

Diss. ETH No. 23560

RATIONAL ELECTRODE MATERIALS SYNTHESIS & DESIGN TOWARDS BETTER LI/NA-ION BATTERIES

GUOBO ZENG

ETH zürich

GRAPHENE

Originally design: Simon Page

RATIONAL ELECTRODE MATERIALS SYNTHESIS & DESIGN
TOWARDS BETTER LI/NA-ION BATTERIES

POWERED BY | **GUOBO ZENG** |

Diss. ETH No. 23560
ZURICH 2016

DISS. ETH NO. 23560

**RATIONAL ELECTRODE MATERIALS SYNTHESIS & DESIGN
TOWARDS BETTER LI-/NA- ION BATTERIES**

A dissertation submitted to attain the degree of
DOCTOR OF SCIENCES of ETH ZURICH
(Dr. sc. ETH Zurich)

Presented by

GUOBO ZENG

M.Sc. Materials Science, ETH Zurich
Born on Dec. 3rd, 1985, Guilin, P. R. China

Accepted on the recommendation of
Prof. Dr. Markus Niederberger, examiner
Prof. Dr. Reinhard Nesper, co-examiner
Prof. Dr. Petr Novák, co-examiner

May 2016 Zurich

Too simple, sometimes naive.

Jiang Zeming

President of P. R. China (1993 - 2003)

Acknowledgements

Time flies.

I never thought that I would be staying in Switzerland for more than seven years. Life here is beautiful and peaceful, it very often let me forget time elapsing. I enjoy the four seasons without realizing time slips under ski board on the top of Alps, passes by blooming flowers in Aprils, hikes through meadows in the valleys or steps on fallen leaves in Höggerberg woods. Life wouldn't be better elsewhere.

Throughout my PhD study in the group of multifunctional materials, I have had the pleasure of working with and learning from many wonderful individuals to whom I am deeply indebted to and thankful to have met. Specifically, I would like to thank the following people:

The first person coming into my mind is Prof. Dr. Markus Niederberger who gave me the opportunity to join his research group when I was still an immature Master student. Once I directly went to him when I saw he was having lunch alone at Mensa and told him what I was doing for my Master thesis. "Good", he said. This was like yesterday happening. During the whole PhD study, I enjoyed the maximum freedom that a PhD student could have. He is the person who influenced me a lot. From him I truly learned how research should be conducted. He is a professor I fully admire.

Special thanks go to Prof. Dr. Reinhard Nesper at ETH Zurich and Prof. Dr. Petr Novák at PSI who immediately agreed to be the co-examiners for my PhD defense. Prof. Nesper was also my Master thesis supervisor. That was my starting point into the battery research. I appreciate two decades of experience on batteries from Prof. Novák from whom I received a lot of help when I established our own electrochemistry lab. Huge thanks also go to Prof. Dr. Manfred Fiebig, chair of D-MATL, who share his precious time to be the chair of my defense committee.

My sincere thanks go to Mrs. Gisela Angst-Schär for her administrative help and the kindness to me, and to everyone in the group.

From time to time, I think of Dr. Idalia Bilecka who often helped me when I started my PhD study in the group. When I heard from Markus that she is now a mother, I was very glad of the news. The time with Dr. Li Luo was particularly good since she is a typical Chinese lady with all traditional virtues. Felix Rechberger and Michael Imhof are specially thanked for the first skiing

lesson I learned from them. That was a lot of fun. Working with Dr. Alessandro Lauria is enjoyable. We had dozens of interesting conversations over diverse topics. Mario Bärtsch is always willing to help and he contributed an excellent German translation for my dissertation abstract.

I would like to express thanks to all other lab colleagues for sharing great time together, enabling to work in a positive and comfortable environment. I would like to show my gratitude to Dr. Wei Cheng, Ofer Hirsch, Dr. Niklaus, Kränzlin, Dr. Inga Olliges-Stadler, Dr. Bettina Ludi, Dr. Florian Heiligtag and all the others, for their helpful and interesting discussions both inside and outside of academia.


I would like to thank our collaborators for their expertise in all aspects: Dr. Dorota Koziej, Dr. Riccarda Caputo, Dr. Nan Shi, Dr. Michael Hess, Dr. Daniel Carriazo, Dr. Elena Tervoort-Gorokhova, Dr. Alla Sologubenko and Lu Jin.

Students at ETH Zurich are among the best around the world. I would like to thank the students who worked together with me either for a Master thesis or projects. They are Gian Cadisch, Xi Chen, Cynthia Gruber, Martin Sarott, Xiaoyu Chen and Etienne Trachsel.

I highly appreciate the Swiss National Science Foundation not only for its abundant financial support, but also the flexibility it allows for a project.

If there were someone who made my routine PhD study more colorful, my girlfriend, Yuhui, is one of them. She is special and talented. Life will be totally different if without her, but certainly less wonderful as it is now. There will be long undiscovered adventure ahead awaiting us, and I am looking forward to it. The final words are always left to my family members. They always stand behind, watch and support me no matter what happens and no matter where I am.

Thank you.



On the train from Zurich to Paris

May 1st 2016

Table of Contents

ACKNOWLEDGEMENTS	I
ABSTRACT	VI
ZUSAMMENFASSUNG	VIII
CHAPTER 1 INTRODUCTION	1
1.1 GENERAL MOTIVATION	1
1.2 LI-ION BATTERIES AND LITERATURE REVIEW	2
1.2.1 <i>Electrochemical cell</i>	3
1.2.2 <i>Battery</i>	4
1.2.3 <i>Historical developments in Li-battery research</i>	6
1.2.4 <i>Working principle of Li-ion batteries</i>	7
1.2.5 <i>Advantages of the Li-ion batteries</i>	7
1.2.6 <i>Design a Li-ion battery</i>	8
1.2.7 <i>Electrolyte</i>	11
1.3 CATHODE/POSITIVE ELECTRODE	14
1.3.1 <i>Layered Dichalcogenides</i>	15
1.3.2 <i>Layered Oxides</i>	16
1.3.3 <i>Layered LiMO₂ Oxides</i>	17
1.3.4 <i>Spinel LiM₂O₄</i>	19
1.3.5 <i>Olivines LiMPO₄</i>	20
1.3.6 <i>Others</i>	22
1.4 ANODE/NEGATIVE ELECTRODE	25
1.4.1 <i>Carbon-based materials</i>	25
1.4.2 <i>Non carbon-based materials</i>	27
1.5 NANOENGINEERING	30
1.6 BEYOND LI	32
CHAPTER 2 TAILORING POLYMORPHS OF LIFEPO₄ AS CATHODES	34
2.1 INTRODUCTION	34
2.2 RESULTS AND DISCUSSION	35
2.3 CONCLUSION	49
2.4 EXPERIMENTAL SECTION	50
CHAPTER 3 SPINEL-TYPE METAL OXIDES AS ANODES	53
3.1 INTRODUCTION	53
3.2 RESULTS AND DISCUSSION	55

3.3 CONCLUSION.....	65
3.4 EXPERIMENTAL SECTION	65
CHAPTER 4 HIERARCHICAL GRAPHENE-BASED AEROGELS AS ANODES	68
4.1 INTRODUCTION.....	68
4.2 RESULTS AND DISCUSSION.....	68
4.3 CONCLUSION.....	80
4.4 EXPERIMENTAL SECTION	81
CHAPTER 5 CONCLUSION	84
5.1 TAILORING THE POLYMORPHS & MORPHOLOGIES OF LiFePO_4 AS CATHODES;.....	84
5.2 SPINEL-TYPE METAL OXIDE/RGO COMPOSITE AEROGELS AS ANODES	85
5.3 HIERARCHICAL GRAPHENE-BASED AEROGELS AS ANODES	85
5.4 ADDITIONAL REMARKS	86
CHAPTER 6 OTHER PROJECTS.....	88
6.1 Ni:MO ₂ , XANES & EXAFS STUDY.....	88
6.2 Cu ₃ N	89
6.3 VANADIUM OXIDES.....	90
6.4 TiO ₂	91
6.5 LiFePO ₄ STICKS FORMATION MECHANISM.....	92
6.6 LiFePO ₄ WITH VARIED MORPHOLOGIES AND PHASES.....	93
6.7 LiFeSO ₄ F & NaFeSO ₄ F	94
6.8 MO _x S _y /C/RGO FOR NIBS	95
6.9 ALLOYING-TYPE MATERIALS FOR LIBS & NIBS	96
LIST OF THE SYMBOLS AND ABBREVIATIONS.....	97
APPENDIX.....	99
A. CELL PREPARATION.....	99
<i>A.1 The cell instrument</i>	<i>99</i>
<i>A.2 Electrode preparation</i>	<i>99</i>
B. CHARACTERIZATION OF ELECTROCHEMICAL CELLS	100
<i>B.1 Cell voltage.....</i>	<i>101</i>
<i>B.2 Current density.....</i>	<i>101</i>
<i>B.3 Charge capacity</i>	<i>101</i>
<i>B.4 Theoretical specific charge and theoretical charge density.....</i>	<i>101</i>
<i>B.5 Practical specific charge and practical charge density</i>	<i>101</i>
<i>B.6 Theoretical specific energy and theoretical energy density.....</i>	<i>102</i>
<i>B.7 Practical specific energy and practical energy density</i>	<i>102</i>

<i>B.8 Specific power and power density</i>	102
C. SUPPORTING INFORMATION FOR CHAPTER 2	103
D. SUPPORTING INFORMATION FOR CHAPTER 3	109
REFERENCES	118
CURRICULUM VITAE	119

Abstract

Lithium ion batteries (LIBs) revolutionized the market for mobile devices after SONY® successfully commercialized the first $\text{Li}_{1-x}\text{CoO}_2/\text{C}$ cell in 1991. Today, with an ever-increasing demand for portable electronic devices and the next generation electric and hybrid-electric vehicles (EVs/HEVs), the batteries are hitting a bottleneck. Energy/power density, lifespan, safety and cost are critical issues that continue to plague the development of LIBs for the potential market of EVs. Among all components in a LIB, the electrode materials hold the key factors towards better performance for the batteries.

The development of “electrode materials on nanoscale” has been attracting great attention, in virtue of their exceptional characteristics that distinguish them from those of bulk crystals. In addition to down-sizing strategy, “design of nanostructured electrode architectures” is another key towards superior battery performance.

In the scope of my PhD study, I mainly focus on the synthesis of electrode materials and the design of electrode architectures on nanoscale level, aiming at better batteries. Followed by a very general introduction to the state of art of LIBs, I am going to report three individual stories including the cathode and anode materials.

Olivine- LiFePO_4 , one of the most successful cathode candidates for LIBs, was discovered by Goodenough *et al.* in 1997. When high pressure (65 kbar) and elevated temperature (900 °C) is applied, olivine- LiFePO_4 (α -phase) transforms into the high-pressure phase (β -phase). In Chapter 2, we report a facile approach to directly tailor the two polymorphs of LiFePO_4 in a controlled way under mild conditions. Employing a microwave-assisted non-aqueous route, highly crystalline LiFePO_4 with either α - or β -phase can be efficiently synthesized, and their electrochemical behavior was systematically studied.

In Chapter 3, we will switch to the anode materials. Spinel-type metal oxides (AB_2O_4) are able to deliver high capacities *via* conversion reaction mechanism. However, they

suffer from poor Li^+ and e^- conductivities and the drastic volume changes upon Li-ion uptake severely impede the high-rate and cyclability performance towards their practical application. We present a general and facile approach to fabricate flexible spinel-type oxide/reduced graphene oxide (rGO) composite aerogels as binder-free anodes. Benefitting from the hierarchical porosity, conductive network and mechanical stability constructed by inter-penetrated rGO layers, and from the pillar effect of NPs in between rGO sheets, the hybrid system synergistically enhances the intrinsic properties of each component. Consequently, the spinel/rGO composite aerogels demonstrated much enhanced rate capability and long-term stability without obvious capacity fading for 1000 cycles at high current rates.

Inspired by the concept above, we further generalized the strategy of the composite aerogels used in LIBs. In Chapter 4, we will focus more on the fabrication of hierarchical graphene-composite aerogels. Since 2004 graphene and its derivatives have attracted immense attention owing to its highly appealing properties. When it is used in batteries as anode, despite of huge research efforts, the capacity, rate performance and long-term stability of graphene-based batteries is still far from being satisfactory. We fabricate a graphene-based composite aerogel in which three categories of spacers on different length scales between the graphene sheets build up a complex hierarchical structure. As a result of the multi-scale spacers strategy, the composite aerogel anodes offered ultra-long stability over 10'000 cycles, still with high energy/power density.

At the end, I will give a very brief description about what we are still working on, *e.g.* rational tailoring the polymorphs of LiFePO_4 or sodium-ion batteries.

Through this dissertation, I hope we have pushed the front line of energy storage and conversion research a little forward.

Zusammenfassung

Lithium Ionen Batterien (LIBs) revolutionierten den Markt für mobile Geräte, nachdem SONY® die erste $\text{Li}_{1-x}\text{CoO}_2/\text{C}$ Batterie/Zelle im Jahre 1991 kommerzialisierte. Durch die stetig steigenden Anforderungen in tragbaren elektronischen Geräten als auch durch die Anwendungen in Elektroautos gerät die Leistungsfähigkeit gegenwärtiger Batterien an ihre Grenzen. Energie/Leistungsdichte, Lebenszeit, Sicherheit und Kosten sind kritische Grössen, welche die potentielle Vermarktung von Elektro- und/oder Hybridautos (EA/HA) basierend auf LIBs begrenzen. Verglichen mit anderen Komponenten in einer LIB stellen Elektrodenmaterialien die Schlüsselfaktoren dar bezüglich deren Leistungsfähigkeit.

Die Entwicklung von Elektrodenmaterialien im Nanobereich hat grosse Aufmerksamkeit auf sich gezogen aufgrund ihrer aussergewöhnlichen Eigenschaften, welche sich markant von Elektrodenmaterialien im Makrobereich unterscheiden. Zusätzlich zur „Nano-Miniaturisierung“ ist das Design einer nanostrukturierten Elektrodenarchitektur ein weiteres wichtiges Element, um die Batterieleistung zu verbessern.

Im Zentrum meiner Doktorarbeit stehen die Synthese von Elektrodenmaterialien und das Design von Elektrodenarchitekturen im Nanobereich mit dem Ziel, leistungsfähigere Batterien zu erhalten. Gefolgt von einer allgemeinen Einführung bezüglich des aktuellen Standes der Batterieforschung der LIB(s) werde ich drei verschiedene Methoden betreffend Kathoden- und Anodenmaterialien darlegen.

Olivin- LiFePO_4 , einer der besten Kathodenmaterialien in Bezug auf LIBs wurde im Jahr 1997 von Goodenough *et al.* entdeckt. Unter hohem Druck (65 kbar) und hohen Temperaturen (900°C) wandelt sich Olivin- LiFePO_4 (α -Phase) in die Hochtemperaturphase (β -phase) um. Im 2. Kapitel dokumentieren wir ein einfaches Vorgehen, um die beiden Polymorphe des LiFePO_4 unter milden Bedingungen kontrolliert zu erhalten. Eine mikrowellengestützte, nichtwässrige Syntheseroute wurde gewählt, um die α - oder β -Phase zu synthetisieren. Des Weiteren wurden deren elektrochemische Eigenschaften systematisch untersucht.

Im Kapitel drei wechseln wir zu den Anodenmaterialien. Metall Oxide des Spinel-Typs (AB_2O_4) verfügen über hohe Kapazitäten *via* Umwandlungsreaktionsmechanismus. Dem gegenüber steht die schlechte Li^+ - und e^- - Leitfähigkeit und die drastische Volumenänderung bei Li -Ionen Aufnahme. Dies hat negative Auswirkungen auf die Zyklierfähigkeit als auch auf die Schnelladefähigkeit, womit die Anwendbarkeit in der Praxis eingeschränkt ist. In diesem Kapitel legen wir eine allgemeine und einfache Methode dar, flexible Membranen des Spinel-Typs/reduziertes Graphenoxid (rGO) als binderfreie Aerogele herzustellen. Die hierarchische Porosität des leitfähigen Netzwerks ermöglicht eine hohe mechanische Stabilität durch die Verkeilung von rGO Schichten mit den Nanopartikeln. Die dadurch entstehenden Synergismen verbessern die intrinsischen Eigenschaften der einzelnen Komponenten. Deshalb weist das Spinel/rGO Komposit Aerogel eine viel höhere Schnellladerate als auch eine höhere Langzeitstabilität auf, ohne nennenswerte Kapazitätsverluste während 1000 Ladungszyklen bei hohen Ladungsdichten zu verzeichnen.

Inspiziert durch das oben erwähnte Konzept haben wir uns die selbige Strategie zunutze gemacht. Im Kapitel vier wird die Herstellung von hierarchischen Graphenoxid Kompositaerogelen genauer erläutert. Seit dem Jahr 2004 haben Graphen und dessen Abkömmlinge grosse Aufmerksamkeit auf sich gezogen aufgrund deren vorteilhaften Eigenschaften. Trotz grosser Forschungsarbeit auf diesem Gebiet sind Kapazität, Ratenleistung und Langzeitstabilität von Graphen basierten Kompositaerogel-Batterien verbesserungswürdig. Wir dokumentieren Graphen basierte Kompositaerogele mit drei verschiedenen Kategorien von Abstandshaltern in verschiedenen Längenbereichen zwischen Graphenschichten, welche eine Komplexe hierarchische Struktur bilden. Diese „multiskalen-Zwischenstück“ Strategie erlaubt es, Kompositaerogel-Anoden mit einer grossen Langzeitstabilität von über 10'000 Zyklen zu erhalten, und die ausserdem eine hohe Energie/Leistungsdichte aufweisen.

Am Schluss werde ich kurz beschreiben, an welchem Forschungsthema ich aktuell arbeite, wie z.B. die Rationalisierung der polymorphen Formen von $LiFePO_4$ oder Natriumionen Batterien.

Durch diese Dissertation hoffe ich, die Grenzen der Energiespeicherung und Umwandlung etwas vorangetrieben zu haben.

Chapter 1 Introduction

1.1 General motivation

Environmental issues have become a global concern.¹ Gaseous emissions from consumption of fossil fuels are often criticized, owing to its consequence of causing global warming. Furthermore, oil and natural gas reserves will face depletion in the next decades.² All concerns about energy safety and cleanliness trigger great attention and interest to switch to alternative energy sources. Nuclear, hydroelectric, solar, wind, wave and geothermal energies are harvested or produced to meet the tremendous demand of electricity in our daily life and in industry. Nuclear energy, though as a constant power source, produces huge amount of radioactive waste. There are some concerns regarding environmental impact from hydropower as well. Other renewable energy often highly depends on time (*e.g.* solar energy), or is restricted in location (*e.g.* wind energy). In addition, the demand for electricity varies during the time (**Figure 1.1a**). To better utilize energy or electricity, energy storage is required.

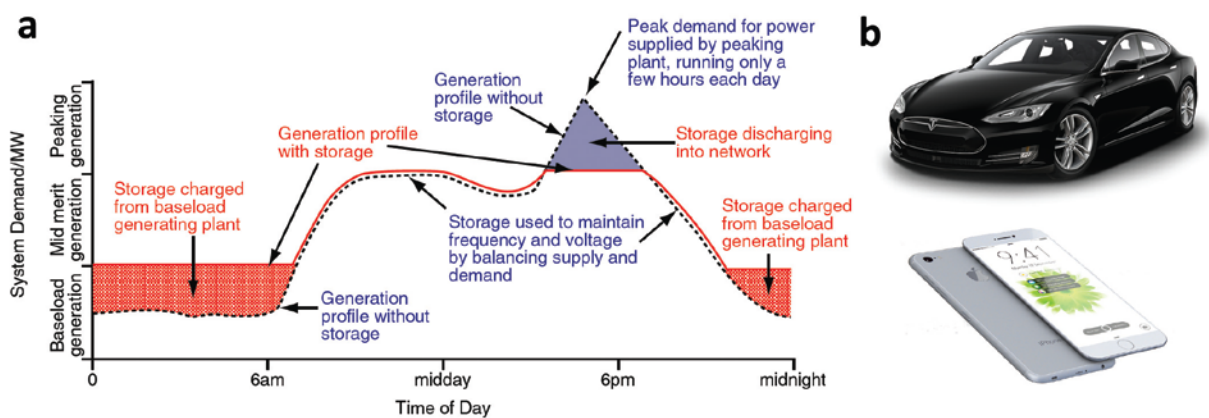


Figure 1.1 a, Typical electrical power profile, showing the large variations during a 24-h period. In a load-leveling scenario, an electrical energy storage device would be charged during periods of low power demand and would discharge during periods of high power demand, thus filling in the valleys and cutting off the peaks. Graph courtesy from Ref [3] **b, An electric car and a mobile phone powered by Li-ion batteries.**

Besides large scale of energy storage is needed for power plants, energy storage at smaller scale is more familiar to us. From mobile electronic devices, such as mobile phones or laptop computers, to next generation of electric and hybrid-electric vehicles (EVs/HEVs), all require to be powered (**Figure 1.1b**).

How shall we deal with such energy storage and conversion at all different scales? One answer comes from the chemical side. The most convenient and clean form of energy storage is portable chemical energy. The batteries offer such portability of chemical energy storage. They are efficient storage devices with the ability to reversibly transform chemical energy to electrical energy with high conversion efficiency, typically exceeding 90% of input energy, and no gaseous exhaust. ⁴

Benefitting from these advantages, batteries are currently well developed as power source for an increasingly diverse range of applications, from the mobile devices to the next generation EVs/HEVs. Batteries have evolved over the decades from lead-acid, nickel-cadmium, nickel-metal hydride (Ni-MH) to current lithium-ion batteries (LIBs), and beyond. Despite of remarkable growth of battery sales in the market, the science and engineering underlying battery technology is often criticized for its slow advancement.⁵ Cost, safety, stored energy density, charge/discharge rates, and service life are the issues that impede the development of LIBs for the potential market of EVs/HEVs. Recently, development of nanostructured materials has been attracting great attention, in virtue of their exceptional characteristics which distinguish them from those of bulk crystals.^{6,7} Nanostructured compounds with reduced dimensionality are usually expected to possess great properties in energy storage and conversion.

In this study, we mainly focused on the synthesis of electrode materials with varied morphologies, and the rational design of nanostructured electrodes, with the hope to pursue higher capacity, larger power, longer cyclability and lower cost for the batteries.

1.2 Li-ion batteries and literature review

To better understand the science and technology behind LIBs, several fundamental definitions and concepts of electrochemistry are introduced in advance, followed by a brief historical story of the development of batteries. The state of art of LIBs and

challenges/issues facing the rechargeable LIBs are reviewed. At last, the nanotechnologies applied to the field are also introduced.

1.2.1 Electrochemical cell

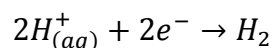
An electrochemical cell consists of two electrodes (the anode and the cathode) immersed into the electrolyte solution. The anode is defined as the electrode where oxidation reaction occurs and the cathode is the electrode where the reduction takes place. The electrodes are electronic conductive and the electrolyte solution is an ionic conductor. At the interface between electrodes and electrolyte, the redox reactions occur spontaneously, giving rise to an electrical current. As a result, the chemical energy is directly converted into electrical energy.

The discharge of an electrochemical cell always corresponds to a chemical process that can be divided into two spatially separated electrochemical half-reactions or electrode reactions. These electrochemical half-reactions can then be combined to form an electronically neutral overall cell reaction.

One of the most important parameters to characterize an electrochemical cell is cell potential. Experimentally, if the external resistance between the electrodes is made very high, so that very little current flows, the observed potential difference of the electrochemical cell becomes the rest potential, E_r , which, under equilibrium conditions, is equal to the electro-motive force or EMF of the cell, E^0 .

Theoretically, if the individual electrode potential is known, it is convenient to predict the EMF of the cell. However, the electrode potential of half-reaction can never be measured independently. A reference electrode is required. Most common reference electrode is the standard hydrogen electrode (SHE).

The standard hydrogen electrode undergoes the reaction



which is, by convention, shown as reduction but, in fact, the SHE can act as either the anode or the cathode, depending on the relative oxidation/reduction potential of the other electrode/electrolyte combination. The term "standard" in SHE indicates that the measurement is under conditions $T = 25\text{ }^\circ\text{C}$, $p = 1\text{ atm}$ and all species at unity activity.

With the reference to SHE, we can tabulate the standard electrode potential, E^0 , which also can be calculated under equilibrium conditions:

$$E^0 = \frac{-\Delta G^0}{nF} \quad [\text{V}]$$

ΔG^0 : Standard Gibbs free energy

F : Faraday constant

n : number of electrons exchanged

This equation links the standard electrode potential (or EMF) to the Gibbs free energy change of the overall current-producing reaction. It is one of the most important equations in the thermodynamics of electrochemical systems. It follows directly from the first law of thermodynamics, since nFE^0 is the maximum value of useful (electrical) work of the system in which the reactions are considered to take place. According to the basic laws of thermodynamics, this work is equal to $-\Delta G^0$.

So far, tabulation of the standard electrode potential, E^0 , is established. Hence, the cell potential can be easily calculated from the equation (note: the standard electrode potential is tabulated as reduction potential by convention):

$$\Delta E^0 = E_{cathode/positive\ electrode}^0 - E_{anode/negative\ electrode}^0 \quad [\text{V}]$$

For real (non-standard) systems, the Nernst equation is used to calculate the electrode potential of the half-reactions at equilibrium:

$$E = E^0 - \frac{RT}{nF} \sum \ln a_i^{v_i} \quad [\text{V}]$$

R : gas constant

v_i : stoichiometric coefficient

T : absolute temperature

a_i : activity

1.2.2 Battery

The battery is a number of cells combined either in parallel to allow larger electric current, or in series to increase supply voltage. (Note: in our text below, we do not strictly distinguish between the battery and the cell.) There are mainly two broad categories of batteries, primary batteries and secondary batteries, respectively.

i. Primary batteries (non-rechargeable batteries)

As its name suggests, primary batteries are intended to be used only once and discarded. They are usually used in portable electronic devices in which only small current for a long time is needed. The batteries are disposable because the chemical reactions are usually irreversible so that the active electrode materials cannot be restored to its initial state after being used. Most common types of non-rechargeable batteries include zinc-carbon batteries, zinc-manganese dioxide alkaline batteries and zinc-silver oxide batteries.

ii. Secondary batteries (rechargeable batteries)

On the contrary to primary batteries, the electrochemical reactions in secondary batteries are reversible. The active materials are exhausted during the discharging process and can be recovered in the charging process. Currently, the most popular examples are LIBs. Rechargeable batteries initially cost more than primary/disposable batteries, but have a much lower total cost of ownership and environmental impact, as they can be recharged inexpensively many times before they need replacing. Various types of batteries are summarized in in **Table 1.1** in which the capacity, theoretical and practical energy values are given.⁸

Table 1.1 The voltage, theoretical specific energy values (considering only the mass of the active materials in the electrodes), values achieved in practice and energy densities for the major battery systems. Table is reproduced from ref [8].

Battery chemistry	Type	Voltage [V]	Theoretical specific energy [Wh kg ⁻¹]	Practical specific energy [Wh kg ⁻¹]	Practical energy density [Wh cm ⁻³]
Zn/MnO ₂ (alkaline)	Primary	1.5	358	145	400
Li/I ₂	Primary	2.8	560	245	900
Pb/acid	Secondary	2.1	252	35	70
Ni/Cd	Secondary	1.3	244	35	100
Ni/MH	Secondary	1.3	240	75	240
Na/S	Secondary	2.1	792	170	345
Na/NiCl ₂ (ZEBRA)	Secondary	2.6	787	115	190
Li-ion batteries*	Secondary	4.1	410	150	400

* There is a large range of values for LIBs owing to the great variety of available electrode materials, both for the positive and negative electrodes, LiCoO₂/C as an example here.

1.2.3 Historical developments in Li-battery research

In order to pursue higher energy density of power devices, researchers started to consider Li metal as the anode of the batteries in the 1970s based on its several unique characteristics:

- Li has one of the most negative SHE value, $E^0 = -3.04$ V
- The lightest metal, $M = 6.94$ g mol⁻¹, and specific density $\rho = 0.53$ g cm⁻³
- Extremely high specific charge, $Q_{th} = 3862$ mAh g⁻¹

The idea of using Li metal as the anode and TiS₂ as cathode was commercialized by Exxon in 1972.^{9, 10} However, it soon encountered safety issues. On repeated charge/discharge cycles, Li metal grows in dendritic form that can penetrate across the separator to cause short-circuit of the battery, which leads to explosion or fire hazards (See **Figure 1.2a**).

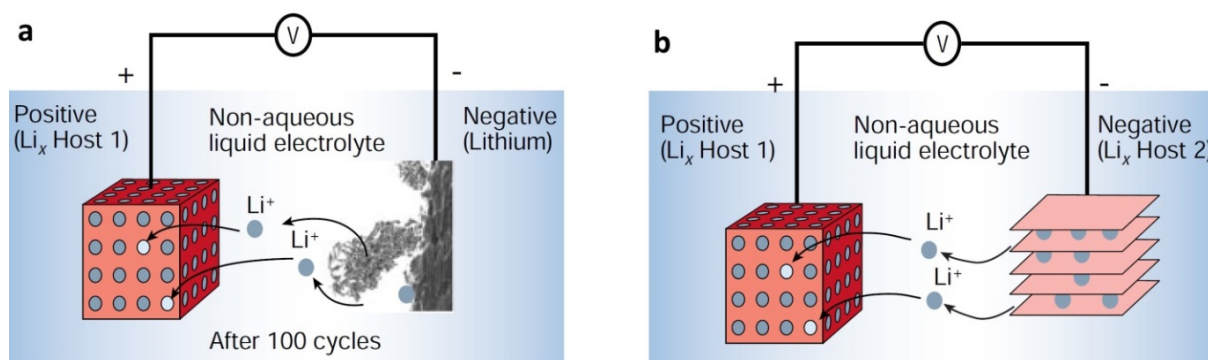


Figure 1.2 Illustration of the operating principles of Li batteries. **a**, Rechargeable Li-metal battery, and the dendrite growth at the Li surface; and **b**, Rechargeable Li-ion battery. Reproduced from Ref [5].

To avoid the safety issues using Li metal, several alternative methods were investigated in which either the electrolyte or the anode was modified. The first method involved replacing metallic Li by an insertion material or compound (**Figure 1.2b**). The idea was first realized by Murphy *et al.*¹¹ and then by Scrosati *et al.*¹² and led, at the end of the 1980s and early 1990s, to the so-called Li-ion or rocking-chair technology. Because of the presence of Li in its ionic form rather than metallic state, Li-ion cells do not suffer from dendrite problem and are, in principle, inherently safer than Li-metal cells (see **Figure 1.2b**). Later, Goodenough proposed the families of Li_xMO₂ (M = Co, Ni or Mn)

compounds that are still dominating in today's batteries.¹³ In 1991 Sony Corporation released the first commercial lithium-ion battery using LiCoO_2/C redox chemistry.¹⁴

1.2.4 Working principle of Li-ion batteries

As illustrated in **Figure 1.2b**, the Li-ion cell is typically composed of two insertion compounds. The Li ions shuttle back and forth between the positive and negative electrode. The electrochemical process is the uptake of Li ions at the negative electrode during charge and their release during discharge. Thus, the net current-forming reaction is actually a continuous pumping of Li ions between two host materials. Advantage of this system is, that contrary to the lead acid, no electrolyte is consumed, so that a very little amount of electrolyte is needed. In this way, a more compact cell construction is possible.

The procedure for fabricating a Li-ion cell consists of using a Li-rich compound as the positive electrode. The cell is thus assembled by coupling this Li-source electrode with a Li-sink as negative electrode. The cell is activated by charging, by which the Li ions are stored in the sink. Positive electrodes which do not contain Li after their synthesis have to be chemically lithiated before using.

1.2.5 Advantages of the Li-ion batteries

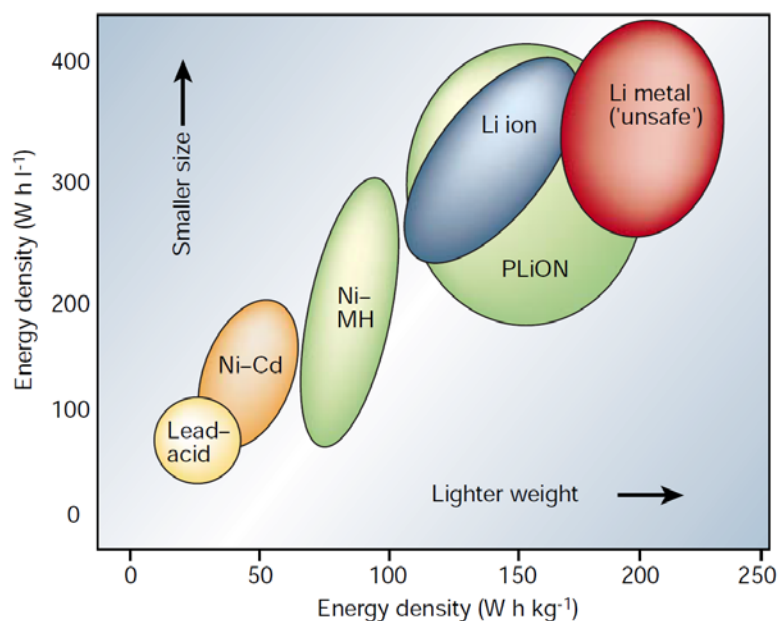


Figure 1.3 Comparison of the different battery technologies in terms of energy density in volume and weight. Graph is taken from Ref [5].

The main problem of conventional batteries as power source either for mobile electronic or EVs/HEVs is their comparatively low specific energy, which impedes their further applications. The low specific energy is usually owing to their low voltage. The energy density of Li-ion batteries (nominal voltage > 3.3 V) with higher operating voltage is two-three times higher than common Ni-MH (nominal voltage < 3.5 V) or the lead-acid power source, which make it much more competitive (**Figure 1.3**).

Compared to other redox-chemistry systems, Li-ion batteries offer several advantages, such as higher voltages, larger (specific) energy density, better (specific) power density and longer service life. The “specific” term is attributed to that Li is lighter in weight and smaller in size than other systems. Furthermore, the use of non-aqueous electrolytes in lithium batteries permits the operation over a wide range of temperatures.

1.2.6 Design a Li-ion battery

There are plenty of excellent references [4][8][15][16][17], particularly the one from Goodenough⁴, elaborating the principles how to design an ideal Li-ion cell: choice of cathode, anode and electrolyte candidates both in theory and in practice.

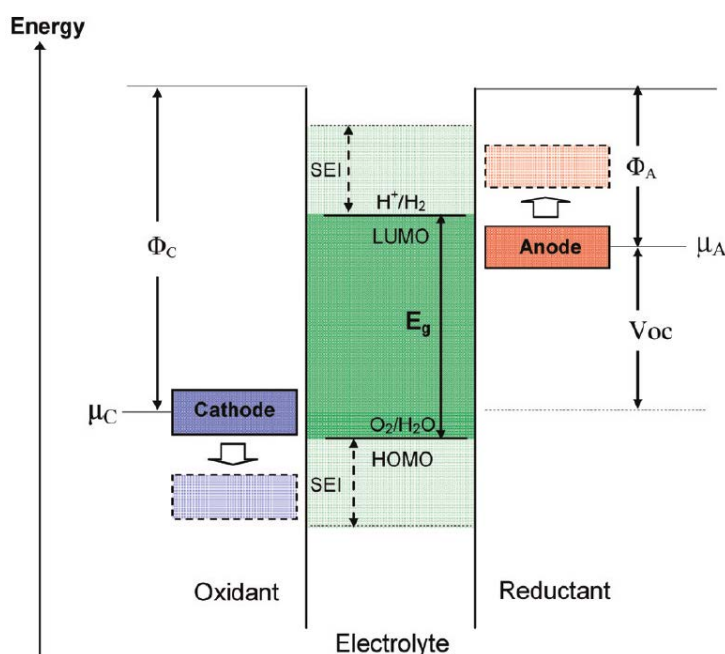


Figure 1.4 Schematic open-circuit energy diagram of an aqueous electrolyte. Φ_A and Φ_C are the anode and cathode work functions, respectively. E_g is the energy difference between the LUMO and HOMO of the electrolyte which is the window providing thermodynamic stability of the cell. However, in a situation when $\mu_A > \text{LUMO}$ and/or a $\mu_C < \text{HOMO}$, a SEI layer that can offer a kinetic stability is necessary. Graph is taken from Ref [4].

For a thermodynamic stable cell/battery, the relative electron energies in the electrodes and an aqueous electrolyte are shown in **Figure 1.4**.

The anode is the reductant with electrochemical potential μ_A , while the cathode is the oxidant with electrochemical potential μ_C . The potential difference between two electrodes gives the open circuit voltage, V_{oc} . The energy separation E_g of the lowest unoccupied molecular orbital (LUMO) and the highest occupied molecular orbital (HOMO) of the electrolyte is the “window” of the electrolyte. The requirement of thermodynamic stability demands the location of the electrode μ_A and μ_C within the window of the electrolyte, respectively.

An anode with μ_A above the LUMO will reduce the electrolyte; however, if a passivating solid electrolyte interphase (SEI) layer is created between the electrode and electrolyte, so a barrier can prevent electron transfer from the anode to the electrolyte LUMO. Similarly, a cathode with a μ_C below the HOMO will oxidize the electrolyte, so a passivation layer between the electrode and electrolyte is required to protect electron transfer from the electrolyte HOMO to the cathode. Thermodynamic stability constrains the open circuit voltage V_{oc} of a cell to

$$V_{oc} = \mu_A - \mu_C < E_g$$

But a stable SEI layer can provide kinetic stability to a larger V_{oc} if $V_{oc} - E_g$ is not too large.⁴

The electronic current in the external circuit should be, in principle, equivalent to the internal ionic current within the battery. However, the ionic current density of the electrolyte and electrode, including the rate of ion transfer across the SEI, is usually much smaller than the electronic current density in the electrode and external metal circuit. Especially, at higher current rate, the ionic motion within an electrode and across a SEI is too slow for the charge distribution to reach equilibrium with the electric motion, which is why the reversible capacity decreases with increasing current density in the battery and why this capacity loss is recovered on reducing the rate of charge/discharge.⁴

Aqueous electrolytes involve the movement of H^+ , and high H^+ conductivity demands an aqueous electrolyte in practical ambient environment. But only $E_g \approx 1.3$ eV is allowed,

which limits V_{oc} and therefore the energy density. To promote a higher V_{oc} and thus a higher energy density ΔV_{oc} , switching to a nonaqueous electrolyte with a larger E_g is required, *i.e.* nonaqueous liquids or polymers, in which Li salts are soluble. However, in this case, the HOMO of the salt and the solvent need to be considered since it may determine the limiting μ_C . Once the window of the Li-ion electrolyte has been determined, one needs to design electrodes of high capacity that have their μ_A and μ_C matched to the LUMO and HOMO of the electrolyte.⁴

As mentioned above, owing to its unique properties, elemental Li^0 would be the ideal anode, however, μ_A of Li^0 locates above the LUMO of practical nonaqueous electrolytes. Therefore, use of Li^0 as an anode is only feasible when a passivating SEI layer is formed. Still, safety issues are present when using Li^0 as an anode. Upon repeated charge/discharge cycles, breaking of the SEI layer in selected areas leads to dendrites growth, which can penetrate through the separator resulting in short-circuit in a battery, leading to dangerous fire consequences.

Therefore, the design principle of a battery lists as follow:

- an anode with a μ_A should match to the LUMO of the electrolyte, and a cathode with a μ_C to the HOMO, or
- a kinetically stable passivating solid electrolyte interphase (SEI) layer which can self-heal quickly if the changes in electrode volume during the charge/discharge cycle break SEI; simultaneously, the SEI layer must allow a rapid Li-ion transfer between the electrode and the electrolyte without blocking electron transfer between the active material and the current collector.

In summary, the main challenges to develop better LIBs for EVs/HEVs in the potentially massive market are to explore low-cost, environmentally friendly materials for the three active components of a battery, 1) a nonaqueous electrolyte of high Li-ion conductivity ($\sigma_{\text{Li}} > 10^{-4} \text{ S/cm}$) over the practical ambient-temperature range $-40 \text{ }^\circ\text{C} < T < 60 \text{ }^\circ\text{C}$ that has a thermodynamically stable window allowing $V_{oc} > 4 \text{ V}$; and 2) an anode and 3) a cathode with their μ_A and μ_C values well matched to the window of the electrolyte as well as each enabling large reversible capacity with fast rate-performance.

1.2.7 Electrolyte

The electrolyte commonly refers to a solution comprising the salts and solvents in the battery terminology. Although the role of electrolyte is often considered not significant, its choice can be crucial. In addition to a large electrolyte window E_g , some additional characteristics of the electrolyte have to be fulfilled:^{4,18}

- A wide electrochemical voltage window, E_g , ideally from 0 to 5 V vs. Li^+/Li^0 ;
- Retention of the SEI during cycling when the electrode particles are changing their volume;
- A Li-ion conductivity $\sigma_{\text{Li}} > 10^{-4}$ S/cm over the temperature range of battery operation so as to minimize the internal resistance. To achieve the purpose, small viscosity generally should be satisfied;
- An electronic conductivity $\sigma_e < 10^{-10}$ S/cm to protect self-discharging;
- A transference number $\sigma_{\text{Li}}/\sigma_{\text{total}} \approx 1$, where σ_{total} includes conductivities by other ions in the electrolyte as well as $\sigma_{\text{Li}} + \sigma_e$;
- A good thermal and chemical stability over ambient temperature ranges and temperatures in the battery under high power (up to 90 °C);
- Chemical stability with respect to the electrodes, including the ability to form rapidly a passivating SEI layer where kinetic stability is required because the electrode potential locates outside the electrolyte window;
- Good compatibility with other components of the cell;
- Safe materials, *i.e.*, preferably nonflammable and nonexplosive if short-circuited (thermal run-off temperature);
- Least environmental impact, low toxicity and low cost.

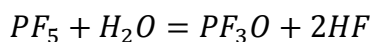
It will be arduous to fulfill all these requirements. In general, the electrolyte is specifically designed for a particular battery application. The electrolytes often used in LIBs are summarized below and in **Table 1.2** (page 14).

i. Organic Liquid Electrolytes

Carbonates are organic liquids that are relatively good solvents for Li salts, because they are aprotic, polar and have a high dielectric constant, which enables them to solvate Li

salts to high concentrations. Besides, they have an oxidation potential (HOMO) at ca. 4.7 V vs. Li⁺/Li and a reduction potential (LUMO) near 1.0 V versus Li⁺/Li. Another advantage of carbonates are, generally, their low viscosity that leads to a low activation energy for Li-ion diffusion. Carbonates extensively used comprise one or two as follows: ethylene carbonate (EC), dimethyl carbonate (DMC), propylene carbonate (PC), diethyl carbonate (DEC), or ethylmethyl carbonate (EMC). When the electrochemical potential of anode is above the LUMO of carbonates, a stable passivating SEI is required to protect the electrolytes from further decomposition. As in the case of carbon (electrochemical potential of carbon > LUMO of carbonates), EC is typically added because it can provide such stable SEI layer on the surface of carbon anode.^{19, 20}

However, the disadvantage of carbonate-based solvents is that they are highly flammable with flash points below 30 °C (see **Table 1.2**). Moreover, the preferred salt, LiPF₆, can undergo an autocatalytic decomposition into LiF and PF₅. The PF₅ reacts irreversibly with any water present



and it reacts with a carbonate electrolyte above 60 °C,²¹ both of which degrade the battery and result in safety hazards.

ii. Ionic Liquids

Ionic liquids have been considered as alternative options for LIBs because they offer several advantages over carbonate-based electrolytes: a high oxidation potential (~5.3 V versus Li⁺/Li), nonflammability, better thermal stability, low toxicity, high boiling points, and a high Li-salt solubility. But the main disadvantages are 1) their higher viscosity which limits the Li-ion conductivity, 2) poor stability at voltages below 1.1 V. Additives are needed to enhance those properties. And 3) the cost should be cut down for massive power batteries.²²

iii. Inorganic Liquid Electrolytes

The inorganic liquid electrolytes are mainly based on LiAlCl₄ and SO₂.²³ Their attraction originates from their high ionic conductivity $\sigma_{Li} = 7 \times 10^{-2}$ S/cm at room temperature.

However, they are hazardous and may produce safety issues. And its electrolyte window is too small to be competitive.⁴

iv. Solid Polymer Electrolytes

Solid polymer electrolytes, where the Li salts are incorporated into a polymer matrix, are a valid alternative to the liquid electrolytes. An solid polymer Li⁺ electrolyte has been used with thin solid electrodes in an all solid-state Li cell. It can also act as the separator between the two electrodes. The advantage is that the polymer is solid but flexible. The flexible polymer can retain contact over an SEI during modest changes of the electrode volume with the state of charge of the battery; however, if the volume change in the electrodes on charge/discharge is too large the solid polymer does not keep good retention of electrode/electrolyte contact. Polyethylene oxides (PEOs) containing a Li salt (LiPF₆ or LiAsF₆) are low-cost, nontoxic, Li-ion polymer electrolytes with good chemical stability.²⁴ The main drawback is the Li-ion conductivity, $\sigma_{Li} < 10^{-5}$ S/cm at room temperature, which is 2-3 orders of magnitude smaller than the organic liquid ones.²⁴ This holds back their applications for power-battery systems.

v. Inorganic Solid Electrolytes

Inorganic solid Li-ion conducting materials having a $\sigma_{Li} > 10^{-4}$ S/cm have been exploited for Li-based electrolytes because they have a wide electrochemical window and fulfill additional requirements.^{25, 26} So far they have only been used in thin-film battery applications in the laboratory, but not in large scale yet.

vi. Other Electrolytes

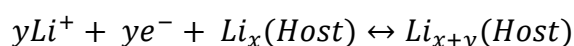
It would be a natural idea to blend different electrolytes and salts in the hope of finding better properties, *i.e.*, hybrids of organic liquid electrolytes, ionic liquids, polymer electrolytes, and/or inorganic solid electrolytes; the most frequently used lithium salts are: LiClO₄, LiPF₆, and LiN(SO₂CF₃)₂. When combining the advantages of each constituent in a hybrid, very often, the disadvantages of each also pop out.

Table 1.2 Nonaqueous electrolytes in LIBs. Table is reproduced from Ref [4].

Electrolytes	Example of classical electrolytes	Ionic conductivity	Electrochemical window (V) vs. Li ⁺ /Li ⁰		Remark
			Reduction	Oxidation	
Liquid organic	1M LiPF ₆ in EC:DEC (1:1)	7	1.3	4.5	Flammable
	1M LiPF ₆ in EC:DMC (1:1)	10	1.3	>5.0	
Ionic liquids	1M LiTFSI in EMI-TFSI	2.0	1.0	5.3	Non-flammable
	1M LiBF ₄ in EMI-BF ₄	8.0	0.9	5.3	
Polymer	LiTFSI-P(EO/MEEGE)	0.1	<0.0	4.7	Flammable
	LiClO ₄ -PEO ₈ + 10 wt % TiO ₂	0.02	<0.0	5.0	
Inorganic solid	Li _{4-x} Ge _{1-x} P _x S ₄ (x = 0.75)	2.2	<0.0	>5.0	Non-flammable
	0.05Li ₄ SiO ₄ + 0.57Li ₂ S + 0.38SiS ₂	1.0	<0.0	>8.0	
Inorganic liquid	LiAlCl ₄ + SO ₂	70	-	4.4	Non-flammable
Liquid organic + Polymer	0.04LiPF ₆ + 0.2EC + 0.62DMC + 0.14PAN	4.2	-	4.4	Flammable
	LiClO ₄ + EC + PC + PVDF	3.0	-	5.0	
Ionic liquid + Polymer	1M LiTFSI + P ₁₃ TFSI + PVDF-HFP	0.18	<0.0	5.8	Less flammable
Ionic liquid+ Polymer + Ionic organic	56 wt % LiTFSI-Py ₂₄ TFSI + 30 wt % PVdF-HFP + 14 wt % EC/PC	0.81	1.5	4.2	Less flammable
Polymer + Inorganic solid	2 vol % LiClO ₄ -TEC-19 + 98 vol% 95 (0.6Li ₂ S + 0.4Li ₂ S) + 5Li ₄ SiO ₄	0.03	<0.0	>4.5	Non-flammable

1.3 Cathode/Positive Electrode

The choice of a cathode/positive electrode involves tailoring of the μ_C of a cathode to the HOMO of the Li-ion electrolyte to be used; the electrode must also be chemically stable in the electrolyte.⁴ To date, practical electrodes have all had host structures into/from which guest Li ions can be inserted/extracted reversibly.^{3, 5} Host structures are preferable because of no or little structural modification occurs during cycling. In such materials the removal and the subsequent insertion of the Li ions in the host lattice proceeds topotactically. The reaction at the positive electrode can be described as follows:



where (HOST) is an insertion cathode.

Several key factors should be met when choosing an insertion compound for the cathode in Li-ion batteries. The requirements are listed as follows:³

- contain a readily reducible/oxidizable ion, for instance a transition metal;
- High free energy of reaction with Li;
- Little or modest structural change upon Li-ion insertion/removal;
- Highly reversible reaction;
- Rapid diffusion of Li-ion in solid;
- Good electronic conductivity;
- Non-solubility in electrolyte;
- Availability or facility of synthesis, and
- Low cost and environmentally benign.

There are extensive studies on different types of cathodes in attempts to fulfill all those criteria above. The individual redox-active compounds preferably offer many of these criteria, but several are opposite in character. All commercialized rechargeable cathode materials to date basically belong to two classes: 1) close-packed structures such as those of layered TiS_2 , LiCoO_2 or cubic LiMn_2O_4 ; and 2) the tunnel structures of LiFePO_4 .³ There are, for sure, a lot of other emerging types of cathodes, *e.g.* polyanion compounds including silicates, fluorosulphate and etc. Due to the scope of this dissertation, it will be only shallowly touched in this Thesis.

1.3.1 Layered Dichalcogenides

In the early beginning of Li battery research, around 1970s, layered dichalcogenides were of particular interest since it was found that the intercalation reactions into the layered materials could be accomplished in an electrochemical cell by inserting ions from the anode.⁵ Of all the layered dichalcogenides, titanium disulfide, TiS_2 , was the most appealing as an energy storage electrode because it was the lightest. Later it was discovered that it was either a small-gap semiconductor or a semi-metal; therefore, no conductive additive was required in the cathode structure.²⁷ It was also found to form a single phase with Li over the entire composition range of Li_xTiS_2 for $0 \leq x \leq 1$. This lack of phase change (solid phase solution) enables all the Li to be removed reversibly without the need for energy loss associated with the nucleation of new phases. In 1976, Whittingham demonstrated that fast Li insertion occurred at room temperature into the

empty octahedral sites of the layered TiS_2 cathode host at *ca.* 2.2 V vs. Li over the solid-solution range $0 < x < 1$.⁹

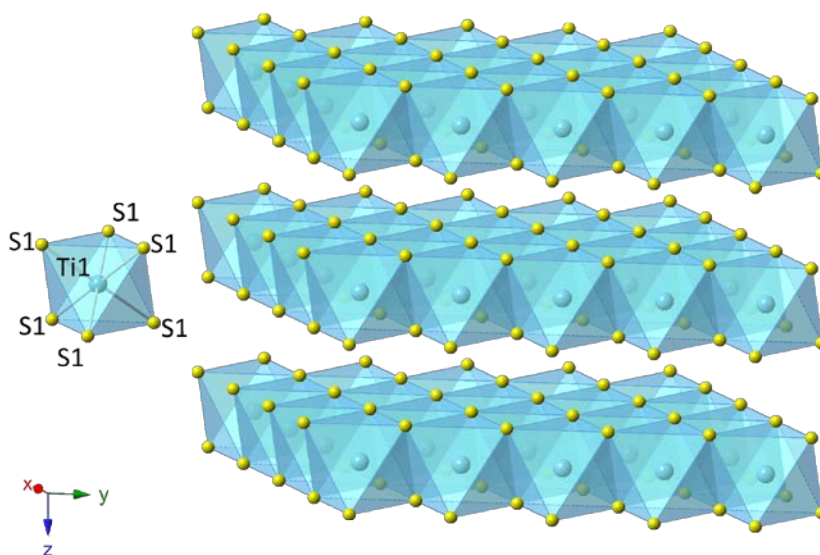


Figure 1.5 Crystal structure of TiS_2 .

TiS_2 adopts a hexagonal close packed structure. Each Ti center is surrounded by an octahedral arrangement of six S atoms that are shared to form extended layers of atoms. The individual layers of TiS_2 are bound together by van der Waals forces (**Figure 1.5**).

Exxon marketed button cells with LiAl anode and TiS_2 cathode for watches and other small devices in 1977-1979. However, it was not a very successful business and thus discontinued later, because of the cost, safety issue from Li dendrite formation and unpleasant odor upon leakage.²⁸ Besides, TiS_2 is a small-gap semiconductor as mentioned above, which means that the voltage of the Li battery could not be increased significantly with a sulfide as the cathode.

1.3.2 Layered Oxides

Layered oxides are one of the most important categories of cathode candidates. Vanadium pentoxide, V_2O_5 , and molybdenum trioxide, MoO_3 , are two of the earliest studied oxides. They both possess layered structure with weak van der Waals interaction between the layers (**Figure 1.6**). The whole structural behavior and phase change upon Li insertion are rather complex; nevertheless, the intercalation mechanism can be much simplified as below:



However, those layered metal oxides never got popular in industry applications owing to their low reaction rate with Li; and if more than one Li is inserted, then drastic permanent structural changes occur resulting in poor cyclability.²⁸ The high-price or toxicity of such elements also impede their further applications.

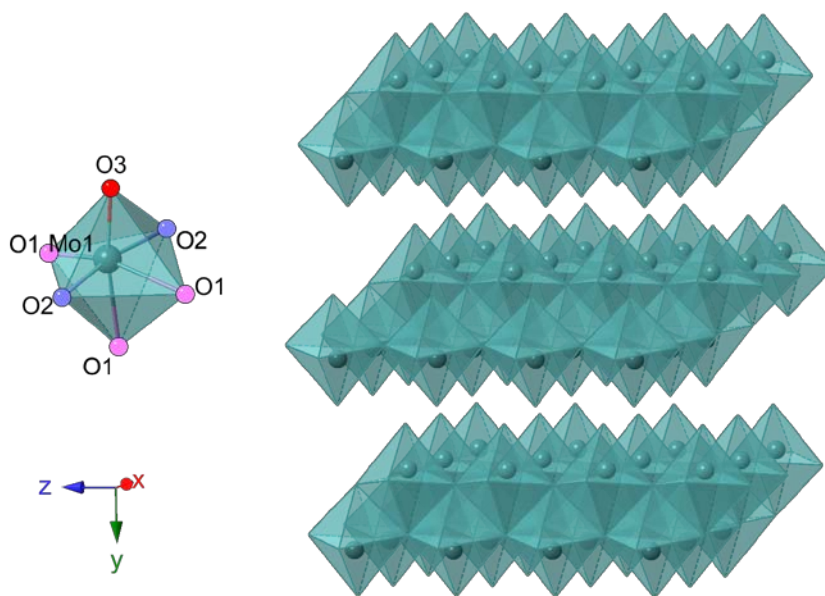


Figure 1.6 Crystal structure of MoO_3 .

1.3.3 Layered LiMO_2 Oxides

On the other hand, Goodenough in 1979 realized LiMO_2 oxides may be well ordered with Li^+ and M^{3+} ions in alternate (1 1 1) octahedral-site planes of a face-centered-cubic array of oxide ions. The Li in LiCoO_2 and LiNiO_2 could be removed electrochemically, and thus making it a feasible cathode material. They demonstrated an open-circuit voltage vs. Li/Li^+ of 4.0V for LiCoO_2 .¹³ More importantly, LiCoO_2 acts as a donor of Li ions, which means that it can be combined with a negative electrode material other than Li metal. By enabling the use of stable and easy-to-handle negative electrode materials (*i.e.* graphite), LiCoO_2 opened a whole new era of possibilities for novel rechargeable battery systems. SONY commercialized the product and achieved the first success in LIBs market in 1991,¹⁴ and since then such configurations have dominated the rechargeable batteries market.

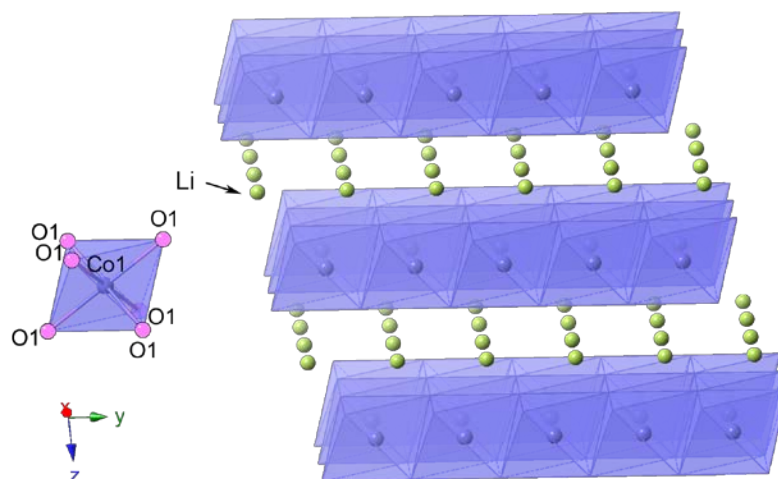


Figure 1.7 Crystal structure of LiCoO_2 .

LiCoO_2 consists of layers of Li that locate between slabs of octahedra formed by Co and O atoms. These octahedrons are edge-sharing, and tilted relative to the layered structure (**Figure 1.7**).

In spite of the commercial success, there were two issues concerning the product: 1). Co is toxic and expensive; 2). Only about half of the Li can be extracted before the oxide starts to lose oxygen or to oxidize the electrolyte to replace the Li^+ by H^+ , which leads to safety hazards for large batteries. Therefore, there was a strong stimulus to remove the Co and to increase the capacity by allowing removal of more Li.²⁷

Much attention has been paid on the layered LiMnO_2 compound for its prospects of providing not only a low-cost but also an environmentally benign cathode material. Goodenough demonstrated that more than half of the Li can be removed from $\text{LiNi}_{0.5}\text{Mn}_{0.5}\text{O}_2$ before the oxide becomes unstable. However, initial trials failed because it is difficult to synthesize the crystal with well-ordered Li ions.²⁷ Later Schougaard *et al.* successfully obtained well-ordered $\text{LiNi}_{0.56}\text{Mn}_{0.44}\text{O}_2$,²⁹ Kang *et al.* synthesized $\text{Li}_1\text{Ni}_{0.5+x}\text{Mn}_{0.5-x}\text{O}_2$,³⁰ and Nesper *et al.* also succeeded to obtain Layered lithium nickel manganese oxides by a oxidative coprecipitation method.^{31, 32} The $\text{Li}_{1-x}\text{Ni}_{0.56}\text{Mn}_{0.44}\text{O}_2$ in Schougaard's work cycled at 0.1 mA cm^{-2} between 2.75 and 4.3V exhibited an initial capacity of about 180 mAh g^{-1} . A stable capacity of 110 mAh g^{-1} was retained at a 5C discharge rate and the full capacity was regained on lowering the charge/discharge rate. These results proved a higher capacity could be achieved in a layered oxide that does not contain Co.

Mixed manganese-cobalt dioxide, $\text{LiMn}_{1-y}\text{Co}_y\text{O}_2$, mixed nickel-manganese dioxide, $\text{LiNi}_{1-y}\text{Mn}_y\text{O}_2$ multielectron redox systems and mixed nickel-manganese-cobalt dioxide, $\text{LiNi}_{1-y-z}\text{Mn}_y\text{Co}_z\text{O}_2$ (NMC) also belong to the category. NMC is one of the most successful cathode material in the current LIBs market. NMC is a competitive contender with LiFePO_4 for the choice of cathode for power tools and HEVs/EVs. The cathode composition is typically one-third Ni, one-third Mn and one-third Co, also known as 1:1:1. Other combinations using different elements (*e.g.* Al) or various ratios of the active cathode materials are possible.²⁸

1.3.4 Spinel LiM_2O_4

Unlike layered oxides, the AB_2O_4 spinel structure forms a three-dimensional structure that improves Li ion diffusion in the electrode, which results in lower internal resistance and improved current handling. The material was inspired by the work of Bruno Scrosati *et al.* who claimed inserting Li ion into magnetite, Fe_3O_4 in 1980s. The inserted Li^+ ions must displace the tetrahedral-site Fe^{3+} ions of Fe_3O_4 into the empty 16c sites of the array to form an ordered rock-salt structure. Goodenough *et al.* demonstrated that the B_2O_4 spinel framework could be an insertion host for Li ions, using LiMn_2O_4 as an example which shows an open-circuit voltage of 3 V.³³ The Li^+ ion occupies the 8a tetrahedral sites of the spinel structure, and extraction of the Li from the tetrahedral sites gives a voltage of 4 V versus Li/Li^+ . Thus a step of 1 V in the energy of the $\text{Mn}^{4+}/\text{Mn}^{3+}$ redox couple occurs on shifting the Li^+ ions from tetrahedral to octahedral sites.³⁴

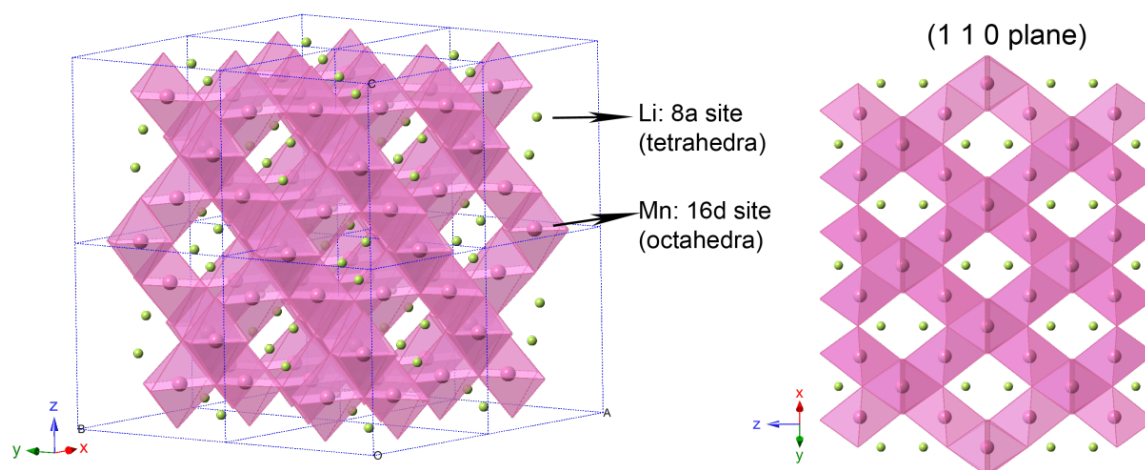


Figure 1.8 Crystal structure of LiMn_2O_4 .

LiMn_2O_4 has the spinel structure (space group: $Fd3m$) with the general formula AB_2O_4 , where A and B are cations occupying tetrahedral (8a) and octahedral (16d) site, respectively, in an intervening cubic close-packed array of O atoms (32e sites) (**Figure 1.8**). The interstitial space in the B_2O_4 framework can be seen as a network of tetrahedral 8a sites, which function as pathways for the transport of Li^+ ions in the structure.³⁵

Another advantage of LiMn_2O_4 is the high thermal stability and enhanced safety, but the cycle and calendar life are limited, which is due to Mn dissolution via the disproportionation reaction proposed by Hunt *et al.*³⁶: $2\text{Mn}^{3+} \rightarrow \text{Mn}^{2+} + \text{Mn}^{4+}$.

The spinel cathode LiMn_2O_4 is another popular candidate for the cathode of high-power LIBs for HEVs, even though under high drain rates its capacity is only around 80 mAh/g. This material has been plagued by self-discharge when left under full charge, particularly at elevated temperatures.³⁷

1.3.5 Olivines LiMPO_4

The attention in the community was changed radically in 1997 with the discovery of the electrochemical properties of the olivine phase, particularly LiFePO_4 , by Goodenough and Padhi *et al.*³⁸ This is the first cathode material with potentially low cost, earth-abundant elements and also environmentally friendly that could have a significant impact in electrochemical energy storage.²⁸

LiFePO_4 consists of a distorted hexagonal close-packed (hcp) O framework with 1/8 of the tetrahedral holes occupied by P, and 1/2 of the octahedral holes occupied by various metal atoms (in this case Li and Fe). Layers of FeO_6 octahedra are corner-shared in the bc plane and linear chains of LiO_6 octahedra are edge shared in a direction parallel to the b-axis. These chains are bridged by edge and corner shared phosphate tetrahedra, creating a stable three-dimensional structure (**Figure 1.9**).³⁹ Therefore, it is stable to high temperatures, not susceptible to be broken up on overcharge or discharge. Only under extreme discharge is the olivine structure destroyed; and even then, the phosphate group is maintained as lithium phosphate.⁹ There is only subtle structural change between LiFePO_4 and FePO_4 which leaves the 1D channels for Li^+ motion intact. This $\text{FePO}_4/\text{LiFePO}_4$ phase change provides a flat voltage plateau of 3.45 V vs. Li/Li^+ ,

well within the stability limits of many electrolytes, and also provides the exceptional cycling stability.

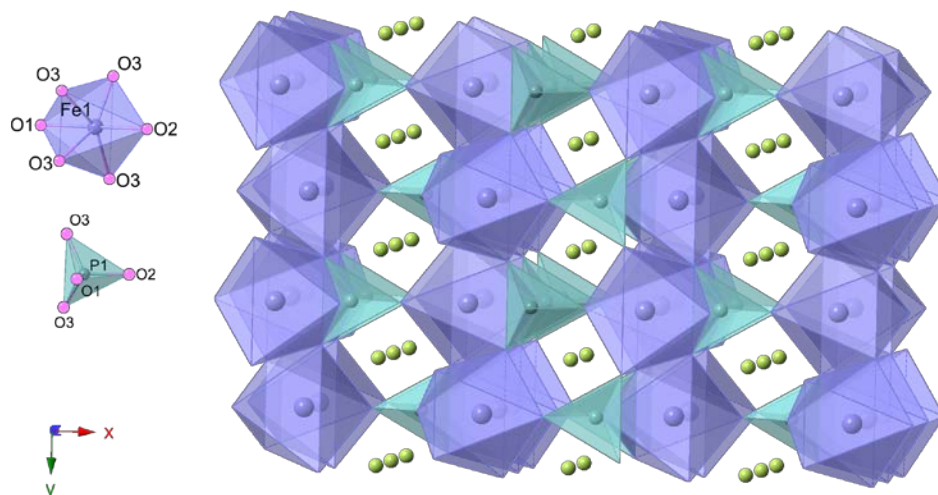


Figure 1.9 Crystal structure of LiFePO_4 .

However, LiFePO_4 is an electronic insulator (in the order of 10^{-9} S/cm at room temperature), which severely limits its rate performance in the first place. Extensive work has been done to improve it, among all, one successful and applicable approach is carbon coating.^{40,41} Besides, there is only 1D channel along b-direction for Li^+ diffusion in LiFePO_4 (**Figure 1.9**), which imposes two constraints: 1). the Li channels must not be blocked by either disorder of the Li and Fe atoms or by the presence of a foreign phase; and 2) the cathode particle must be small without stacking faults that block the channel.²⁷ Generally, LiFePO_4 obtained by low-temperature wet-chemistry route suffers from abundant Li-Fe anti-site defects, resulting in much lower specific capacities and slower rate-performance. Only after correcting those defects and proper carbon-coating, LiFePO_4 can approach its theoretic capacity (170 mAh/g) even under high current rates, which is typically realized by annealing LiFePO_4 together with carbonaceous compounds (*e.g.* sugars) at high temperature (around 700 °C) under protective atmosphere (slightly reducing environment).

LiFePO_4 has been successfully applied to power tools in the market. Extensive studies are now underway to commercialize this technology for HEVs/EVs, along with its strong competitors, *i.e.* NMC or LiMn_2O_4 .

Much of the discussion has centered on the Fe element of the LiMPO_4 olivine structure, but the transition metal may also be Mn, Ni, and Co. Ceder *et al.* predicted by calculations that the open-circuit voltages are 3.5 V for LiFePO_4 , 4.1 V for LiMnPO_4 , 4.8 V for LiCoPO_4 , and 5.1 V for LiNiPO_4 and band gaps of 3.7 and 3.8 eV for LiFePO_4 and LiMnPO_4 .^{42, 43}

1.3.6 Others

In the past decades, efforts on developing new cathode materials have never stopped. There are varied emerging types of cathodes. Among all, polyanion-type compounds are of particular interest, which are defined as a class of materials in which tetrahedral polyanion structure units $(\text{XO}_4)^{n-}$ and their derivatives $(\text{X}_m\text{O}_{3m+1})^{n-}$ ($X = \text{P, S, As, Mo, or W}$) with strong covalent bonding combine with MO_x ($M = \text{transition metal}$) polyhedra.⁴⁴ Polyanion cathode materials generally possess higher thermal stability than conventional layered transition-metal oxides due to the strong covalently bonded oxygen atoms, which make them more suitable for large-scale LIB applications, by virtue of their better safety properties.³⁹ **Table 1.3** summarizes some properties of polyanion compounds which have been investigated up to now.⁴⁴

Table 1.3 Properties of some polyanion compounds. Table is reproduced from Ref [44].

Polyanion compounds		Structure	Voltage (V) Li ⁺ /Li ⁰	Theoretical capacity/ practical capacity (mAh/g)		Thermal stability	Remark	
Phosphates	LiFePO ₄	Olivine structure, orthorhombic (space group <i>Pmn</i>)	3.5	170	>160	Excellent	Excellent cycling stability Instability of delithiated state and low cycling performance at high temperature high electrode potential, practical application will rely on the development of electrolytes with higher stability window	
	LiMnPO ₄		4.1	171	160	Good		
	LiCoPO ₄		4.8	167	120	Poor		
	LiNiPO ₄		5.1	169	-	-		
Silicates	Li ₂ FeSiO ₄	Li ₃ PO ₄ structure, tetrahedral (as much as 8 polymorphs)	2.8/4.8*	332	200	Excellent	Possible for two electron reaction (Fe ²⁺ /Fe ³⁺ /Fe ⁴⁺ redox couples), good cycling stability Poor cycling stability, amorphism upon delithiation Higher electrode potential, low electrochemical activity, poor cycling performance	
	Li ₂ MnSiO ₄		4.1/4.5*	333	250	-		
	Li ₂ CoSiO ₄		4.2/5.0*	325	100	-		
Fluorophosphates	Li(Na)VPO ₄ F	Triclinic (space group <i>P1</i>)	4.2	156	155	Excellent	Higher electrode potential, good cycling stability	
	Na ₃ V ₂ (PO ₄) ₂ F ₃	Tetragonal (space group <i>P4₂/mnm</i>)	4.1	192	120	-	Irreversibility of extraction of the third Na ⁺	
	Li ₅ V(PO ₄) ₂ F ₂	layered monoclinic (space group <i>P2₁/c</i>)	4.1	170 (V ³⁺ /V ⁴⁺ /V ⁵⁺) redox couples	70	-	Poor reversibility of V ⁴⁺ /V ⁵⁺ redox couple two-dimensional ion conduction paths and solid solution-like electrochemical behavior	
	Li(Na) ₂ FePO ₄ F	Layered or stacked or 3D structure was adopted depends on the alkali ion and transition metal ion	3.5	292	135	Good		
	Li(Na) ₂ MnPO ₄ F	-	-	-	-	Electrochemical inactive		
	Li(Na) ₂ CoPO ₄ F	-	5.0	287	120	Good		Both large theoretical capacity and high electrode potential, practical application will rely on the development of electrolytes with higher stability window
	Li(Na) ₂ NiPO ₄ F	-	5.3	287	-	-		

Fluorosulphates	LiFeSO ₄ F	Triclinic (space group <i>P1</i>)	3.6	151	135	Poor	Better ionic/electronic conductivity compared with LiFePO ₄
	LiMSO ₄ F (M = Co, Ni)	Triclinic (space group <i>P1</i>)	-	-	-	-	Electrochemical inactive
	LiMnSO ₄ F	Monoclinic (space group <i>P2₁/c</i>)	-	-	-	-	
Borates	LiFeBO ₃	Monoclinic (space group <i>C2/c</i>)	3.0	220	200	-	Solid-solution intercalation mechanism
	LiCoBO ₃	Monoclinic (space group <i>C2/c</i>)	-	215	-	-	Almost negligible electrochemical activity
	LiMnBO ₃	Hexagonal (space group <i>P6</i>)	-	222	110	-	A plateau around 4.3 V with limited capacity, most of the capacity lie in the voltage of 1.25 – 4.3 V

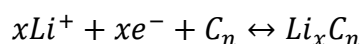
1.4 Anode/Negative Electrode

The μ_A of carbon lies above the LUMO of carbonate electrolytes. Due to the SEI layer formation on the carbon when introducing ethylene carbonate (EC) electrolyte to provide kinetic stability and its relatively cheap price, carbon materials are currently the most broadly used negative electrodes employed in LIBs. As a result of considerable chemical (pyrolytic processing) or physical (mechanical milling) modifications, the electrochemical performance of carbon negative electrodes has been improved continuously. Reversible capacities of ca. 350 mAh g⁻¹ for graphite are now being reached (theoretically 372 mAh g⁻¹ for the end compound LiC₆).

In parallel, ongoing research efforts are focused on searching for carbon alternatives in the hope of finding materials with both larger capacities and slightly more positive intercalation voltages compared to Li⁺/Li, so as to match the window of electrolyte and minimize any risks of high-surface-area Li plating at the end of fast recharge, which are associated with safety problems.⁴ This is surely at the cost of energy density. Generally, anodes used in LIBs are broadly classified into three main categories: intercalation, conversion, and alloy types based on the reaction mechanism with Li as shown in **Figure 1.10** and **Table 1.4**.

1.4.1 Carbon-based materials

Several reasons have made carbons to be the most attractive and investigated negative electrodes for the LIBs. First of all, carbon is a low cost material. Another advantage for the battery industry is that the redox potential of lithiated carbon materials is almost identical to that of metallic Li. Moreover, a good cycling stability is expected due to the high mechanical electrode integrity (compared to conversion- and alloy-types). The insertion of Li into carbon, often called intercalation, can be written as follows:⁴⁵



Many types of carbonaceous materials have been proposed. Within these we can distinguish between graphitic carbons and non-graphitic carbons. In graphitic carbons a maximum amount of Li corresponding to $x < 1$ in Li_xC₆ can be reached, giving a theoretical specific charge value of 372 mAh g⁻¹. During intercalation a change in the stacking order of the graphite layers, shifting from ABA to AAA, is observed. According

to equation above, the Li intercalation is reversible. In practice, more than the theoretical amount of Li is consumed during the initial discharge process. This extra amount cannot be recovered during the following charge. This irreversible specific charge, which depends on the electrolyte used, is explained on the basis of the reduction of the electrolyte solution and the formation of a SEI film at the Li_xC_6 interface. When the film is formed, the electrolyte reduction is suppressed and the electrode can be cycled reversibly.¹⁶

On the one hand this film is necessary to kinetically protect the electrode surface from further reduction prolonging the lifetime of the cell, but on the other hand the irreversible specific charge has to be kept at a low value, because all the Li source in a practical LIB is offered by the positive electrode, which is limited. The type of electrolyte used strongly affects the formation of the SEI film. For instance, propylene carbonate (PC) undergoes reduction at about 800 mV vs. Li^+/Li . At a slightly more negative potential intercalation of PC solvated Li ions into graphite occurs, leading to a large expansion of the graphite layers, and consequently, to the destruction of the graphite lattice. As a result, the SEI cannot serve as a reliable barrier. On the other hand, ethylene carbonate (EC) is reduced much faster than PC. Thus, the SEI is formed rapidly and stops further solvated Li intercalation. Since the viscosity of EC is quite high, mixtures with *e.g.* dimethyl carbonate (DMC) or diethyl carbonate (DEC) are often used.¹⁶

Among the non-graphitic carbons there are the so-called high specific charge carbons. Such carbons can show specific charges of about 400 to 2000 mAh g^{-1} , and are mainly obtained by pyrolysis of certain polymers or even ordinary sugar. These disordered structures contain isolated graphene layers on either side of which intercalated Li may undergo adsorption, *i.e.* “house of card” mechanism proposed by Dahn *et al.*⁴⁶ Such mechanisms can double the specific charge. The main problems of these high specific charge carbons are the very high irreversible specific charge and the poor cycling stability, hinting at the formation of stable LiC_x compounds. Nitrogen- or boron-doped carbons were also used as negative electrode. However, the specific charge of these materials rapidly diminished upon cycling.

These issues will be addressed in detail in Chapter 3 and 4.

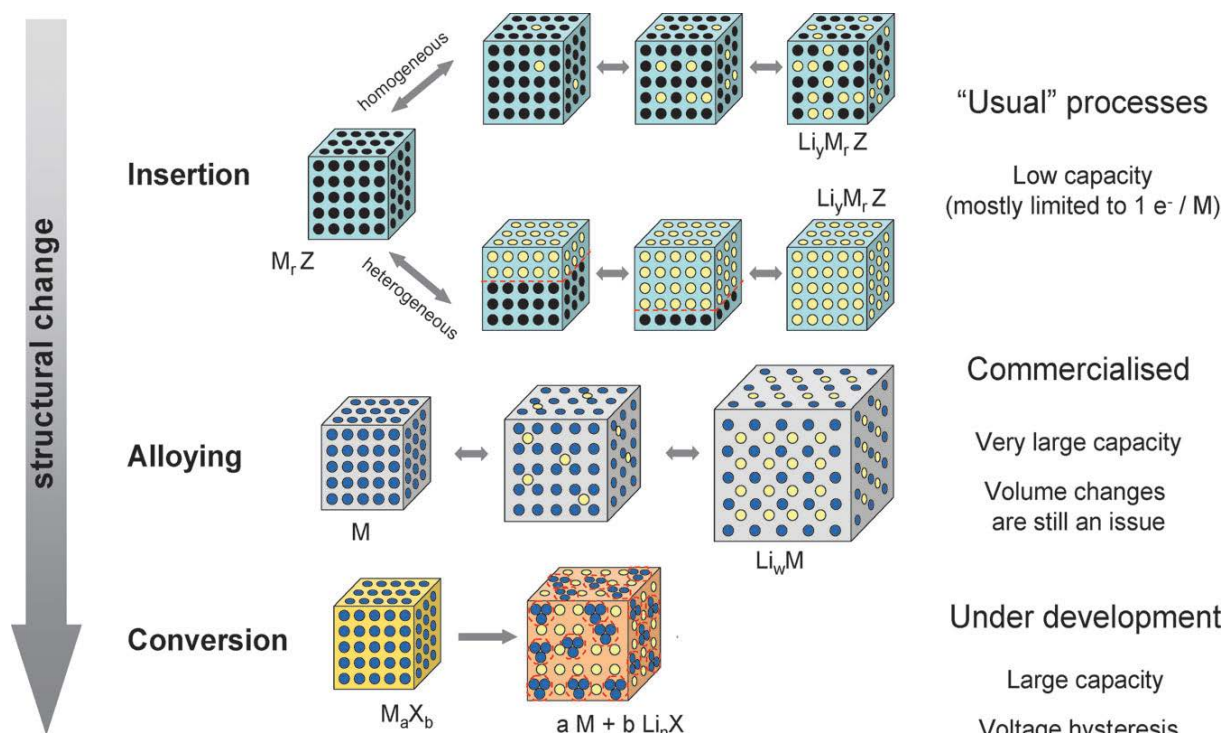


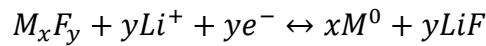
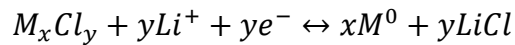
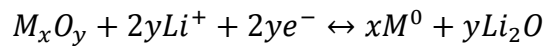
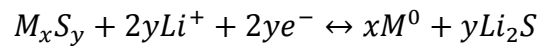
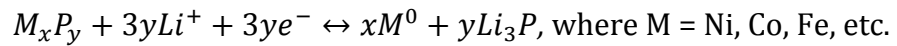
Figure 1.10 A schematic illustration of three different reaction mechanisms observed in anode materials for LIBs. Graph taken from Ref [8].

1.4.2 Non carbon-based materials

The most investigated classes of non carbon-based materials are conversion and alloy types electrode materials. The main motivation of using the conversion or alloy materials as negative electrode is that they can offer high capacity of Li storage. The major problems of these emerging electrodes arise from the huge difference in volume before and after Li insertion. In the case of silicon a volume change of about 320% is theoretically calculated.⁴⁷ As a result, mechanical stress and cracks are induced during cycling, which cause disintegration and hence loss of electrical contacts between particle-particle and between particle-current collector. To increase tolerance of stress-induced cracking and thus enhanced cyclability, one feasible solution is to reduce the particle size (nano-sizing). In addition, any physical or chemical approaches of overcoming the issues of reactant expansion should be beneficial, *e.g.* the strategy of nano-engineering of negative electrodes. This will be specifically addressed in more detail in the next part and Chapter 3.

i. Conversion-type

Conversion is a reversible electrochemical reaction (or often called a displacement reaction), where the transition metal comprising compound (MX_y , X = P, S, O, F, Cl etc.,) is electrochemically reduced to the form of a metal (M^0) upon the lithiation process (discharge).^{8, 48} During delithiation (charge), the reduced metallic nanoparticles are theoretically cycled back to its original state (MX_y), as shown in **Figure 1.10**. However, there is some debate regarding the final oxidation state after the first discharge process. Researchers argued that the complete reversibility back to the parent material is not possible; for instance in FeCo_2O_4 , reduction of Fe^0 and Co^0 is recorded after discharge; while FeO and Co_3O_4 only formed in subsequent cycles.⁴⁹ The overall and much simplified conversion mechanism for the various compounds is summarized as below:⁴⁸



Owing to the multiple electron reactions, such conversion type electrodes can offer higher reversible capacity than insertion type materials, (*e.g.* carbon-based materials). Similar to graphitic anode, irreversible electrolyte decomposition can not be avoided in the initial several cycles, particularly in the first one. The decomposition leads to the formation of a SEI layer over the active particle surfaces, which are predominantly composed of insoluble inorganic by-products, polymeric films, etc; whereas, the SEI layer formed over conversion anodes is entirely different from graphitic anodes. Associated with higher capacities, large volume variation, high redox potential, severe polarization and poor cyclability are other important issues for this type of anode. However, carbon coating or forming composites with carbonaceous material/passive elements is proposed to sustain the volume variation and thus enhanced stability upon extended cycles. As mentioned earlier, pre-lithiation of the electrode is one efficient method to solve the problem of the large initial irreversible capacity lost.

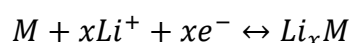
Indeed, conversion-type anodes certainly have several advantages over insertion type anodes, but overcoming the mentioned drawbacks remains a big challenge. In Chapter 3, we will describe specifically our efforts to solve the problems.

Table 1.4 Comparison of the theoretical specific capacity, charge density, volume change and onset potential of various anode materials. Table is summarized from Ref [16, 17, 50].

Materials	Lithiated phase	Potential range vs. Li ⁺ /Li [V]	Theoretical specific charge [mAh g ⁻¹]	Theoretical charge density [mAh cm ⁻³]	Density [g cm ⁻³]	Volume change [%]
Li (metallic)	Li	0	3862	2047	0.53	100
C	LiC ₆	0.05	372	837	2.25	12
Li ₄ Ti ₅ O ₁₂	Li ₇ Ti ₅ O ₁₂	1.6	175	613	3.5	1
Co ₃ O ₄	Co + Li ₂ O	- (>0.8)	890	5438	6.11	- (huge)
Fe ₃ O ₄	Fe + Li ₂ O	- (>0.8)	926	4630	5.0	- (huge)
Si	Li _{4,4} Si	0.4	4200	9786	2.33	320
Sn	Li _{4,4} Sn	0.6	994	7246	7.29	260
Sb	Li ₃ Sb	0.9	660	4422	6.7	200
Al	LiAl	0.3	993	2681	2.7	96
Mg	Li ₃ Mg	0.1	3350	4355	1.3	100
Bi	Li ₃ Bi	0.8	385	3765	9.78	215

ii. Alloy-type

Electrochemical alloying between Li and metallic or semi-metallic elements was proved feasible in a reversible manner in non-aqueous electrolytes in the 1970s, in parallel to the intense studies of intercalation compounds. The motivations are their high theoretical capacity and lower working potential (except graphite) compared to the insertion and conversion type anodes, especially for group IV elements (Si, Ge, Pb and Sn).^{8, 48, 50} The alloying reactions can be written as follows:



Despite the capacities derived from alloying reactions reaching values as high as 9786 mAh cm⁻³ and 4200 mAh g⁻¹ for Si, their practical utilization in secondary batteries is severely hindered by the dramatic volume changes accompanying with the alloying process (**Table 1.4**). For instance, the lithiation of Sn to the end product, Li_{4,4}Sn or

$\text{Li}_{4.2}\text{Sn}$ (still on debate), can expand up to 260%. This huge volume increase leads to a loss of contact between the grains and the current collector, and the disintegration of the composite electrodes, thus a very poor cycling performance. The strategies used to circumvent these issues can be found in many review papers, where the majority aims at tackling volume expansion.

1.5 Nanoengineering

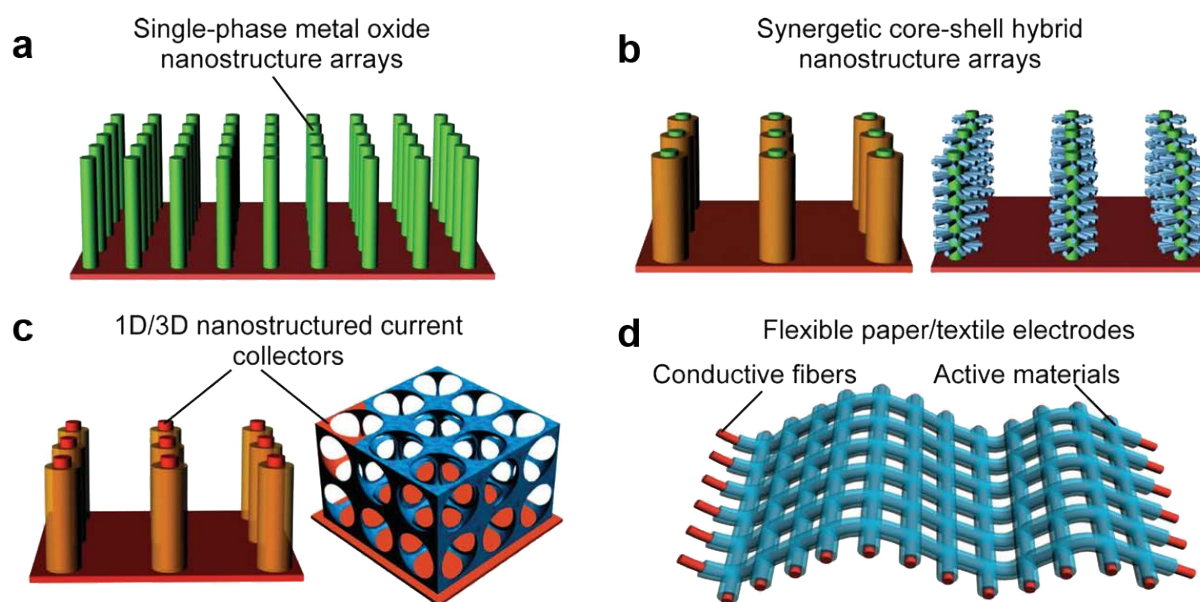


Figure 1.11 Several examples of nanostructured architecture design for LIBs. Graph cited from Ref [51].

In the past, most attempts to improve the design of LIBs tackled the issues at the macroscopic scale, but work now is much more focusing on the nanoscale. Nanomaterials and nanostructured hybrid electrode materials quickly entered the field of energy storage after 2000.¹⁵ Several examples of nanostructured electrode designs are given in **Figure 1.11**. Nowadays, the high-efficiency energy storage requires the devices to be able to store large quantities of electrical energy in small space and release the energy rapidly, which would never be realized without nanosizing and/or nano-coating and/or rational design of appropriate electrode materials. These strategies represent a promising avenue to enhance the battery performance, as they will bring several advantages.^{7, 51}

- They enable electrode reactions to occur that cannot take place for materials composed of micrometer-sized particles; for instance, reversible Li intercalation into mesoporous β -MnO₂ without destruction of the rutile structure.
- The reduced dimensions increase significantly the rate of Li insertion/removal, because of the short distances for Li-ion transport within the particles. The characteristic time constant for diffusion is given by $t = L^2/D$, where L is the diffusion length and D the diffusion constant. The time t for intercalation decreases with the square of the particle size on replacing micrometer with nanometer particles.
- Electron transport within the particles is also enhanced by nanometer-sized particles, as described for Li-ions.
- A high surface area permits a high contact area with the electrolyte and hence a high Li-ion flux across the interface.
- For very small particles, the chemical potentials for Li-ions and electrons may be modified, resulting in a change of electrode potential (thermodynamics of the reaction).
- The range of compositions over which solid solutions exist is often more extensive for nanoparticles, and the strain associated with intercalation is often better accommodated.

The employment of nanoengineering provides LIBs a leap in terms of capacity, power, cost and materials sustainability. However, the effective increase in the electrodes' surface area is at the expense of other disadvantages.⁷

- Nanoparticles may be more difficult to synthesize and their dimensions may be difficult to control.
- High electrolyte/electrode surface area may lead to more significant side reactions with the electrolyte, thus much lower initial Coulombic efficiency, and more difficulty maintaining interparticle contact.
- The density of a nanopowder is generally less than the same material formed from micrometer-sized particles. The volume of the electrode increases for the same mass of material thus reducing the volumetric energy density.

The down-sizing of particle size is only one possibility, the use of nanostructured hybrid electrode materials is the other one. The combination of both methods offers a promising avenue to boost the electrochemical performance of active electrode materials, as this strategy will synergistically strengthen the advantages of each component, but also mitigates their disadvantages. This will be specifically illustrated in Chapter 3 and 4.

1.6 Beyond Li

Li, an element known for about 200 years, is suddenly becoming a rising star elopement: it is the primary ingredient of the LIBs that power the next generation of HEVs/EVs and, as such, could become as precious as gold in this century.⁵² In addition, it is not uniformly spread within the Earth's crust: there is sparking rumors that Andean South American countries could soon be the 'new Middle-East'. Together, these factors set the scenario for controversial debates about the available reserves and the anticipated demands: if all cars are to become electric within 50 years, worries about a crunch in Li resources - and thus a staggering price increase such as that faced today with fossil fuels - are permeating.⁵²

Unlike Li, sodium (Na) is one of the more abundant elements on Earth and exhibits similar chemical properties to Li, indicating that Na chemistry could be applied to a similar battery system. In the 1970s-80s, both Na-ion and Li-ion electrodes were investigated, but the higher energy density of LIBs made them more applicable to small, portable electronic devices, and research efforts for rechargeable batteries have been mainly focused on LIBs since then. Recently, research attention in Na-ion batteries (NIBs) has been re-emerged, driven by new applications such as medium and large-scale stationary energy storage, and to address the concern on Li abundance.^{53, 54}

However, the larger size (116 pm for Na⁺ vs. 90 pm for Li⁺) and different bonding characteristics of Na-ions influence the thermodynamic and/or kinetic properties of NIBs, which leads to unexpected behavior in electrochemical performance and reaction mechanism, compared to their LIB counterparts. Besides, the heavier mass number (23 for Na⁺ vs. 6.94 for Li⁺, atomic mass unit) and higher redox potential (-2.71 V for Na⁺ vs. -

3.04 V for Li^+ , standard hydrogen electrode) lower the theoretical specific capacity and energy density of NIBs.⁵⁵

The topic is challenging, quite interesting though. We have some on-going research on it (in Chapter 6), but due to the limited time frame of my PhD study, this topic will not be touched in this dissertation.

Chapter 2 Tailoring Polymorphs of LiFePO_4 as Cathodes

2.1 Introduction

Since its discovery by Goodenough *et al.* in 1997,³⁸ olivine LiFePO_4 (denoted α -phase hereafter) has been extensively investigated as cathode material for lithium ion batteries in electric vehicles (EVs) owing to its high specific charge (170 mAh/g), high operating voltage (3.45 V vs. Li^+/Li), outstanding cyclability, low cost, environmental friendliness and intrinsic thermal safety.^{5,56} However, on the way to its practical application for power batteries olivine- LiFePO_4 suffers from low electronic conductivity (10^{-9} to 10^{-10} S/cm) and poor ionic conductivity (10^{-12} to 10^{-16} cm^2/s).⁵⁷ These issues typically are alleviated by particle size reduction, coating with a conductive layer (*e.g.* carbon layer⁵⁸⁻⁶⁰ or conductive polymer^{61,62}), and/or lattice modification (*e.g.* mainly cation doping^{63,64}). However, higher surface area comes at the expense of lower tap density and thus loss of volumetric energy density, and the suitability of the doping strategy is still controversially discussed.⁵⁷ Considering all these factors, a cathode consisting of micron-sized particles with a nano-sized hierarchical and porous architecture might represent a promising alternative for high-performance LIBs as well as for easy-processing on an industrial scale.⁶⁵ However, there are only few reports on LiFePO_4 particles with a self-assembled 3-dimensional structure.^{66,67} Such complex morphologies are generally achieved by solvothermal or hydrothermal routes with the assistance of surfactants or templates.⁶⁸

When high pressure (65,000 bar) and elevated temperature (900 °C) are applied to α - LiFePO_4 , it transforms into a high-pressure phase (denoted β -phase hereafter), which was discovered by Amador *et al.* in 2001.⁶⁹ More than 10 years later, in 2012, Haase *et*

The content of this chapter was published on *Chem. Mater.* **2013**, 25, 3399-3407 entitled "Tailoring Two Polymorphs of LiFePO_4 by Efficient Microwave-Assisted Synthesis: A Combined Experimental and Theoretical Study" with authorship G. Zeng, R. Caputo, D. Carriazo, L. Luo and M. Niederberger*.

al. developed a liquid-phase method of synthesizing $\beta\text{-LiFePO}_4$ at ambient pressure and low temperature.⁷⁰ To the best of our knowledge, the work of Amador and Haase are the only publications on that particular phase. They are mainly focused on the synthesis protocol and no information is given about the morphology of the β -phase particles.

In this chapter, we report a simple and elegant method to efficiently fabricate both polymorphs of LiFePO_4 in a controlled way. Employing a microwave-assisted non-aqueous route highly crystalline single-phase LiFePO_4 with the desired structure can be obtained in just 3 minutes by simply tuning the ratio of the two solvents, benzyl alcohol and 2-pyrrolidinone. The α - and β - phase form completely different morphologies, which provides an unique opportunity to compare their electrochemical properties in dependence of the particle shape. The powders of the two polymorphs are dispersed in an aqueous solution of glucose, directly deposited on the current collector, assembled into Swagelok half cells without any conductive additives and polymer binders and finally thermally annealed. To understand the behavior and properties of α - and β - LiFePO_4 , the experimental results were complemented by a theoretical study. The structures of the two phases were investigated by Density Functional Total Energy calculations to get their relative stabilities and structure differences at the atomistic level. A qualitative understanding of the poor electrochemical performance of the β -phase can be provided by the dynamics of the mobile Li ions in both structures.

2.2 Results and discussion

Microwave-assisted solvothermal syntheses have been proven to be an efficient approach for the synthesis of a great variety of inorganic compounds.^{71, 72} In surfactant-free systems, one way to alter the particle morphology is to change the solvents and/or the relative concentrations. In the case of LiFePO_4 the synthesis in benzyl alcohol (BnOH) leads to the formation of platelets⁷³ or sticks.⁷⁴

To prepare LiFePO_4 we used a stoichiometric amount of LiCl , Fe(II) acetate and H_3PO_4 and varying BnOH to 2-pyrrolidinone (2-Py) volume ratios. After a short heat treatment with microwave irradiation crystalline $\alpha\text{-LiFePO}_4$ was obtained at a solvent ratio of 4. If the ratio was changed to 1, then $\beta\text{-LiFePO}_4$ was obtained. Simply by altering the reaction medium, the phase can be tailored. The X-ray diffraction (XRD) patterns of the two as-

synthesized samples are shown in **Figure 2.1**. The refinements of the experimental patterns are listed in Table C.1 and C.2 (Appendix).

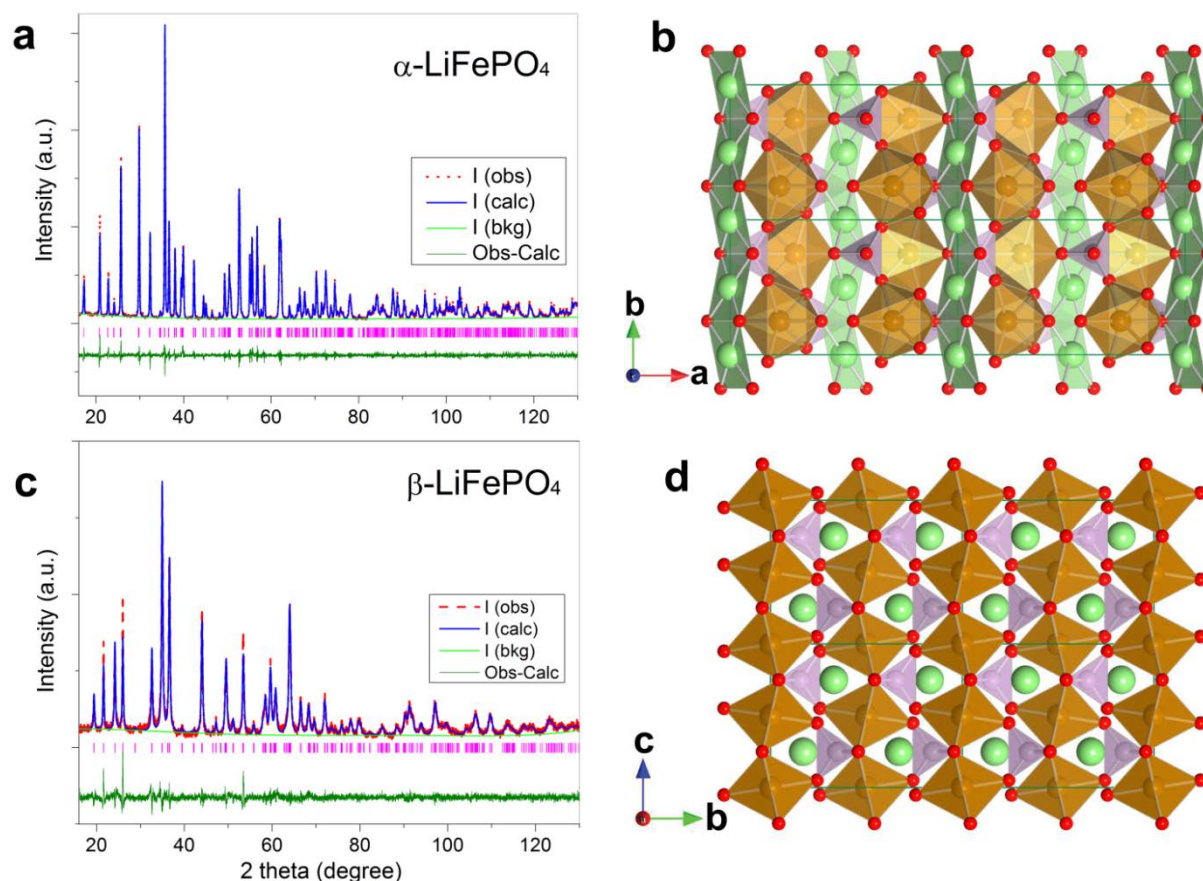


Figure 2.1 XRD patterns and crystal structures for α - and β - LiFePO_4 , respectively. Experimental XRD patterns (red lines) and Rietveld refinement (blue lines) for α - LiFePO_4 (a) and β - LiFePO_4 (c). Projected views along the crystallographic c-direction of α - LiFePO_4 (b) and the a-direction of β - LiFePO_4 (d) in which the octahedra $[\text{FeO}_6]$ are shown in brown, the tetrahedra $[\text{PO}_4]$ in violet and Li in green.

These two phases share the same orthorhombic symmetry but in different space groups, $Pnma$ (α) and $Cmcm$ (β), respectively. The main differences between the two structures concern the coordination of the cations. In $Pnma$, the cations, Li and Fe, are tetra- and octa-coordinated to O atoms, respectively. In fact, the $[\text{LiO}_6]$ octahedra are more distorted than the $[\text{FeO}_6]$ ones, the distortion index in bond length is 0.013 \AA in the former and 0.008 \AA in the latter. For that, the coordination of Li atoms is better represented as quadratic planar (see **Figure 2.1b**) with mean bond length Li-O of 2.112 \AA and distortion index of 0.002 \AA . The $[\text{LiO}_4]$ planes share an edge between them and a corner with the tetrahedra $[\text{PO}_4]$ and octahedra $[\text{FeO}_6]$. In $Cmcm$, the tetrahedra $[\text{LiO}_4]$ share a corner with the nearest $[\text{FeO}_6]$ octahedra, which in turn share an edge between

them. At DFT-D level of calculations, the average bond lengths of Li-O and Fe-O are 2.075 Å and 2.044 Å, with distortion index of 0.068 Å and 0.022 Å, respectively.

A distinguished structural difference, which is relevant for the electrochemical properties, is the relative distance between the Li atoms. In the orthorhombic $Cmcm$ the shortest distances between Li atoms, as reported in Table C.3 (Appendix), are larger than in the α -phase, too large for an effective Li-Li long range interactions and hopping mechanism as suggested for explaining the diffusion of Li in FePO_4 .^{75,76} In **Figure 2.1** a projection along the crystallographic c - and the a -direction of the two structures are shown, respectively. Interestingly, the inclusion of the dispersion contributions (DFT-D) overestimates the long-range interactions along the crystallographic a - and b -directions, along which Li atoms are displaced, with the largest and the shortest distances, respectively. The effect is reflected into shorter a , b lattice parameters compared to the experimental ones. On the other side, by using the local spin density approximation (LSDA) plus the on-site Coulomb parameter U , the lattice parameters are overestimated. The structure details are reported in Table C.4 and Table C.5 for α - and β - phase, respectively (Appendix).

Recently, the structure features of LiFePO_4 have been explained by using the extended Zintl-Klemm concept,⁷⁷ for which the β - LiFePO_4 structure can be rationalized by assuming one-electron transfer from the Li atoms to the P atoms. The two symmetry groups representing the two structures α and β are related by symmetry, being $Cmcm$ one of the minimal non-isomorphic supergroups of the $Pnma$ symmetry group, but they do not transform one into the other by simply exchanging the cation positions.

In addition, the orthorhombic $Pnma$ structure has been recently discussed by several authors both experimentally and theoretically⁷⁸⁻⁸¹ by introducing the question of anti-site defects and site exchange between Li (4a) and Fe (4c) atoms. Clearly, the site exchange can be made possible only in an off-stoichiometric compound, in which Li vacancies might allow the migration to or the occupancy in the (4a) sites by Fe atoms. As pointed out by Chung *et al.*⁷⁹ the occupancy of the (4a) sites by Fe brings in an additional electrostatic repulsion because of a difference valence. Furthermore, site exchange and Li-vacancy on the (4a) sites inevitably induces a deterioration of the

electrochemical properties due to a depletion of the ionic carriers on the preferential pathway of Li diffusion.

The de-lithiated form iron(III) phosphate (FePO_4) has also been extensively studied for different Li contents.⁸²⁻⁸⁵ Among the different polymorphs of FePO_4 ,^{83, 86} the symmetry groups *Pnma* and *Cmcm* represent the host lattice of the corresponding lithiated structures. The optimization of the two orthorhombic FePO_4 structures reported in literature^{83, 84, 87} showed that at DFT-D level of calculations they differ by 90.12 kJ/mol, being the structure with symmetry group *Cmcm* lower in energy. Table C.6 in Appendix presents the structure data of FePO_4 in the two crystallographic symmetry groups after full geometry optimization. The configuration with edge-sharing $[\text{FeO}_6]$ octahedra in the *Cmcm* symmetry is energetically preferred over the corner- and edge-sharing between $[\text{FeO}_6]$ octahedra and $[\text{PO}_4]$ tetrahedra in the *Pnma* structure. Reversely, the lithiated phases showed a lower total energy in the *Pnma* symmetry than in the *Cmcm* one, as reported in Table C.3. The enthalpies of absorption of one mole Li in the orthorhombic *Pnma* and *Cmcm* structures of FePO_4 , at DFT-D level of calculations, are -379.88 kJ/mol and -279.08 kJ/mol to form respectively the α - and β - LiFePO_4 . Generally, the specific energy density reported in literature⁸⁸ is 578 Wh/kg for the α -phase, which corresponds to 328.26 kJ/mol for the absorption of one mole Li in the *Pnma* FePO_4 , a value which falls in the range of our DFT-D calculations. For the β -phase, the expected energy density, calculated from the above reported enthalpy, will be 2.89 V for the same absorption reaction of one mole Li in the *Cmcm* FePO_4 . In fact, the cathodic reaction Li^+/Li can be considered as the reverse reaction of absorption of Li in FePO_4 , in the ideal case of a completion reaction. The exact numerical correspondence with the experimentally determined potentials can be improved by considering the free energy of reaction at (P,T) experimental conditions instead of the internal energy at (P,T) equal to zero.

Interestingly, not only the phase can be tailored by this route, but also the size and morphology of the particles as shown in **Figure 2.2**. Pristine α - LiFePO_4 crystallizes into submicron-sized plates with lengths of 400-600 nm, widths of 140-180 nm and several nanometers in thickness (**Figure 2.2 a, b**). On the other hand, the β - LiFePO_4 displays a bow tie-like particle morphology with an open, 3D porous microstructure (**Figure 2.2c**). The particles are symmetric and exhibit a narrow size distribution with lengths of 2-3

μm (**Figure 2.2d**). Every particle consists of self-assembled blades with nanospace in between. Such well-organized morphology facilitates the penetration of the electrolyte into the electrode particles, offering a larger interface between electrode and electrolyte. Generally, in the electrode materials design, nanoparticles are advantageous, because they offer shorter diffusion path to Li-ions. Therefore, higher rate performance is expected. However, down-sizing also brings some problems. On the one hand, higher surface area comes at the expense of volumetric energy density and lower tap density. Controversies regarding the toxicological assessment of nanoparticles hamper their industrial processing in comparison to microparticles. Micron-sized particles consisting of hierarchically ordered nanoparticles, additionally arranged into a porous 3D structure as offered by $\beta\text{-LiFePO}_4$ is believed to be ideal. It combines the advantages of nanoparticles with the benefits of microparticles.

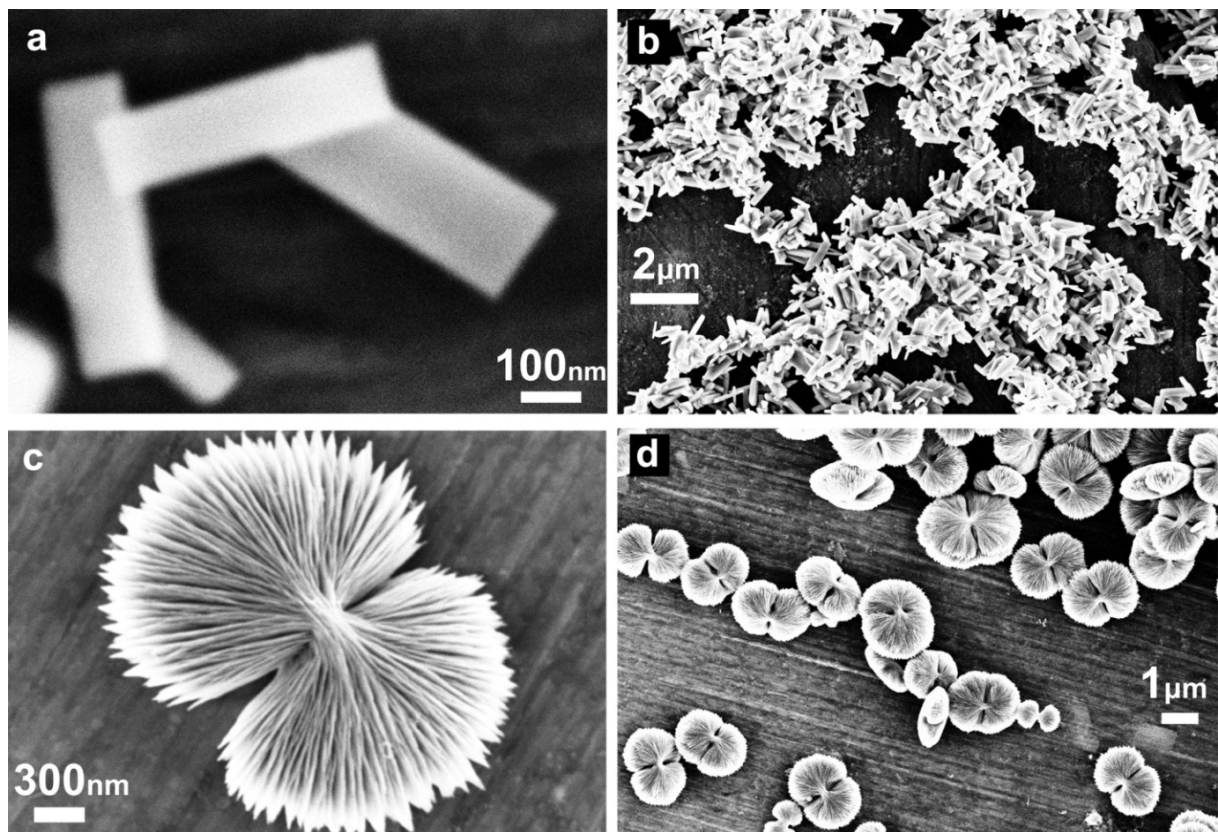


Figure 2.2 Representative SEM images for $\alpha\text{-LiFePO}_4$ and $\beta\text{-LiFePO}_4$. SEM images of $\alpha\text{-LiFePO}_4$ at high (a) and low magnifications (b). SEM images of an individual particle of $\beta\text{-LiFePO}_4$ with the bow tie-like morphology (c) and overview of several particles with sizes of 2-3 μm (d).

Downsizing to the nanoscale and 3D open porosity is beneficial from the Li-ion diffusion point of view. But to enhance the rate performance and to alleviate over potential upon

cycling, electronic conductivity is also required. However, α -LiFePO₄ is an insulating material (1.6×10^{-7} S/cm at 55 °C to 1.4×10^{-4} S/cm at 210 °C, Figure C.1 in Appendix). The conductivity of β -LiFePO₄ lies in the same range (2.9×10^{-7} S/cm at 55 °C to 1.3×10^{-4} S/cm at 210 °C, Figure C.1). To tackle this issue, coating the particles with carbon⁵⁸⁻⁶⁰ or conductive polymer^{61, 62} is generally employed. Here we used a simple, yet effective, approach to carbon-coating the particles. The as-synthesized powders were mixed with aqueous glucose solution, directly dropped onto the current collector and dried. The sugar wrapped-particles were annealed in N₂ at high temperature. During the annealing, glucose decomposed into amorphous carbon that is homogenously distributed on the pristine particles with full preservation of the morphologies (**Figure 2.3**). At the same time, the particles were connected together and glued to the current collector. This approach for electrode preparation makes a large number of typically used additives such as expensive binders (PVDF (polyvinylidene fluoride) or PTFE (polytetrafluoroethylene)), carbon blacks and minor toxic solvents like NMP (N-Methyl-2-pyrrolidone) superfluous.

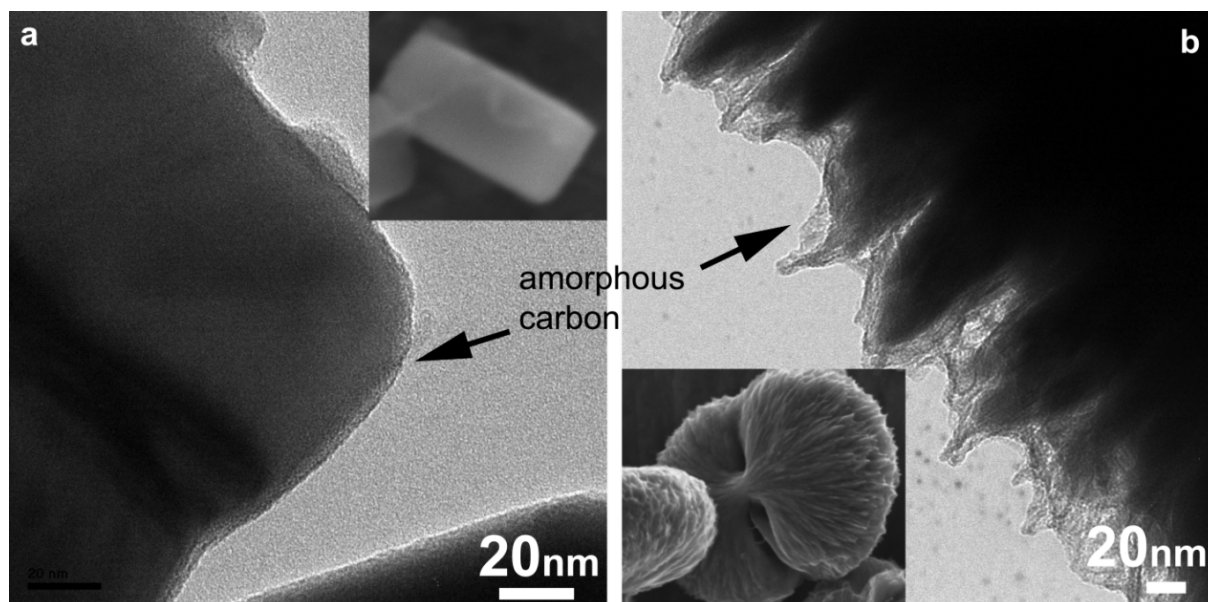


Figure 2.3 Carbon coating on LiFePO₄ particles. TEM images of the thin layer of amorphous carbon homogenously coated on the surface of α -LiFePO₄ (a) and β -LiFePO₄ (b). Insets: SEM images of the particles after heat treatment and carbon coating.

The quality of the carbon layer is highly dependent on the annealing temperature. Higher annealing temperatures usually result in more conductive carbon layer. However, the β -phase undergoes a phase transition to the α -phase above 475 °C, this

temperature has to be considered as the limit for the carbon coating process. In addition, higher annealing temperatures lead to the formation of $\text{Fe}_2\text{P}_2\text{O}_7$ as an impurity phase (**Figure 2.4**). Therefore, the annealing temperature for the $\beta\text{-LiFePO}_4$ was set at $450\text{ }^\circ\text{C}$ only, whereas at such low temperature, the decomposition of the glucose into amorphous carbon is incomplete.⁸⁹ The carbon-coated sample (denoted as $\beta\text{-LiFePO}_4@450$ hereafter) was brown and exhibited little improved electronic conductivity ($2.9\times 10^{-7}\text{ S/cm}$ at $55\text{ }^\circ\text{C}$ to $3.4\times 10^{-5}\text{ S/cm}$ at $210\text{ }^\circ\text{C}$, Figure C.1). Annealing $\beta\text{-LiFePO}_4$ at $550\text{ }^\circ\text{C}$ caused the phase-transition to $\alpha\text{-LiFePO}_4$ with better electronic conductivity ($9.2\times 10^{-6}\text{ S/cm}$ at $55\text{ }^\circ\text{C}$ to $1.7\times 10^{-4}\text{ S/cm}$ at $210\text{ }^\circ\text{C}$, Figure C.1, denoted as $\beta\text{-LiFePO}_4@550$ hereafter). Annealing pristine $\alpha\text{-LiFePO}_4$ with sugar at $650\text{ }^\circ\text{C}$ resulted in a black film with the best electronic conductivity ($5.1\times 10^{-3}\text{ S/cm}$ at $30\text{ }^\circ\text{C}$ to $2.0\times 10^{-2}\text{ S/cm}$ at $210\text{ }^\circ\text{C}$, abbreviated as $\alpha\text{-LiFePO}_4@650$ below). A typical carbon loading was $\sim 10.2\text{ wt\%}$ determined by TGA (see Figure C.2 in Appendix).

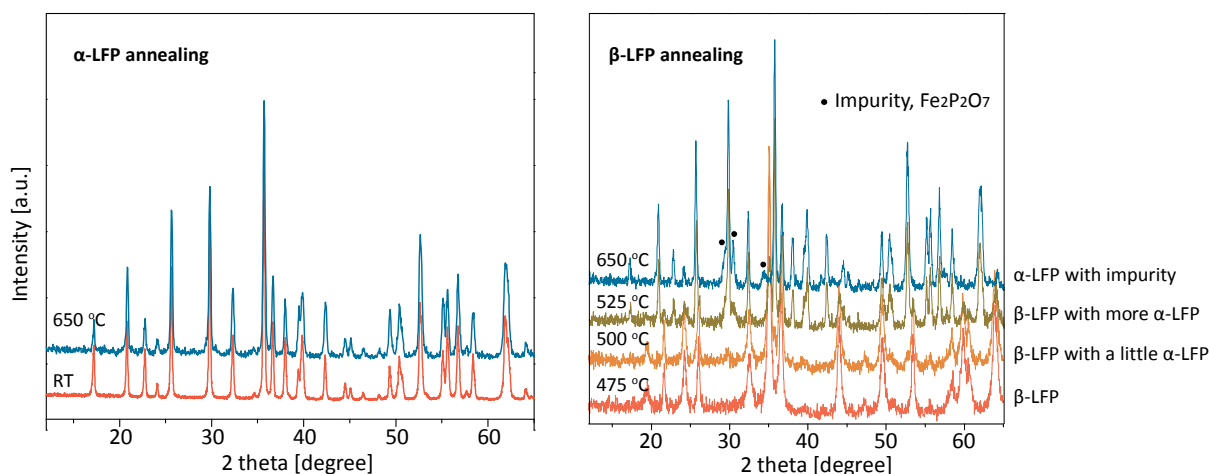


Figure 2.4 Temperature dependent XRD patterns for $\alpha\text{-}$ and $\beta\text{-LiFePO}_4$, respectively.

Besides carbon coating, annealing is effective to increase the crystallinity of the as-synthesized materials; meanwhile, reduce the anti-site defects existing in LiFePO_4 . Generally, LiFePO_4 prepared *via* wet chemistry routes typically exhibit a higher possibility of Fe-Li anti-site defect. As mentioned earlier in the text, such anti-site defect is disadvantageous for the Li-ion diffusion,^{90,78} and thus poor electrochemical performance as shown later.

In the first paper about $\beta\text{-LiFePO}_4$,⁶⁹ Amador *et al.* claimed that it was electrochemically inactive up to 5.1 V. Although they did not present any information about the particle

morphology, it can be assumed that the harsh reaction conditions applied to the solid-state-process (900 °C and 65 kbar) result in large particle sizes with unfavorable electrochemical properties. On the other hand, Haase *et al.*⁷⁰ proposed that β - LiFePO_4 is Li-ion intercalation active. They obtained 32 mAh/g in a cyclic voltammetry scan at 0.1 mV/s. They calculated a mean domain size of 20 nm, strongly agglomerated, but no electron microscopy images were provided. To clarify the behavior of both phases, we performed electrochemical measurements and compared the results.

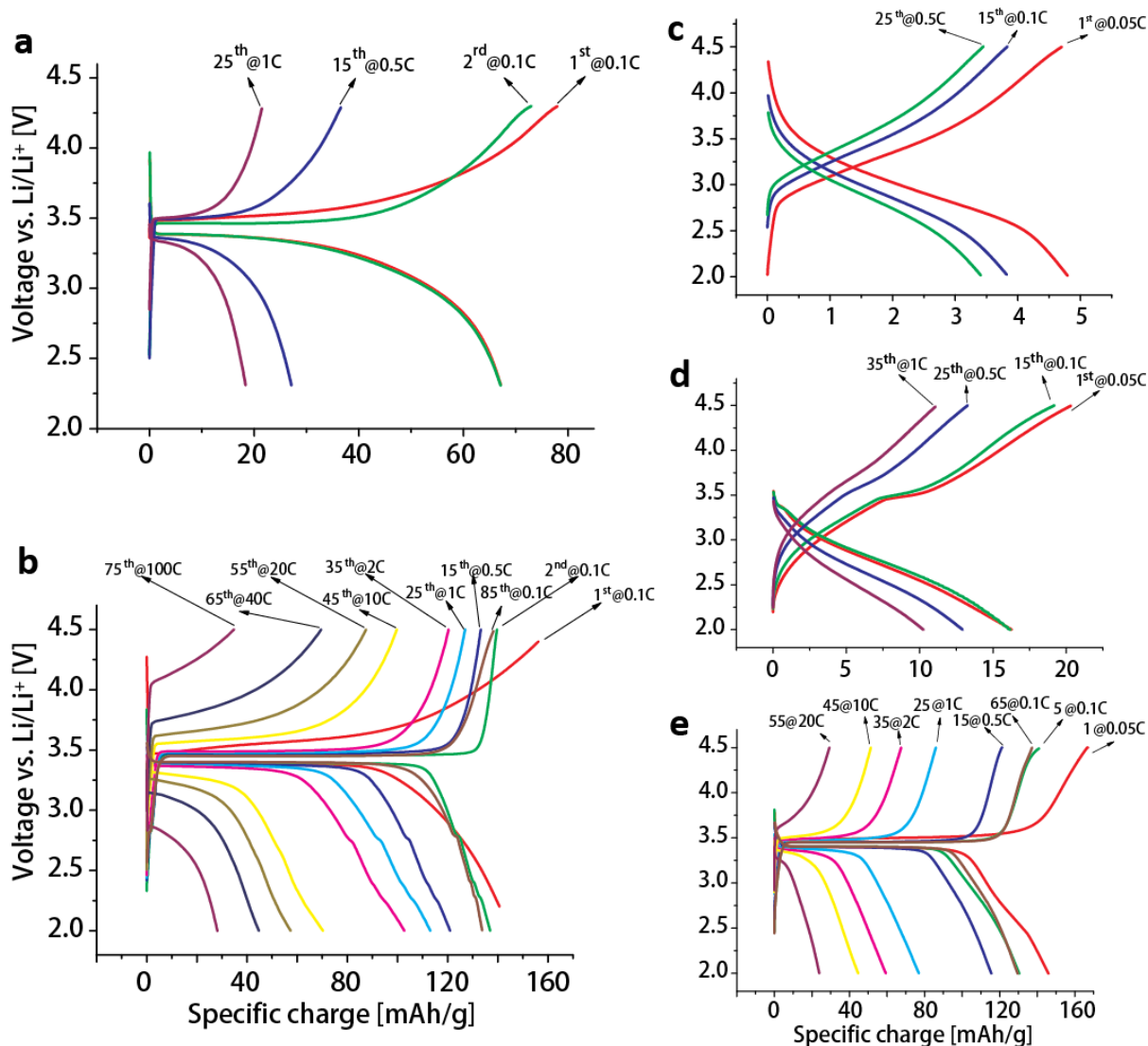


Figure 2.5 Galvanostatic cycling tests for all types of electrodes at different current rates: As-prepared α - LiFePO_4 (a) and carbon-coated α - LiFePO_4 (b); pristine β - LiFePO_4 (c), carbon-coated β - LiFePO_4 (d) and α - LiFePO_4 obtained from β - LiFePO_4 by annealing (e).

Firstly, the galvanostatic cycling was tested for pristine α -LiFePO₄ and β -LiFePO₄. The respective rate performances are shown in **Figure 2.5 a** and **c**. α -LiFePO₄ displayed the characteristic plateau at 3.45 V with a reversible specific charge/discharge of ~ 70 mAh/g at 0.1 C, ~ 30 mAh/g at 0.5 C and ~ 20 mAh/g at 1C, respectively (1C = 170 mA/g). The moderate performance is understandable, considering the lack of any heat treatment and absence of a conductive layer coating (although carbon black was added for the electrode preparation). Although the β -LiFePO₄ possesses hierarchical porous microstructure, surprisingly, it delivers even worse capacities of less than 5 mAh/g at 0.05 C, ~ 4 mAh/g at 0.1 C and ~ 3.5 mAh/g at 0.5 C. Besides, β -LiFePO₄ does not show any indication for a clear charge/discharge plateau. This result is comparable to the work of Amador *et al.*⁶⁹

The annealed α -LiFePO₄@650 demonstrated much enhanced cycling performance, reversibly delivering a specific discharge of ~ 137 mAh/g at 0.1 C, ~ 121 mAh/g at 0.5 C, ~ 114 mAh/g at 1 C, ~ 103 mAh/g at 2 C, ~ 71 mAh/g at 10 C, 58 mAh/g at 20 C, 45 mAh/g at 40 C and ~ 29 mAh/g at 100 C. After these high-rate cycles, it fully recovered to ~ 134 mAh/g at 0.1 C (**Figure 2.5b**). In sharp contrast to C-coated α -LiFePO₄, the C-coated β -LiFePO₄@450 still showed a poor electrochemical behavior. It delivered a discharge capacity of ~ 16 mAh/g at 0.05 C, ~ 16 mAh/g at 0.1 C, ~ 13 mAh/g at 0.5 C and ~ 10 mAh/g at 1 C (**Figure 2.5d**). These values are only slightly improved compared to pristine β -LiFePO₄. A closer look at the charge profile in **Figure 2.5d** reveals a plateau at ~ 3.5 V. Although the heat treatment was carried out at 450 °C only, this observation points to the presence of α -LiFePO₄, as demonstrated by cyclic voltammetry tests later.

β -LiFePO₄ transforms into α -LiFePO₄ at temperatures above 475 °C (**Figure 2.4**), with full preservation of the complex particle morphology. To take advantages of such hierarchical microstructure for the Li-intercalation active α -phase, β -LiFePO₄ was annealed and C-coated at 550 °C (denoted as β -LiFePO₄@550 below). After the heat treatment, it reversibly delivered a specific discharge of ~ 145 mAh/g at 0.05C, ~ 130 mAh/g at 0.1 C, ~ 120 mAh/g at 0.5 C, ~ 80 mAh/g at 1 C, ~ 60 mAh/g at 2C, ~ 50 mAh/g at 10 C and ~ 25 mAh/g at 20 C, and returned to ~ 130 mAh/g at 0.1 C after the high-rate cycles (**Figure 2.5e**). In spite of the hierarchical morphology, which is expected to be ideal for the electrochemical properties, β -LiFePO₄@550 does not outperform α -LiFePO₄@650. One reason is the presence of minor amounts of Fe₂P₂O₇, which does not

contribute to the specific charge in the cathode window.^{91,92} Moreover, an annealing temperature of 550 °C is too low to form well conducting amorphous carbon layer, neither not high enough to completely remove the anti-site defects hampering Li ion diffusion. Nevertheless, considering the large particle size of $\beta\text{-LiFePO}_4@550$ in the range of several micrometers, the performance is comparable to a nanomaterial, which was one of the primary goals of this work.

Figure 2.6 shows the cycling properties at different current rates for all types of electrodes. $\alpha\text{-LiFePO}_4@650$ and $\beta\text{-LiFePO}_4@550$ exhibit an outstanding cycling performance. These results are comparable to the flowerlike or walnut-shaped LiFePO_4 recently reported by Goodenough *et al*,⁶⁵ to the hollow spheres lately reported by Lee *et al*,⁹³ and better, especially at high current rates, than those of microspheres with double coating⁹⁴ and porous LiFePO_4/C microspheres synthesized by Yu *et al* using a sol-gel method.⁹⁵ It is worthwhile to underline again that our electrodes were prepared without any additives. At faster cycling, the columbic efficiency drops. The gap between charge and discharge capacity could be reduced by insertion of a potentiostatic step until the current decreased to 0.1 C. The columbic efficiency for $\alpha\text{-LiFePO}_4@650$ is ~96% and ~94% for $\beta\text{-LiFePO}_4@550$ (see Figure C.3).

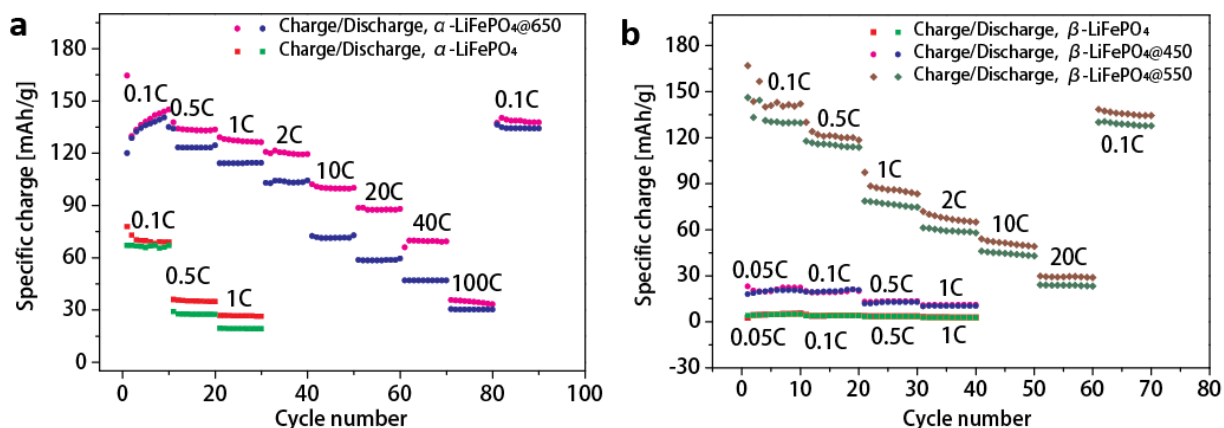


Figure 2.6 Galvanostatic cycles at various C-rates for all electrodes: As-prepared $\alpha\text{-LiFePO}_4$ and carbon-coated $\alpha\text{-LiFePO}_4$ (a); pristine $\beta\text{-LiFePO}_4$, carbon-coated $\beta\text{-LiFePO}_4$ and $\alpha\text{-LiFePO}_4$ obtained from $\beta\text{-LiFePO}_4$ by annealing (b).

To further clarify the electrochemical behavior of LiFePO_4 , particularly of the β -phase, cyclic voltammetry tests were carried out, providing information about the redox reactions during the electrochemical process. As shown in **Figure 2.7a**, $\alpha\text{-LiFePO}_4$

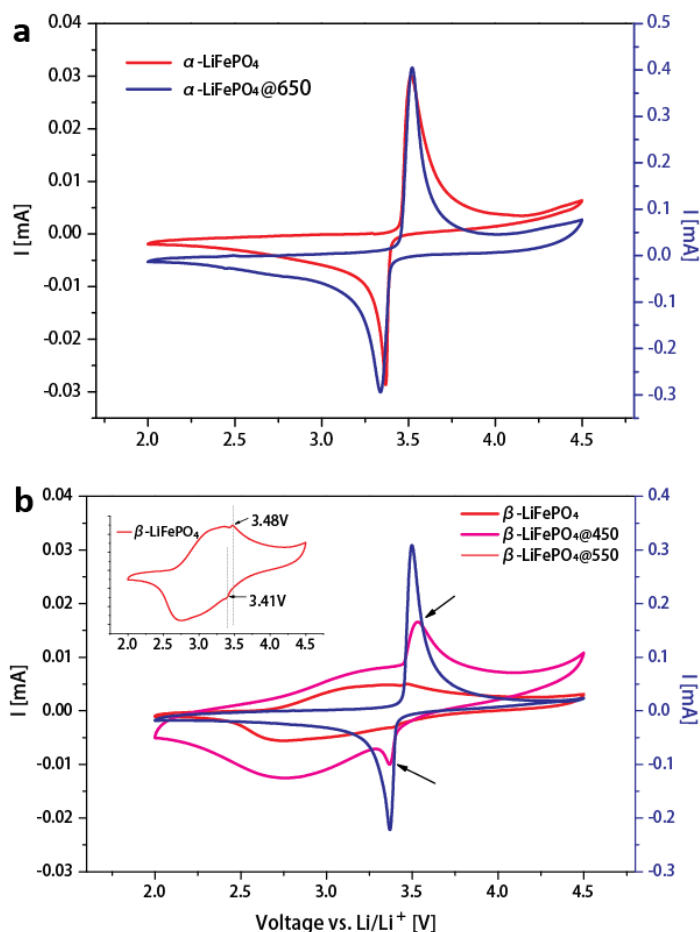


Figure 2.7 Cyclic voltammograms for as-prepared and annealed $\alpha\text{-LiFePO}_4$ (a), pristine and annealed $\beta\text{-LiFePO}_4$ (b). All scans were performed at a rate of 0.05 mV/s. Inset (b): Rescaled cyclic voltammetry scan for $\beta\text{-LiFePO}_4$.

$\beta\text{-LiFePO}_4$ is nearly electrochemically inactive. $\beta\text{-LiFePO}_4$ annealed at 450 °C showed a little higher specific charge. However, its cyclic voltammogram displays more significant shoulders at 3.48 V and 3.41 V (Figure 2.7). This explains the appearance of a plateau at 3.5 V in the galvanostatic cycling profiles, thus providing more capacity than pristine $\beta\text{-LiFePO}_4$. When $\beta\text{-LiFePO}_4$ transformed into the α -phase at 550 °C, as already demonstrated in the galvanostatic test, its cyclic voltammetry profile also resembled that of $\alpha\text{-LiFePO}_4$.

To better understand the two phases and the differences of their properties, especially the poor electrochemical performance of the β -phase, we performed DFT-based molecular dynamics calculations. The two different displacements of the Li ions in the α

presents the characteristic oxidizing peak at 3.52 V and the reducing peak at 3.37 V, independent of the heat treatment. The inset of Figure 2.7b shows the rescaled CV profile for pristine $\beta\text{-LiFePO}_4$ with much broader redox peaks. Anodic and cathodic peaks are located at lower voltages compared to $\alpha\text{-LiFePO}_4$, approximately at 3.4 V and 2.7 V, respectively. Noticeably, the voltammogram has two shoulders at 3.48 V on the anodic peak and at 3.41 V on the cathodic peak. This feature indicates the presence of trace amounts of $\alpha\text{-LiFePO}_4$ in the bow tie-like β -phase, which is, however, below the detection limit of XRD. Accordingly, $\alpha\text{-LiFePO}_4$ contributes to the capacity of the pristine $\beta\text{-LiFePO}_4$, confirming that

and in the β structures suggest, as confirmed later experimentally, a different mechanism for Li ion diffusion. In fact, in the *Pnma* (α) structure the particular sites $4a$ in $(0, 0, 0)$ occupied by Li enable a cooperative motion along the b -direction, suggesting that this is the preferred pathway of diffusion, a sort of confined tunnel displaying linear chains of Li atoms. Therein, they sit exactly at the center of mass of the nearest six O atoms to form edge-sharing $[\text{LiO}_6]$ octahedra, as drawn in Figure C.4 in Appendix. The Li ions diffuse uniaxially along the b -direction, where Li ions hop between octahedral sites *via* a tetrahedral void formed by the edge-sharing $[\text{LiO}_6]$ octahedra.⁹⁰ One-dimensional diffusion was first reported in theory⁹⁶ and later confirmed in experiments.⁹⁷ In all three crystallographic directions Li atoms are collinear, but only along the $[0\ 1\ 0]$ direction the Li-Li distance is shorter (see Table C.3 in Appendix).

In the *Cmcm* (β) structure, the $4c$ sites at $(0, 0.674, 0.25)$ allow a linear displacement of Li atoms along the $[1\ 0\ 0]$, $[0\ 1\ 0]$, $[0\ 0\ 1]$ directions, with Li-Li distances equal to the lattice parameters a , b , c , respectively, as shown in Figure C.5. Differently from the *Pnma* structure, in all those three directions Li atoms do not directly interact, but their polyhedra of coordination, which are distorted tetrahedra, share a corner with the next tetrahedra of the $[\text{PO}_4]$ groups. In fact, Li atoms are coordinated to O atoms in a very distorted tetrahedral configuration, in which the Li-O shortest distance is 1.933 Å (DFT-D) and 2.025 Å (LSDA+U). Only along the $[0\ 1\ 1]$ direction the Li atoms can directly interact, along which they are displaced in a staggered configuration with the shortest Li-Li distances. The short Li-O distance, which is comparable with the Li-O distance in Li_2O , can be a further argument for which a poor mobility of Li ions has to be expected in the β - structure. In fact, as confirmed by molecular dynamics at different sampling temperatures (10 K, 300 K, 850 K), in the *Pnma* symmetry the motion of Li ions are concerted and cooperative along the $[0\ 1\ 0]$ direction, whereas in the *Cmcm* symmetry Li atoms rattle into the voids without the possibility of hopping. In addition, they do not exactly sit on the center of mass of the nearest O atoms, as it is the case in the *Pnma* symmetry, but they are shifted from it by 0.669 Å. Increasing the temperature up to the value of the experimentally observed phase transition (475 °C), the stretching and bending modes of the P-O bonds, in particular, make Li ions move faster, but without the possibility to jump or interact with the motion of the nearest Li ions, which are about 4.0 Å apart.

As the collinear displacement is one of the structural requirements to ensure a fast and cooperative mobility of Li ions in a host lattice. We computationally searched for other possible model structure exhibiting the required collinearity of Li atoms, but keeping the *Cmcm* symmetry space group representation. One of the possible model structures with a shorter Li-Li distances was obtained by locating Li atoms initially on the 4b sites at (0.5, 0, 0) of the *Cmcm* structure of FePO_4 . The structure data, after full optimization, in the standard representation are reported in Table C.7 in Appendix. Interestingly, the total energy of the corresponding optimized structure at DFT-D level is 175.49 kJ/mol higher than the β -structure. Nevertheless, the enthalpy of absorption of Li into the orthorhombic *Cmcm* structure of FePO_4 to form the latter structure is -193.71 kJ/mol, compared to -279.08 kJ/mol of the β -structure. That enthalpy of absorption corresponds to the specific energy density of 341.09 Wh/kg.

Clearly, to tune at best the electrochemical properties, the structure requirements of the Li-collinearity and the thermodynamic stability need to be combined with reversible structural changes upon delithiation-lithiation processes. The new *Cmcm* structure, being an example of a more systematic investigation of structure prediction for materials design, is less stable than the β -structure, for which possesses less specific energy density, but, as the Li atom displacement along the c-direction might suggest, an improved Li mobility is expected. Instead, in the new *Cmcm* structure the s- and p-orbitals of Li and O atoms overlap at lower energy than in the β - LiFePO_4 , indicating that a higher energy is required to activate the motion of Li atoms. Therefore, the new *Cmcm* structure, expected to be a local minimum between the two lower energy structures, if experimentally achievable can be one of the reasons of the deterioration of the electrochemical properties.

The comparison of the calculated XRD patterns (see Figure C.7 in Appendix) of the new *Cmcm* structure with the two orthorhombic structures α and β , as optimized after the refinement of the corresponding experimental XRD patterns, suggests that the new *Cmcm* structure is a local minimum structure between the two lower energy structures.

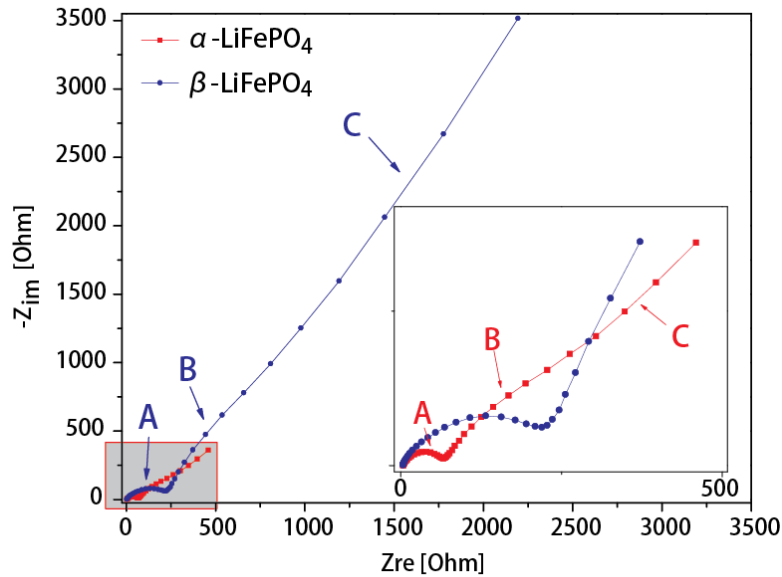


Figure 2.8 EIS spectra of α - and β - LiFePO_4 with enlarged section at high frequencies (inset).

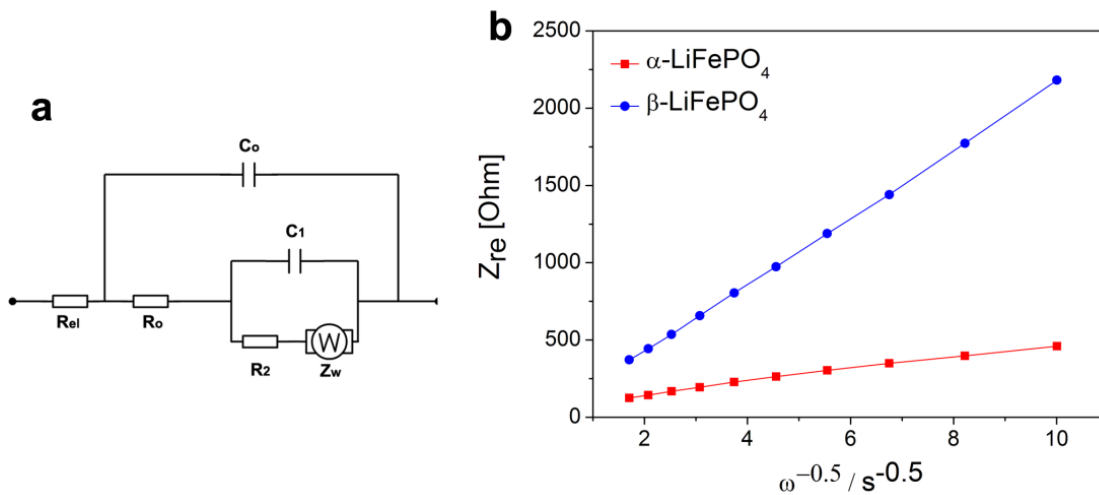


Figure 2.9 Simplified-contact-Randles (SCR) equivalent circuit for fitting the experimental EIS spectra (a). Relationship between Z_{re} and $\omega^{-0.5}$ at low frequencies (b).

To further demonstrate that β - LiFePO_4 is inactive in Li (de)intercalation, electrochemical impedance spectroscopy (EIS) was performed with α - LiFePO_4 as a reference sample. **Figure 2.8** compares the EIS spectra of the two phases in the frequency range from 0.01 Hz to 100 kHz with amplitude of 5 mV. At very high frequencies one observes a resistive intercept, R_o , which is due the ohmic resistance of the electrolyte. Then a semicircle appears at high frequencies (region A). It is generally associated either with the interface between the electrolyte and the active particles or

the charge-transfer resistance coupled with double-layer capacitance. It is more correct to ascribe it to the interface between the metal current collector and the active electrode.^{98,99} Region B at middle frequencies is mainly due to the presence of a conductive coating around the active particles and the contribution of inter-particle contacts giving rise to electronic resistance. The appearance of this region indicates that active particle-to-particle contacting/wiring is not perfect. Consequently, we cannot simply employ a simplified-contact-Randles (SCR) equivalent circuit as proposed in **Figure 2.9a**.⁹⁹ At low frequencies, a diffusional tail (Region C) dominates the response. The inclined line is attributed to the diffusion of Li-ions into the active electrode particles, the so-called Warburg diffusion. Z_{re} is proportional to $\sigma_w \omega^{-0.5}$, where σ_w is the Warburg coefficient and ω is the frequency. Therefore, in a plot Z_{re} vs. $\omega^{-0.5}$ the slope is the Warburg coefficient σ_w (**Figure 2.9b**). The Li ion diffusion coefficient can then be calculated according to the equation:

$$D = 0.5 \left(\frac{RT}{AF\sigma_w C} \right)^2$$

where R is the gas constant (8.314 J mol⁻¹K⁻¹), T is the temperature (295K), A is the area of the electrode surface, which is obtained by BET surface area measurement (see Figure C.6 in Appendix), F is the Faraday's constant (96,500 C/mol) and C is the molar concentration of Li ions in LiFePO₄, which can be calculated. The calculated Li ion diffusion coefficient is 1.9×10^{-15} cm²s⁻¹ for α -LiFePO₄ and 1.3×10^{-18} cm²s⁻¹ for β -LiFePO₄. The diffusion coefficient of β -LiFePO₄ is three orders of magnitude lower than that of α -LiFePO₄. Combined with its poor electronic conductivity, it illustrates why β -LiFePO₄ is almost electrochemically inactive.

2.3 Conclusion

Whereas the olivine-type LiFePO₄ has extensively been studied, the properties of the other polymorph crystallizing in the $Cmcm$ symmetry group are much less known. Here we present an easy way to access both phases of LiFePO₄ by a time-efficient microwave-assisted nonaqueous process. Depending on the solvent used, not only the crystal structure varies, but also the particle morphology. Having a material with the same composition, but different crystal structures and particle shapes at hand makes it

possible to directly compare the influence of these parameters on the electrochemical performance as cathode material in Li-ion batteries. Although the β - LiFePO_4 presents a sophisticated, hierarchically self-assembled bow tie-like morphology, which is expected to be ideal for lithium ion battery applications, it is electrochemically almost inactive. DFT-based molecular dynamics calculations at different sampling temperatures indicated that in the $Cmcm$ symmetry Li ions were only able to rattle in the voids without the possibility of hopping. On the other hand, α - LiFePO_4 offered excellent electrochemical performance after carbon coating in spite of the relatively simple platelet-like morphology. According to the calculations, in the $Pnma$ (α) symmetry the motion of Li ions are concerted and cooperative along the $[0\ 1\ 0]$ direction. After thermal transformation of β - LiFePO_4 into the α -phase, the electrochemical performance is greatly improved. However, the performance is not superior to the one of the α - LiFePO_4 platelets, although the complex morphology of the β -phase was preserved. This observation suggests that the morphology is less important than a suitable crystal structure providing high lithium mobility. But one has to keep in mind that in our case the quality of the carbon coating is not the same for the α - LiFePO_4 platelets and the bow tie-like α - LiFePO_4 obtained from the β -phase. As a matter of fact, considering that the carbon coating on the bow tie-like α - LiFePO_4 was produced at lower temperature resulting in the same electrochemical performance highlights the importance of an optimized particle morphology.

2.4 Experimental section

Chemicals: LiCl (99.9%, anhydrous), iron(II) acetate (99.995%), H_3PO_4 (99.999%), benzyl alcohol (99.8%, anhydrous, BnOH) and 2-pyrrolidinone (99%, anhydrous, 2-Py) were purchased from Sigma-Aldrich, stored in a glovebox filled with Ar (H_2O and $\text{O}_2 < 1\text{ppm}$) and used as received without further purification.

Synthesis: In a typical synthesis of α - LiFePO_4 , 4.0 ml of BnOH and 1.0 ml of 2-Py were mixed and added to stoichiometric amounts of precursors: 0.5 mmol LiCl (21.2 mg), Fe(II) acetate (87.0 mg) and H_3PO_4 (49.0 mg) in a 10 mL microwave glass tube equipped with a Teflon cap. The precursors were completely dissolved in the mixture of solvents under magnetic stirring after about 30 min, which was carried out in the glovebox to avoid oxidation of Fe(II). Outside the glovebox, the transparent green solution was then heated up under microwave irradiation and continuous stirring to 50 °C for 5 min, followed by a step at 195 °C for 3 min, using a CEM Discover reactor operating at 2.45 GHz. The grey precipitate was harvested by centrifugation and washed once with acetone and twice with

ethanol. The samples were dried in a vacuum oven at 60 °C overnight. For the synthesis of $\beta\text{-LiFePO}_4$, 2.5 ml of BnOH and 2.5 ml of 2-Py was employed while all other parameters were kept the same. Green products were obtained finally.

Carbon coating & Annealing: 30 wt% of glucose monohydrate (puriss) was dissolved in deionized H_2O and 70 wt% of LiFePO_4 was added and homogeneously mixed under mechanical stirring for 3 minutes. 0.1 ml of the as-prepared suspension was then transferred onto a petri dish-like titanium current collector with diameter of 13 mm and depth of 1 mm. The suspension was dried out in a vacuum oven at 60 °C and a thin film was directly formed on the current collector. It was calcined in a tube furnace at different temperatures (450 °C, 550 °C or 650°C) in N_2 for 6 hours with ramping rate of 3 °C/min. It resulted in brown or black (depending on the temperature) thin films with overall mass load of $\sim 2.5 \text{ mg/cm}^2$. These films on current collectors were directly used as electrodes without any additional additives.

Electrochemical Measurements: For non-carbon coated samples, 12.5 wt% of carbon black (Super P, TIMCAL), 12.5 wt% of binder (PVDF, Aldrich) and 75 wt% of pristine LiFePO_4 was uniformly mixed in N-methyl-2-pyrrolidinone (NMP, Fluka) under mechanical stirring. The resulting paste was either transferred onto petri dish-like Ti current collectors or doctor-bladed onto Al foil. After drying at 80 °C overnight under vacuum, circular electrodes with diameters of 13 mm were punched out and assembled into Swagelok-type cells in an argon-filled glove box in the case of doctor-bladed films. Lithium metal (99.9%, Alfa-Aesar) served as both reference and counter electrode. A fiber glass separator was soaked with electrolyte (1 M LiPF_6 in 1:1 wt% ethylene carbonate (EC)/dimethyl carbonate (DMC), Novolyte). All electrochemical measurements (galvanostatic cycling, cyclic voltammetry and impedance spectroscopy) were performed using a Biologic instrument (VMP3) at room temperature. The electrodes were cycled between 2.0 and 4.5 V vs. Li/Li^+ for varying specific current rates (1C = 170 mA/g).

Characterizations: X-Ray powder diffraction (XRD) patterns were recorded using a PANalytical diffractometer (PW 1800 with monochromator, $\text{Cu K}\alpha$ radiation). The morphologies were recorded by a LEO 1530 Gemini scanning electron microscope (SEM) working at 5kV and by a Philips CM 12 transmission electron microscope (TEM) at 100 kV. Nitrogen gas sorption to obtain the specific surface area by the BET method was measured on a Quantachrome Autosorb-iQ-C-XR. The carbon contents were determined by thermogravimetric analysis (TGA, Q500, TA Instruments).

Computational approach: In order to compare the relative stability, the two structures as to the lattice parameters and the atomic positions were optimized using DFT-based code CASTEP.¹⁰⁰ We used norm-conserving pseudo-potential and reciprocal space representation for all atoms. The core region is the $n = 1$ orbital for all atoms, except for Fe for which the $n = 2$ is also included, leaving accordingly 16 electrons into the valence region. The Brillouin zone is sampled by using a fine mesh commensurate to the specific lattice dimensions, but with the actual spacing below 0.02 \AA^{-1} . The energy threshold, the maximum atomic displacement, the maximum atomic force and the lattice stress were set to be 0.001 meV per atom, 0.001 Å, 0.001 eV/Å and 0.002 GPa, respectively. We used the generalized gradient form (GGA) of the exchange-correlation functions and in particular

Perdew-Burke-Ernzerhof96 (PBE), as implemented in CASTEP code. As being formed by charged groups, namely the cations Li and Fe, and the polyanion net of $[\text{PO}_4^{3-}]$, after the Coloumb energy, the most long range contribution to the total energy is the dispersion term. Non-covalent forces and in particular van der Waals interactions were introduced by using damped atom-pairwise dispersion corrections of the form C_6R^{-6} , proposed by Grimme¹⁰¹ as implemented in CASTEP. In addition, as it is well known the limitation of DFT in properly describing the band gap for highly correlated systems, we used the Local Spin Density plus the Hubbard U parameter, which for the valence d orbital of Fe was set to 2.5 eV. Furthermore, by using the Reflex powder diffraction module, implemented in Materials Studio 6.0, we simulated the XRD patterns of the optimized structures and performed the Rietveld refinement of the experimental XRD patterns. In the simulations, we used the X-ray radiation for the Cu source with $\lambda_1 = 1.5406 \text{ \AA}$ and $\lambda_2 = 1.5444 \text{ \AA}$, as set in the experiments.

Chapter 3 Spinel-Type Metal Oxides as Anodes

3.1 Introduction

Technological improvements in lithium-ion batteries are driven by an ever-increasing demand for portable electronic devices and electric vehicle applications.⁵ The main challenge remains in developing electrode materials with higher capacity, faster rate performance and longer lifespan.^{102, 103} Higher capacity means more Li uptake per transition metal or carbon, thus a larger change in the oxidation state is associated with the transition metal. As a result, the mechanism changes from classical intercalation, as in the case of *e.g.* C/LiC₆ or Li₄Ti₅O₁₂/Li₇Ti₅O₁₂, to conversion (*e.g.* Co₃O₄/Co), and alloying (*e.g.* Sn/Li_xSn). Besides metal oxides, transitional metal sulfides (*e.g.* MoS₂), also hold particular interest as conversion-type materials for LIB application.^{104, 105} In sharp contrast to interlayer/interstitial Li insertion with only small or even zero strain, an abrupt structural change take places upon electrode discharging for metal oxides/sulfides undergoing conversion, *e.g.*, reaction of Co₃O₄ to metallic Co and formation of Li₂O.^{106, 107} Consequently, high-energy density anodes suffer from mechanical degradation due to lithiation-induced volume expansion, electrode pulverization and detachment from the conducting environment during long-term cycling, resulting in large irreversible capacity loss, low Coulombic efficiency and poor cycling stability. In addition, low Li⁺ and e⁻ conductivity is generally associated with metal oxides, which limits the high-rate performance.⁵¹ Extensive attempts to tackle the issues have been focused on nanosizing the materials,⁷ *e.g.*, by preparing nanoparticles (NPs), nanowires, or nanotubes, owing to their enhanced electrode kinetics. However, reduction of the particle size alone cannot prevent severe capacity fading upon

The content of this chapter was published on *ACS Nano* **2015**, *9*, 4227-4235 entitled "[A General Method of Fabricating Flexible Spinel-Type Oxide/Reduced Graphene Oxide Nanocomposite Aerogels as Advanced Anodes for Lithium-Ion Batteries](#)" with authorship G. Zeng, N. Shi, M. Hess, X. Chen, W. Cheng, T. Fan and M. Niederberger*.

prolonged high-rate cycling due to drastic volume changes coming along with the conversion/alloying reaction. A variety of appealing strategies have been utilized to address the issues, among which the carbon-based nanocomposites is the most popular approach.¹⁰⁷⁻¹¹¹ For example, graphene anchored with Co_3O_4 NPs presented enhanced reversible capacity and cyclic performance as anode for LIBs.¹⁰⁷ However, to achieve large reversible capacity combined with high Coulombic efficiency, elongation cycling life together with good rate capability of conversion-type electrode materials still remains a great challenge. The optimization of the three-dimensional (3D) electrode architecture has been recognized as critical on the way to achieve superior performance of LIBs, particularly with hierarchical porous electrodes.⁵¹ For example, Yi *et al.* proposed a pomegranate-like Si-C hybrid electrode with a nanoscale design in which each single Si particle was encapsulated in a spacious hollow carbon shell to leave enough room for expansion upon Li uptake, leading to extraordinary cyclability.¹¹² The key to success is the presence of enough void space or porosity in the electrode, which facilitate electrolyte diffusion while maintaining good electron transport and accommodating large volume changes.

Nowadays, there is also growing interest in lightweight and flexible LIBs to meet the special needs for high-performance and flexible electronics, such as wearable devices or implantable biomedical devices.^{103, 113} However, to fabricate a flexible electrode with high-efficiency additional requirements have to be considered. The appropriate - often nanoscale - electrode material and the electrode architecture have to be engineered into a robust, but yet flexible form. Hierarchical-structured mesoporous carbon-based materials, particularly graphene or carbon nanotubes, with controlled pore features on the micron and nanometer scales, are preferred candidates to be integrated with active materials owing to their high e^- conductivity and excellent mechanical stability.¹¹⁴⁻¹¹⁷ For instance, Cheng *et al.* built a flexible hybrid electrode based on a 3D porous graphene framework *via* a complicated template-assisted CVD procedure, which finally resulted in outstanding electrochemical (EC) performance.¹⁰³ To build up hierarchical porosity generally sophisticated techniques, such as soft/hard templating, followed by acid etching or heat treatment, are usually required.

Here we present a simple and general method to fabricate flexible reduced graphene oxide (rGO) - spinel-type metal oxide nanoparticle (NP) aerogel composites as

advanced anodes overcoming several of the limitations discussed before. In this work, a monolith of rGO-based composite aerogel with embedded spinel-type metal oxide nanoparticles was designed and directly used as binder-free anode. The interconnected rGO sheets can offer a hierarchical porosity, and the introduction of NPs as spacers/pillars between rGO interlayers plays a critical role to prevent the hierarchical structure from collapsing. As a result of this design, synergistic effects are expected to lead to high capacity and long-term cycling stability of the electrode.

3.2 Results and discussion

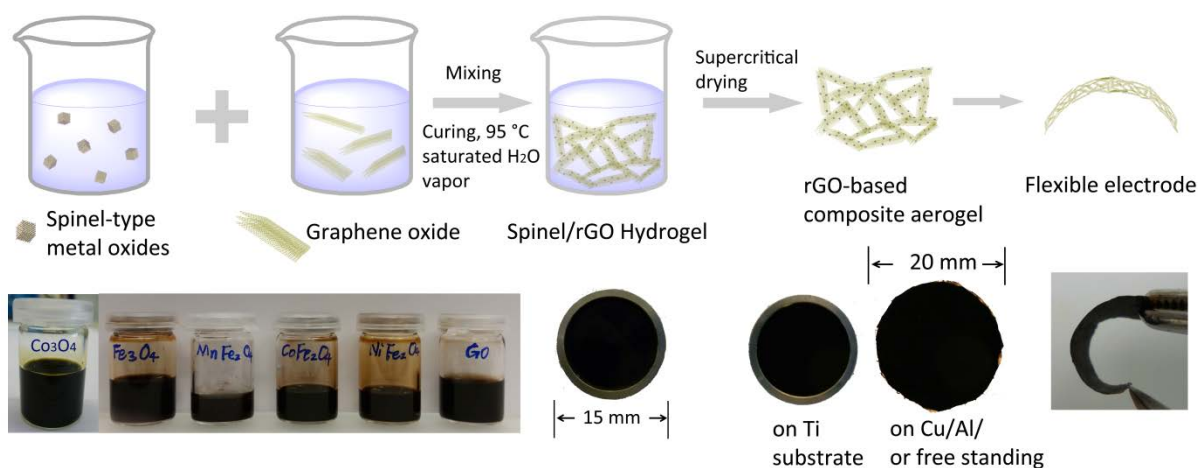


Figure 3.1 Schematic illustration of the fabrication process for spinel/rGO nanocomposite aerogel films. Colloidally stable spinel-type NPs and GO dispersions are used as building blocks. The combined suspension is cured under a saturated H₂O vapor environment at 95 °C for 6 hours, leading to a monolithic gel film. After supercritical drying, a flexible rGO-based composite aerogel with a rationally controlled shape is obtained. The free standing aerogel films can be bent without breaking.

The fabrication protocol of rGO-based composite aerogels is simple, as shown in **Figure 3.1**. First, colloidally stable suspensions of NPs are needed, which can be obtained through tailoring the surface chemistry of NPs, *e.g.*, tuning the surface charge to be positive. The positively charged metal oxide NPs later can be intimately combined with aqueous dispersion of negatively surface charged GO. In addition to electrostatic attraction between these two building blocks, π - π interactions between the GO sheets support the self-assembly process. Upon gelling in a mold at 95 °C, the NPs are homogeneously integrated into the interconnected rGO network, forming a monolithic

film of hydrogel. However, as already reported before for nanoparticle-based metal oxide aerogels,¹¹⁸⁻¹²⁰ it is critical to carefully tune the different interactions between the building blocks to get an efficient gelling process. After supercritical drying, a crack-free and flexible aerogel film (minimum ~ 100 μm in thickness) was obtained, which was directly used as the electrode without any further additives. The shape of the as-obtained composite aerogels is dependent on the shape of the containers and their substrates. A film or a bulk composite aerogel can be made on different substrates, *e.g.* Ti, Cu, Al, or even a free standing one can be produced if a Teflon container is used (details can be found in the experimental part). The interconnections of the graphene sheets offer enough mechanical strength and flexibility, so that the composite aerogel film can be bent or twisted without breaking.

This modular approach starting from preformed building blocks is rather different to other GO based composite aerogel preparation routes, where typically the NPs are hydro- or solvothermally grown on GO from molecular precursors.¹²¹⁻¹²⁴ This seemingly small experimental detail has a profound effect on the electrode preparation. In the latter case, the as-synthesized powders have to be processed into the electrodes by grinding/milling with binder, typically resulting in electrodes with lower porosity, and thus limited improvement in EC performance. In our case, the composite aerogel is directly assembled in the desired electrode geometry, preventing the use of binders and thus giving access to electrodes with high porosity and good mechanical flexibility.

To achieve high homogeneity at the nanoscale in the final composite, colloiddally stable NP suspensions are the prerequisite. For this purpose, we developed a novel synthesis route for Co_3O_4 NPs, where Co(II) acetate was dissolved into a mixture of benzyl alcohol and ammonia solution, followed by heating in an oil bath at 165 $^\circ\text{C}$ for 2 hours. After rinsing and drying, a black powder was obtained, which could be identified by powder X-ray diffraction (XRD) as Co_3O_4 (ICDD PDF No. 01-073-1701, **Figure 3.2a**). The broad reflections are characteristic for small nanocrystals. The crystallite sizes are estimated to be 5 nm calculated from the (4 0 0) and (4 4 0) reflections using the Scherrer equation, which is consistent with the results from transmission electron microscopy (TEM) as depicted in **Figure 3.2b**. The Co_3O_4 NPs exhibit a cube-like morphology, a low degree of agglomeration and a narrow particle size distribution with an average size of 4.6 nm. Owing to the positive charge on the surface, as confirmed by the ζ -potential

measurement (**Table 3.1**), the Co_3O_4 NPs can be dispersed into H_2O at high concentrations up to 30 mg/ml without any surfactants and they are stable for several weeks (**Figure 3.1**). The other spinel-type ferrites (MFe_2O_4 , $\text{M} = \text{Mn, Fe, Co}$ and Ni) were prepared by a slightly modified microwave-assisted benzyl alcohol route reported before.¹²⁵ The respective metal organic precursors and a small amount of ethylenediamine were dissolved in benzyl alcohol and heated at 195 °C for a few minutes under microwave irradiation. The NPs were identified by XRD as Fe_3O_4 (ICDD PDF No. 00-01-1111), MnFe_2O_4 (No. 00-10-0319), CoFe_2O_4 (No. 00-01-1121), and NiFe_2O_4 (No. 00-03-0875), respectively. The as-obtained ferrites display similar cube-like morphology like the Co_3O_4 NPs, however with a broader size distribution (see Figure D.1 in Appendix). But in contrast to cobalt oxide, the as-obtained ferrites could not be well dispersed in H_2O in the required high concentrations. Therefore, 2-(2-(2-methoxyethoxy)ethoxy)acetic acid, MEEAA, was added to increase the stability of the aqueous dispersions. All the NPs are positively charged after the surface functionalization as confirmed by the ζ -potential measurement (**Table 3.1**). In the end, colloiddally stable suspensions were obtained for all the ferrite NPs, except for MnFe_2O_4 , which continued to have some tendency to agglomerate.

Table 3.1 ζ -potentials for the colloidal NP suspensions.

	Co_3O_4	MnFe_2O_4	Fe_3O_4	CoFe_2O_4	NiFe_2O_4	GO
ζ -potential [mV]	38.7	21.5	40.5	26.0	21.4	-24.8
Conductivity [mS/cm]	0.1151	0.4887	0.2936	0.3966	0.3480	1.0179

During the curing step, the GO sheets start to cross-link and self-assemble into a macroscopic gel. The positive surface charge of the NPs enables intimate binding to the negatively charged GO sheets, resulting in a large number of NPs uniformly incorporated into the interconnected GO network. The obtained wet gels exhibit disordered and open macroporosity which is clearly visible on the SEM image. As a representative example, the morphology of $\text{Co}_3\text{O}_4/\text{rGO}$ composite aerogel is shown in **Figure 3.2c**. The morphology SEM images of all other spinel/rGO composite aerogel and pure rGO aerogel without NPs can be found in Figure D.2 in Appendix. The SEM image at higher magnification (**Figure 3.2d**) shows that the GO sheets are corrugated with abundant NPs embedded between them. The inset TEM image reveals more clearly that

plenty of Co_3O_4 NPs are homogeneously combined on the rGO sheets. The specific surface area and the porosity were characterized by nitrogen adsorption-desorption isotherm measurements for the $\text{Co}_3\text{O}_4/\text{rGO}$ composite aerogel and for the rGO aerogel without nanoparticles (Figure D.3-4). The rGO aerogel possesses remarkably high BET specific surface area of up to $815 \text{ m}^2 \text{ g}^{-1}$. For the $\text{Co}_3\text{O}_4/\text{rGO}$ aerogel the surface area is $332 \text{ m}^2 \text{ g}^{-1}$ due to the large amount of heavy Co_3O_4 nanocrystals. The pore size distribution further demonstrates the existence of some mesoporosity between 3 and 40 nm.

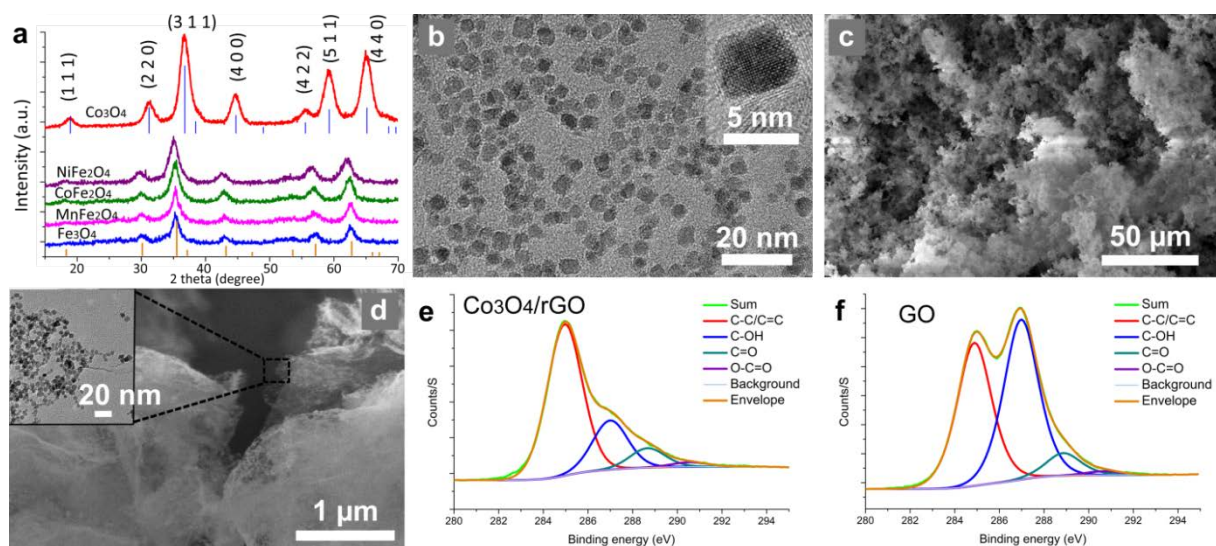


Figure 3.2 **a**, XRD patterns for all the as-prepared spinel-type transition metal oxides. **b**, TEM image of the Co_3O_4 nanocrystals with cube-like morphology and narrow particle size distribution (inset: HRTEM of a Co_3O_4 nanocube). **c**, SEM image of the $\text{Co}_3\text{O}_4/\text{rGO}$ composite aerogel at low magnification, and **d**, at higher magnification (inset: TEM image of the composite aerogel, showing that the Co_3O_4 nanocrystals are homogeneously distributed and intimately anchored on the rGO sheets). **e**, High resolution XPS spectra of C 1s for the $\text{Co}_3\text{O}_4/\text{rGO}$ aerogel and **f**, the pristine GO sample, giving evidence for the partial reduction of the GO in the composite sample.

Interestingly, X-ray photoelectron spectroscopy (XPS) measurements show that the GO is partially reduced even under the mild treatment conditions of $95 \text{ }^\circ\text{C}$. As an example, **Figure 3.2e,f** depict the C 1s XPS high resolution spectra on the composite $\text{Co}_3\text{O}_4/\text{GO}$ sample and the pristine GO sample, respectively. The envelop of the C 1s peak is deconvoluted into four components,¹²⁶ corresponding to C-C/C=C (aromatic rings, 284.9 eV), C-OX (epoxy (X=C) and hydroxyl groups (X=H), 287.0 eV), C=O (288.7 eV) and O-C=O (carboxyl groups, 290.6 eV). Comparing the spectra, we can clearly observe that the signal attributed to the C-OH groups is significantly decreased for the heat treated

sample. This observation indicates that oxygen-containing functional groups on the GO sheets are partially removed upon thermal treatment, which is beneficial for the electronic conductivity.¹²⁷ Other samples display similar results that can be found in Figure D.5 in Appendix.

The use of nanostructured composite aerogels as electrode materials represents a promising avenue to boost the electrochemical performance, as this strategy synergistically strengthens the advantages of each component, but also mitigates their disadvantages.^{51, 128} In our study, we chose spinel-type transition metal oxides as demonstration anodes as they can offer high theoretical capacity via conversion mechanism. However, the general issues associated with conversion-type materials also apply to spinels, such as abrupt structure and volume changes upon Li^+ cycling, and unfavorable e^- and Li^+ conductivity. Consequently, poor cyclability (less than 150 cycles) is a general issue for most of the reported results.¹⁰⁷⁻¹¹¹ On the other hand, graphene or graphene oxide has received broad attentions in energy storage applications due to its high specific surface area and e^- conductivity. It can store Li^+ *via* a double-sided adsorption mechanism forming LiC_3 with a theoretic specific charge of 744 mAh g^{-1} , which is double of the theoretical capacity of 372 mAh g^{-1} for graphite.¹²⁹ Unfortunately, graphene is prone to restacking, leading to drastic fading in its high initial capacities. To address these issues and to exploit high performance electrodes, we designed a rGO-based composite aerogel with embedded spinel-type metal oxide nanoparticles. rGO based aerogels can offer a hierarchical porosity, in which the macropores act as a buffering reservoir for the Li-ion containing electrolyte, facilitating the diffusion to the interior surfaces, while the mesopores provide a large accessible surface area for the Li^+ transport/storage and accommodate any local volume changes upon Li^+ insertion/extraction for conversion-type metal oxides.¹³⁰ The introduction of NPs as spacers/pillars between graphene or rGO interlayers plays a critical role to prevent the hierarchical structure from collapsing. In return, the rGO sheath protects the NPs from detaching from the conducting medium, and its percolating graphitic network provides a conductive pathway for e^- transport for the active NPs. As a result of this design, synergistic effects are expected to lead to high capacity and long-term cycling stability of the electrode.

To demonstrate the benefits of the composite electrode with the hierarchical microstructure, the $\text{Co}_3\text{O}_4/\text{rGO}$ and $\text{CoFe}_2\text{O}_4/\text{rGO}$ aerogel films are discussed as examples in more details. Data from the other composites (MnFe_2O_4 , Fe_3O_4 , and NiFe_2O_4) are reported in Figure D.6-9 in Appendix. A constant voltage (CV, potentiostatic) step after the constant current mode (CC, galvanostatic) helps to complete discharge/charge, particularly at high current rate. In order to study the kinetic behaviors of Li^+ insertion/removal into/from the composite electrodes at different current rates, a CV step might be added after the CC mode on discharge or charge. 1C^* is defined as 1 A g^{-1} through the whole text (* is added if a constant voltage step was applied where the cut-off current was set typically to 0.05C or higher). To easily compare with the results obtained in other publications, battery performance only under galvanostatic mode is always shown in the figures of composite electrodes.

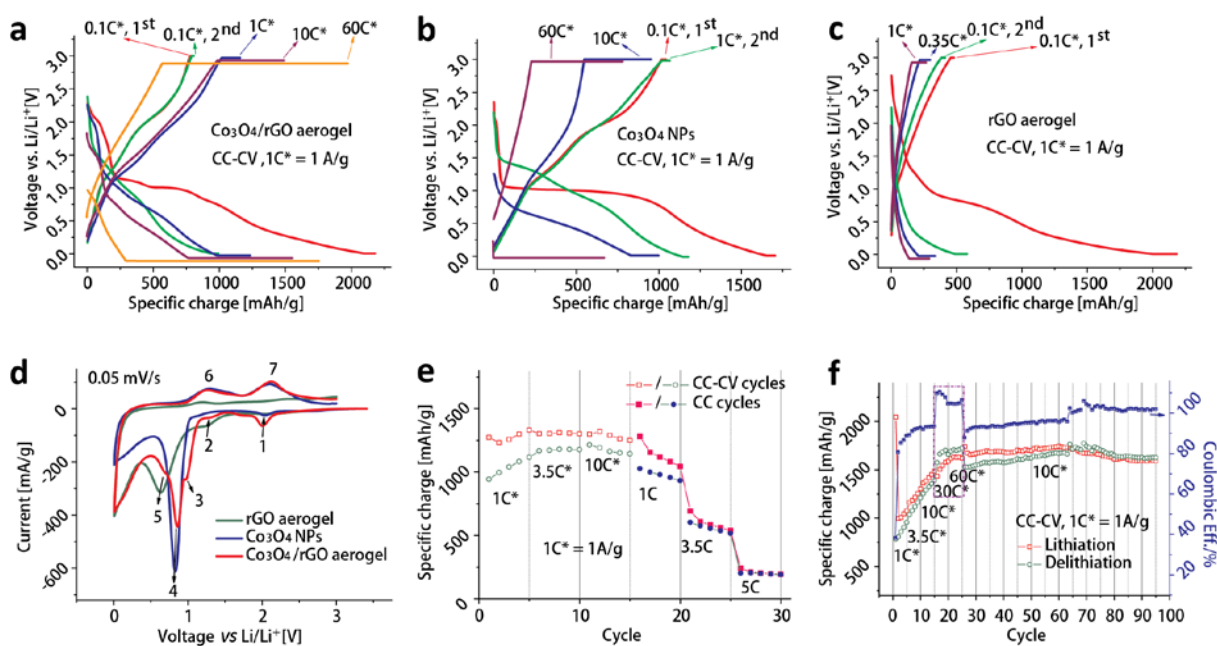


Figure 3.3 Constant current + constant voltage (CC+CV) cycling profiles for **a**, the $\text{Co}_3\text{O}_4/\text{rGO}$ composite aerogel, **b**, the as-obtained Co_3O_4 NPs with 30% of carbon black and 10% of binder and **c**, the rGO aerogel without any NPs. **d**, Comparison of the cyclic voltammetry scans for all three samples. **e**, Comparison between CC+CV cycles and CC cycles for $\text{Co}_3\text{O}_4/\text{rGO}$ composite aerogel. **f**, Cycle performance of the $\text{Co}_3\text{O}_4/\text{rGO}$ composite aerogel under CC+CV conditions.

The results of the CC+CV cycling profiles for the $\text{Co}_3\text{O}_4/\text{rGO}$ composite aerogel are presented in **Figure 3.3a**. On the initial discharge at 0.1 C^* , the $\text{Co}_3\text{O}_4/\text{rGO}$ composite aerogel displays a short plateau at 2.0 V , which could be assigned to the formation of

$\text{Li}_x\text{Co}_3\text{O}_4$.¹³¹ Another plateau at ~ 1.2 V comes from the contribution of rGO, as deduced from a comparison of the cyclic voltammetry measurements between all three samples (**Figure 3.3d**). Another long plateau at ~ 1.0 V results from the conversion reaction of $\text{Li}_x\text{Co}_3\text{O}_4$ to metallic Co embedded in Li_2O .^{131, 132} Finally, a sloping curve down to the cut-off voltage of 0.01 V develops, which is mainly associated with three processes occurring in parallel: the solid electrolyte interphase (SEI) formation, the reduction of functional groups bound to the graphene oxide layers, and the double side adsorption of Li^+ on the graphene oxide layers.^{129, 133, 134} In total, 2184 mAh g^{-1} are delivered. Two oxidation peaks at 1.3 V and 2.1 V on the first charge arise from Li^+ extraction, transforming the material back to $\text{Co}_3\text{O}_4/\text{CoO}$ and graphene layers.^{132, 133, 135} A capacity of 792 mAh g^{-1} is covered (**Figure 3.3a**, 1st charge), corresponding to an initial Coulombic efficiency of 36.3%. The low Coulombic efficiency is mainly due to the high surface area, which comes along with the irreversible formation of SEI as well as with the irreversible reaction with functional groups on graphene oxide layers.¹³³ The issue of a low initial efficiency can be improved by a prelithiation procedure.¹¹² After several cycles at 0.1 C^* , the composite aerogel seems to be activated, it presents better EC behavior upon each cycle (**Figure 3.3a,f**). The total capacity delivered at 1 C^* is higher than that obtained at 0.1 C^* while the potential hysteresis between charge and discharge is also decreased. Even at 10 C^* , the composite $\text{Co}_3\text{O}_4/\text{rGO}$ aerogel can charge the same capacity on the CC part as the curve at 1 C^* . In total, the capacity delivered at 10 C^* is 1494 mAh g^{-1} , with 503 mAh g^{-1} contribution from the CV part. At 60 C^* , the total capacity further increases to 1963 mAh g^{-1} , but the largest contribution comes from the CV part, namely 1385 mAh g^{-1} . As the current increases to such high rates, the different kinetics in the lithiation and delithiation can be clearly observed: the lithiation process is more sluggish than that of the delithiation, which is also confirmed by the asymmetric cycling tests shown in Figure D.10 in Appendix. Nevertheless, even without the help of the CC part, the $\text{Co}_3\text{O}_4/\text{rGO}$ composite aerogel demonstrate its high rate capability as shown in Figure 2e. It can deliver about 1005 mAh g^{-1} at 1 C, 580 mAh g^{-1} at 3.5 C and 205 mAh g^{-1} at 5 C rate.

An interesting phenomenon is observed for the rate-capability plot: when the current increases from 10 C^* to 30/60 C^* , the Coulombic efficiency reaches more than 100%, as shown in the purple box in **Figure 3.3f**. It seems that the Li^+ ions, trapped in the porous

electrode during previous cycles, are suddenly released. The same observation could be made on other composite aerogel samples (see Figure D.6-8), but never on the conventionally prepared NP or pure rGO samples (**Figure 3.3b,c**). Accordingly, it seems that this unusual kinetics behavior is related to the influence of the hierarchical, porous microstructure on the lithium deposition in the composite aerogels at very high current rates.

For comparison, conventionally prepared electrodes were fabricated from as-obtained Co_3O_4 NPs using 30 wt% of carbon black and 10 wt% of binder (PVDF). Shown in Figure 2b, on the first discharge at 0.1 C^* a short potential plateau at 2.0 V is followed by a long plateau at $\sim 1.0\text{ V}$ and a sloping curve down to the cutoff voltage. Overall, 1702 mAh g^{-1} can be delivered. On delithiation at 0.1 C^* , two short plateaus appear at $\sim 1.2\text{ V}$ and $\sim 2.1\text{ V}$, respectively, with a total specific charge of 1044 mAh g^{-1} , giving an initial Coulombic efficiency of 61.3%. On the second discharge at 1 C^* , the plateau at 1.0 V disappears at the expense of a slope with blurred plateaus extracting a total specific charge of 1180 mAh g^{-1} . In the second cycle, the Coulombic efficiency is enhanced to 90.7%. However, at a rate of 10 C^* the hysteresis between charge and discharge is much larger than that of the 1 C^* curve, and it is even more pronounced for high rates at 60 C^* , where Co_3O_4 NPs show significant over-potentials, leading to a premature hitting of the cut-off potential upon discharge.

As a second reference, the pure rGO aerogel without any embedded NPs was also tested under the same conditions (**Figure 3.3c**). The initial discharge capacity of 2186 mAh g^{-1} at 0.1 C^* is remarkably high. However, the first delithiation capacity at 0.1 C^* is only 481 mAh g^{-1} , which gives an initial Coulombic efficiency of only 22.0%. After the 1st cycle at 0.1 C^* , the total capacities continue dropping upon every cycle. After five cycles at 1 C^* , it can merely deliver a capacity of 294 mAh g^{-1} on discharge and 269 mAh g^{-1} on charge. These specific charges are close to those of graphite electrodes, indicating restacking of the rGO sheets to a graphite-like structure.¹³⁶ The significantly lower electrochemical performances of these two reference samples clearly emphasize the importance of a rational design of the microstructure of the composite electrode.

To acquire more insight into the exceptional EC behavior of the rGO-based composite aerogels, electrochemical impedance spectroscopy (EIS) measurements at an amplitude

of 10 mV over the frequency range from 100 kHz to 0.01 Hz were carried out on the pristine electrodes as well as on the ones that went through different cycles. In **Figure 3.4**, we show the $\text{Co}_3\text{O}_4/\text{rGO}$ aerogel as a representative example of all the other samples that display similar results (see Figure D.6-9). The pristine electrode does not undergo any charge-transfer reactions and only diffusional processes (Warburg impedance part) take place. However, after three cycles at 0.1 C the response of the electrode changes significantly and a semicircle can be observed, indicating a proper charge transfer reaction. Thus, the composite electrodes become activated as already observed in the total extracted specific charge in **Figure 3.3f** and in **Figure 3.6**.

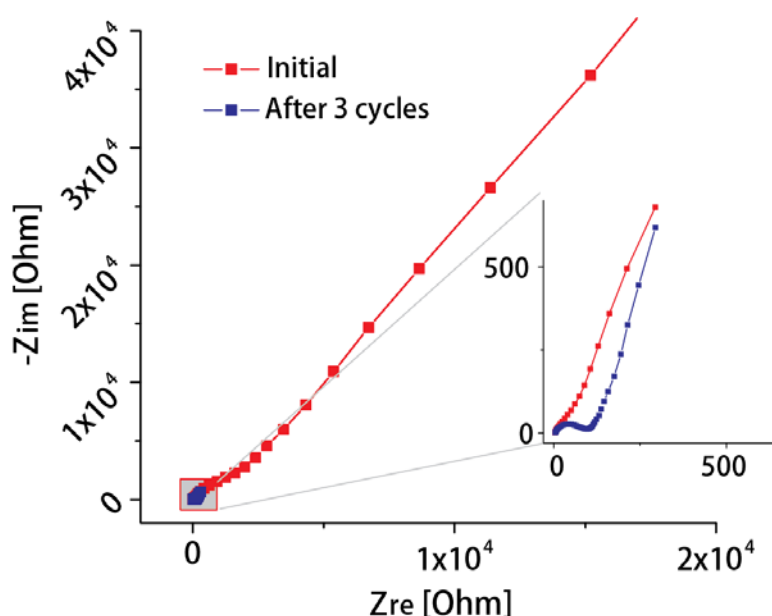


Figure 3.4 EIS spectra of the $\text{Co}_3\text{O}_4/\text{rGO}$ composite aerogel before and after 3 cycles at 3 V vs. Li^+/Li .

To underline the general applicability and benefit of our electrode design with its hierarchical porous microstructure, we discuss, as another sample, the $\text{CoFe}_2\text{O}_4/\text{rGO}$ composite fabricated by the same protocol. **Figure 3.5** presents the results of CC+CV cycling profiles. On the initial cycle at 0.1 C^* , the $\text{CoFe}_2\text{O}_4/\text{rGO}$ aerogel delivers capacities of 2045 mAh g^{-1} on lithiation and 904 mAh g^{-1} on delithiation, corresponding to a Coulombic efficiency of 44.2%. On the second cycle at 0.1 C^* , a rapid improvement to 80.6% occurs as a results of 1045 mAh g^{-1} on lithiation and 842 mAh g^{-1} on delithiation. Similar to the results of the $\text{Co}_3\text{O}_4/\text{rGO}$ composite, capacities are accumulated over cycles. For instance, 929, 1177 and 1290 mAh g^{-1} are discharged at current rates of 1, 10 and 60 C^* , respectively. To demonstrate the long-term stability,

the $\text{CoFe}_2\text{O}_4/\text{rGO}$ composite aerogel was galvanostatically cycled without the help of the constant voltage part, and it manifests a remarkable rate capability and long-lived cycle performance. As shown in **Figure 3.6**, at 1 A g^{-1} , it goes through a capacity fading down to 360 mAh g^{-1} in the first 30 cycles. In the following 170 cycles, the composite electrode is activated and the capacity gradually increases back to 700 mAh g^{-1} . The average Coulombic efficiency for the first 200 cycles at 1 A g^{-1} is 96.2%. For the next 200 cycles the current rate is increased to 2 A g^{-1} . Nevertheless, the electrode still delivers a very stable capacity of around 520 mAh g^{-1} with an average efficiency of 99.6%. To test the limit of the electrode, the current rate was further promoted to 4.5 A g^{-1} for another 1000 cycles with the result that the $\text{CoFe}_2\text{O}_4/\text{rGO}$ composite aerogel still gives an impressive capacity of around 330 mAh g^{-1} , approaching the theoretic limit of graphite (372 mAh g^{-1}). The average Coulombic efficiency on these 1000 cycles is close to 100%.

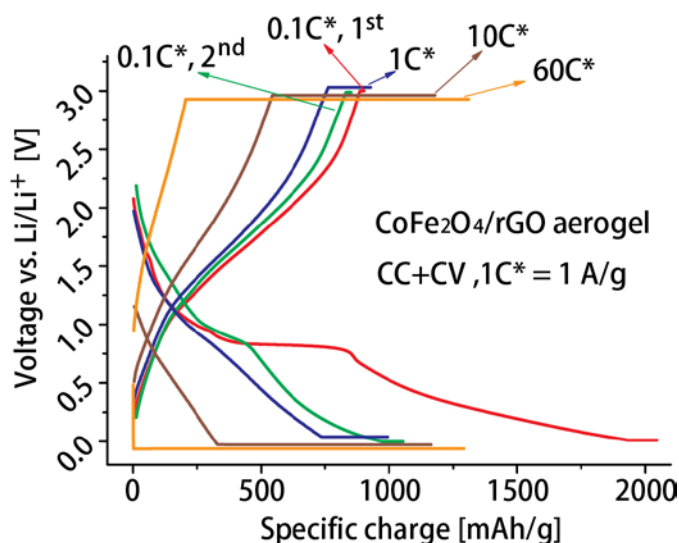


Figure 3.5 CC+CV cycling profiles for the $\text{CoFe}_2\text{O}_4/\text{rGO}$ composite aerogel at different current rates.

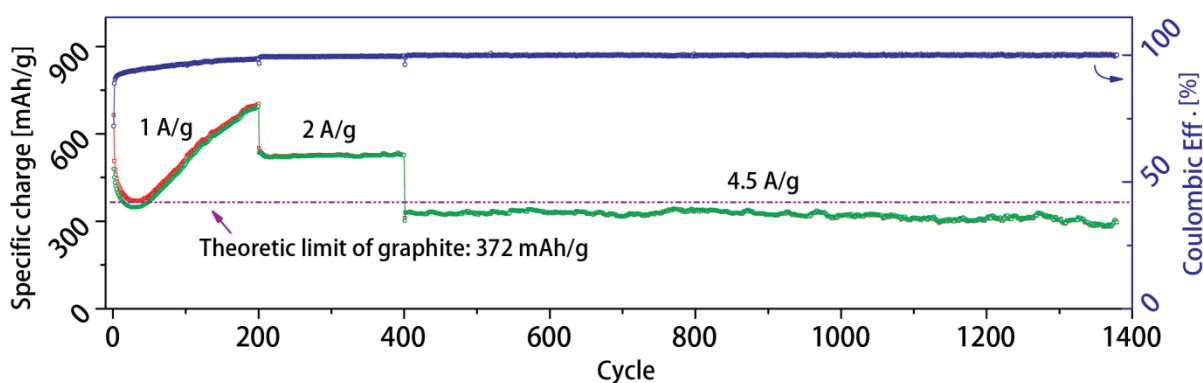


Figure 3.6 Rate capability and long-term stability performance for the $\text{CoFe}_2\text{O}_4/\text{rGO}$ composite aerogel under galvanostatic condition without the help of a constant voltage part.

3.3 Conclusion

In summary, using colloidally stable spinel-type NPs and GO as building blocks with their tailored surface charges, we developed a facile method to fabricate flexible composite spinel-type metal oxide/rGO aerogels with any desired shape that can directly be used as binder-free anodes in LIBs. Benefitting from several structural features provided by this carefully designed electrode architecture, including hierarchical porosity, conductive network and mechanical stability offered by the interpenetrated rGO layers, and the pillar effect of NPs in between the rGO sheets, the hybrid system synergistically enhances the intrinsic properties of each component. Consequently, the spinel/rGO composite aerogel demonstrates much enhanced rate capability and long-term stability without obvious capacity fading after 1000 cycles at high rates. We believe that the strategy presented here can be extended to other metal oxides, sulphides, and alloys (*e.g.* Ge or Sn) for the preparation of advanced anodes in LIBs. In addition, the hierarchically porous microstructure in such hybrids is promising for other applications *e.g.*, in supercapacitors or in catalysis.

3.4 Experimental section

Chemicals: Co(II) acetate (99.995%), Fe(III) acetylacetonate (99.9%), Co(II) acetylacetonate (97%), Ni(II) acetate tetrahydrate (99.998%), Mn(II) acetate (98%), benzyl alcohol (BnOH, 99.8%), ethylenediamine (EDA, 99%), aqueous ammonia solution (~25%) and 2-[2-(2-methoxyethoxy)ethoxy]acetic acid (MEEAA, 99 %) were purchased from Sigma-Aldrich and used as received without further purification. Graphene oxide (2.5-10 mg/ml in H₂O, GO) was purchased from Royal Elite (Shanghai).

Oil bath synthesis of Co₃O₄ NPs: 1 mmol Co(II) acetate was dissolved into 7 ml BnOH under stirring. After several minutes, 7 ml ammonia solution was added into the open vessel. The reddish emulsion was put into an oil bath set at 165 °C, upon which it started to boil immediately with substantial bubble evolution. After ~5 minutes, a reddish solution with significantly reduced volume was obtained, which was kept at 165 °C for 2 h under stirring, leading to a black suspension. The black precipitate was harvested by adding diethyl ether before centrifugation, washed twice with ethanol, and finally dried in an oven at 60 °C. The dry powder was dispersed into H₂O with different concentrations from 10 mg/ml to 30 mg/ml simply by shaking and sonication (1 minute), which turned out to produce colloidal solutions stable for several weeks.

Microwave-assisted synthesis of MFe_2O_4 : For the synthesis of Fe_3O_4 , 1 mmol of Fe(III) acetylacetonate and 100 μ l EDA were added into 5 ml of benzyl alcohol in a 10 ml microwave glass tube in an Ar filled glovebox and stirred for 20 min. The reaction mixture was heated under microwave irradiation at 195 °C for 10 min. The resulting product was washed with diethyl ether once and with a 1:1 mixture of ethanol and diethyl ether for another three times. The obtained wet precipitate was then dispersed in H_2O containing MEEAA (10 μ l/ml). The mixture (20-30 mg/ml NPs) was sonicated for 1 h, resulting in a colloiddally stable dispersion. For the synthesis of the other spinels MFe_2O_4 (M = Co, Mn, Ni), 0.5 mmol Fe(III) acetylacetonate with 0.25 mmol of Mn(II) acetate, Co(II) acetylacetonate or Ni(II) acetate tetrahydrate, respectively, were dissolved in 5 ml of benzyl alcohol with addition of 100 μ l of EDA. All other experimental conditions were the same as for the Fe_3O_4 synthesis.

Fabrication of spinel/rGO composite aerogel: The GO (5 mg/ml, typically) and the NP dispersion (20 mg/ml, typically) were homogenously mixed under sonication (5-10 minutes). The weight percent of NPs was typically kept at 70 %. However, other NP loadings (up to 90 wt%) could be produced by varying the relative concentrations of NPs and GO (see Figure D.11 in Appendix). The mixed suspension was transferred onto a petri-dish like current collector (made of Cu, Ti or Al) or another container, sealed in a closed bottle, and cured under a saturated H_2O vapor environment at 95 °C for 6 h. A monolithic gel film formed without obvious volume shrinkage. The gel was carefully put into an excess of acetone for solvent exchange twice (24 h), followed by drying in supercritical CO_2 . A monolithic, crack-free aerogel film with minimum thickness of ~ 100 μ m was finally obtained. A free-standing film with some extent of volume shrinkage could also be produced if other containers were used (*e.g.*, Teflon).

Electrode preparation: The as-obtained composite aerogel film on a Ti current collector was additionally vacuum dried at 100 °C and later on directly used as electrode without any additives. To investigate the annealing effect on graphene oxide, the composite aerogel was either heated to 250 °C or to 280 °C in N_2 plus 5 vol% H_2 for 6 h with a ramping rate of 2 °C/min (Figure D,12-13). For comparison, Co_3O_4 electrodes were prepared in a conventional way, *i.e.*, 60 wt% of Co_3O_4 was uniformly mixed with 30 wt% of carbon black (Super P, TIMCAL), 10 wt% of PVDF (polyvinylidene fluoride, Aldrich) in NMP (N-methyl-2-pyrrolidinone, Fluka) under mechanical stirring. The resulting paste was transferred onto a Ti current collector and vacuum dried at 100 °C overnight. The average electrode loading was 1-1.5 mg/cm². Higher loadings could also be achieved using larger concentrations of GO and NP suspensions.

Electrochemical Measurements: Electrodes were assembled into Swagelok-type cells in an Ar filled glove box (H_2O , O_2 < 0.1 ppm). Li metal (99.9%, Alfa-Aesar) served as both reference and counter electrode. A glass fiber separator was soaked with electrolyte (1 M $LiPF_6$ in 1:1 wt% ethylene carbonate (EC)/dimethyl carbonate (DMC), Novolyte). All electrochemical measurements were performed using a Biologic instrument (VMP3) at room temperature. The electrodes were cycled between 0.01 and 3 V vs. Li/Li^+ for varying specific current rates. 1 C was defined as 1 A g⁻¹. If a constant voltage step was added, the cut-off current was set at 0.05 A g⁻¹.

Characterizations: X-ray powder diffraction (XRD) patterns were recorded using a PANalytical diffractometer (Empyrean with monochromator, Cu K α radiation). The morphologies were studied by a LEO 1530 Gemini scanning electron microscope (SEM) working at 5kV and by a Philips CM 12 transmission electron microscope (TEM) at 100 kV. The ζ -potential information was obtained on Zeta Potential Analyzer (DelsaNano C, Beckman Coulter). X-ray photoelectron spectra (XPS) were recorded on a Sigma 2 spectrometer (Thermo scientific) using a non-monochromatic Al K α X-ray source, where binding energy was calibrated taking C 1s = 285.0 eV. N₂ adsorption/desorption isotherms were measured on a Quantachrome Autosorb-iQ to acquire the specific surface area and pore size distribution by the BET and DFT method, respectively. The carbon contents were determined by thermogravimetric analysis (TGA, Q500, TA Instruments).

Chapter 4 Hierarchical Graphene-Based Aerogels as Anodes

4.1 Introduction

Lithium ion batteries revolutionized the market for mobile devices after Sony successfully commercialized the first $\text{Li}_{1-x}\text{CoO}_2/\text{C}$ cell in 1991.¹³⁷ Until today, carbon-type materials, *e.g.* natural graphite or hard/soft carbons, have dominated in battery anodes. In spite of all the success, for applications in electric vehicles the energy density, rate performance and lifespan need to be significantly improved. Carbon, in the form of graphite, which theoretically discharges 372 mAh g^{-1} by forming LiC_6 ,⁴⁵ has almost reached its limit. Graphene, on the other hand, arouse tremendous research interest because it often presents much higher specific capacities. It was proposed that double-side adsorption of Li-ion on a single graphene sheet gives a theoretical capacity of 744 mAh g^{-1} for LiC_3 .^{46, 138} Sato et al. suggested a different mechanism for disordered carbons. Each Li-ion is trapped in one benzene ring, and a capacity of 1116 mAh g^{-1} with the end product of LiC_2 was predicted.¹³⁹ Another model based on organic electrodes (composed of fused C6 aromatic rings) even indicated that each C6 ring can reversibly accept 6 Li-ion to form a LiC complex, offering 2233 mAh g^{-1} .¹⁴⁰ Although many researchers tried to maximize the capacity of graphene by expanding its interlayer spacing¹³⁶ or by introducing a large quantity of structural defects,^{141, 142} most of the attempts are far from being satisfactory, with the long-term cyclability at high current rates representing the key issue.¹²⁹

4.2 Results and discussion

Graphene is thermodynamically prone to restacking, which means that without

The content of this chapter was submitted with authorship G. Zeng, A. Sologubenko, Y. Gong, E. T-Gorokhova, X. Chen, A. Lauria and M. Niederberger*.

appropriate electrode design the high capacity drops quickly upon extended cycling.^{143, 144} Here we present a simple and potentially scalable methodology to fabricate graphene-based aerogels with a complex architectural design (**Figure 4.1**). Three categories of particles with different size ranges are homogeneously incorporated between disordered and crumpled graphene sheets, acting as multiscale spacers: i) Mo_xS_y /amorphous carbon composite spheres of 50-200 nm in diameter; ii) Mo_xS_y nanoparticles around 5-6 nm and iii) sub-nanometer Mo_xS_y molecular clusters. These spacers not only ensure a hierarchical porosity, which facilitates the Li-ion transport/storage, but they also play a critical role as pillars on different length scales preventing the collapse of the porous graphene structure. The self-assembled graphene sheets are connected by π - π interactions, resulting in macro-porosity that acts as a buffering reservoir for the Li-ion electrolyte, while the percolating graphitic network provides the conductive pathway for the electrons. Upon lithiation, the graphene and the spacers can uptake Li-ions and thus both components contribute to the high capacity. Moreover, the initially corrugated graphene sheets do not only accommodate the resulting volume increase of the spacers, but also act as protective shells to prevent their detachment from the aerogel framework.¹⁴⁵ By combining structural units of different size scales, the architecture of the composite aerogel is able to synergistically strengthen the individual beneficial contributions of each component,⁵¹ such that an enhanced electrochemical (EC) performance can be expected.

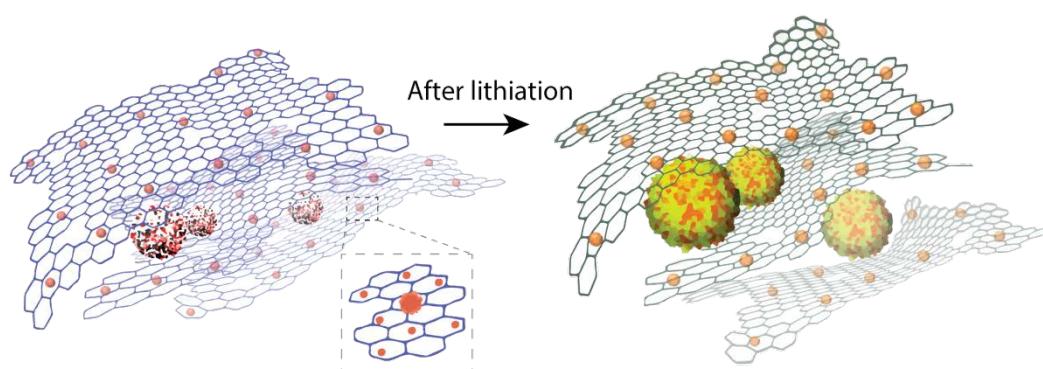


Figure 4.1 Schematic of the graphene-based aerogel anode before and after Li-ion insertion (the different building blocks are not in scale). Three categories of spacers are homogeneously incorporated between disordered graphene sheets: i) Mo_xS_y /amorphous carbon composite spheres with diameters of 50-200 nm; ii) Mo_xS_y nanoparticles around 5-6 nm and iii) sub-nanometer sized Mo_xS_y clusters. Different size ranges of the spacers ensure a hierarchical porosity of the aerogel, which along with the conductive network and the mechanical stability provided by graphene results in a composite with greatly enhanced rate capability and ultra-long stability (up to 10,000 cycles).

The construction of porous graphene-based aerogels generally requires expensive templates, *e.g.* a Ni foam,¹⁴⁶ and sophisticated techniques, *e.g.* chemical vapor deposition (CVD),¹⁰³ which makes the scalability impractical for large-scale battery production. In our approach we directly start from commercially available graphene oxide (GO) dispersions and MoS₂ powder to fabricate the hierarchical porous electrode (see Methods). After ball milling in N-methyl-2-pyrrolidone (NMP), the initially crystalline and micron-sized MoS₂ particles (**Figure 4.2**) were transformed into sub-nanometer molecular clusters, which were amorphous (**Figure 4.2a & 4.3a**). Some of the dots were well dispersed, while others loosely aggregated into nano assemblies with sizes of around 5-6 nm. Owing to the high-energy ball milling process, the initial MoS₂ was oxidized to Mo(V) and S(VI+) (**Figure 4.4**). In the following, for simplicity the oxidized species are referred to as Mo_xS_y. In addition, NMP molecules attached to the Mo_xS_y surface during ball milling (**Figure 4.5**), which enabled the aqueous Mo_xS_y dispersion to be colloidally stable for months (**Figure 4.3a inset**). In the next step of the electrode fabrication process, the Mo_xS_y dispersion was combined with dopamine to form Mo_xS_y/polydopamine (PDA) spheres with sizes of 50-200 nm after polymerization (Fig. 2b). The Mo_xS_y/PDA dispersion (**Figure 4.3b inset**) was mixed with the GO dispersion. Upon a curing step at 95 °C, the GO sheets started to cross-link and self-assembled into a monolithic composite Mo_xS_y/PDA/GO hydrogel. After critical point drying, the obtained composite aerogel was thermally treated. The annealing process converted the graphene oxide into reduced graphene oxide (rGO) and the PDA beads into amorphous carbon, where the nitrogen from PDA was expected to be incorporated as a dopant into the graphene lattice,^{147, 148} finally leading to a conductive Mo_xS_y/C/rGO aerogel consisting of the three components Mo_xS_y, Mo_xS_y/N-doped carbon hybrid spheres and N-doped rGO (**Figure 4.3c inset**).

The composite Mo_xS_y/C/rGO aerogel was macroporous (**Figure 4.3c**), and SEM/TEM images at higher magnifications (**Figure 4.3d,e**) revealed that the rGO sheets were highly corrugated with embedded Mo_xS_y/amorphous carbon microspheres. The 3D tomography TEM/STEM images and the EDX line scan over the sphere clearly confirmed that it was a hybrid of homogeneously distributed sub-nanometer Mo_xS_y dots and N-containing amorphous carbon, rather than a core-shell structure (**Figure 4.3f**). The three types of spacers on three different length scales as proposed in **Figure 4.1** are

experimentally illustrated in **Figure 4.3g-i**. Besides the $\text{Mo}_x\text{S}_y/\text{C}$ spheres as micro spacers, we also found Mo_xS_y nano assemblies of 5-6 nm embedded between the graphene sheets, and, surrounding these Mo_xS_y nano assemblies, a large number of sub-nanometer Mo_xS_y clusters homogeneously distributed over the graphene layers. All together the spacers and the graphene provide a large surface area of $369 \text{ m}^2 \text{ g}^{-1}$ with a multiscale porosity spanning from the meso to the macro range (**Figure 4.6**). Moreover, N-doping and defects are critical to promote the capacity of graphene.¹⁴⁹ The NMP molecules attached to the Mo_xS_y particles and the PDA-hybrid spheres both acted as nitrogen source during their decomposition upon annealing, leading to N-doped graphene (**Figure 4.7**).

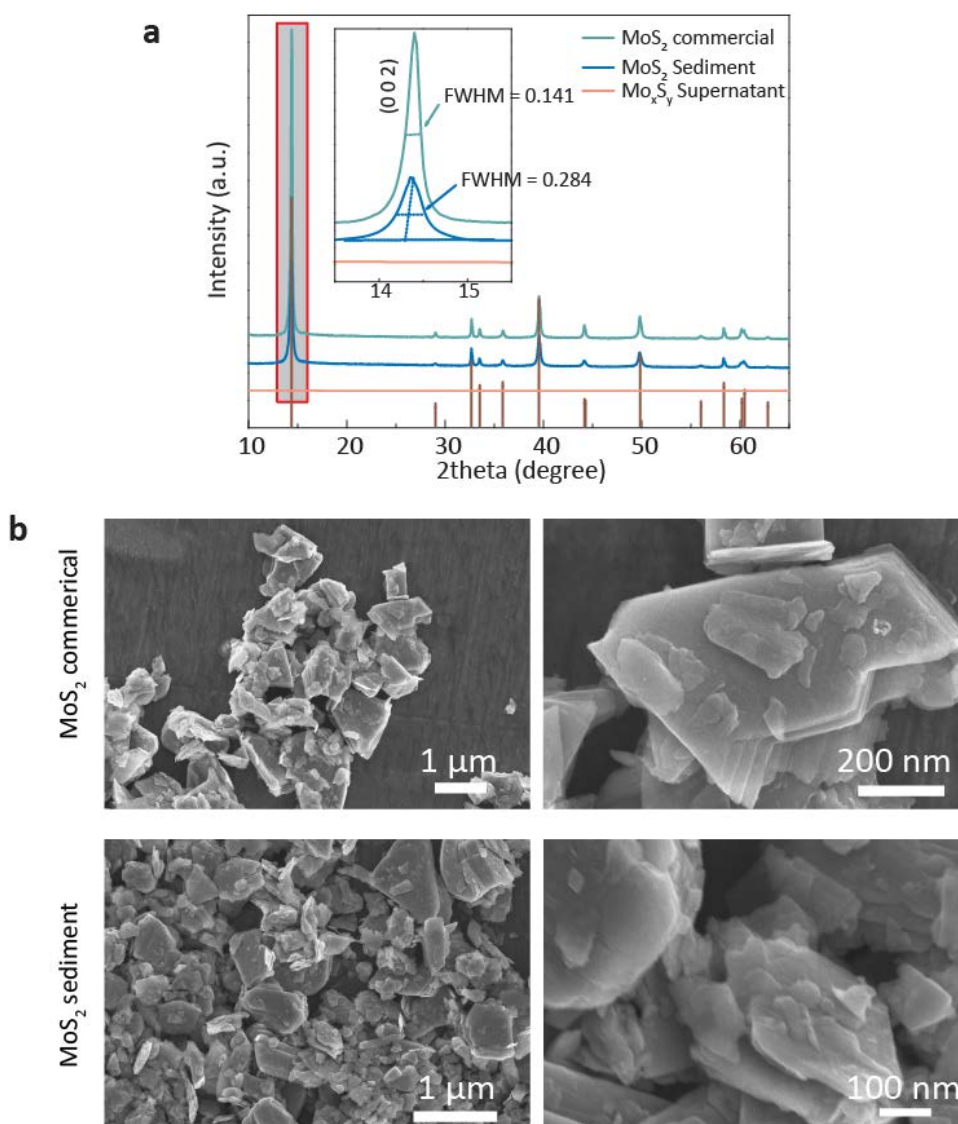


Figure 4.2 XRD patterns and SEM images of the different Mo_xS_y compounds used for the preparation of the dispersion. The Mo_xS_y particles were prepared via ball milling of commercial

MoS₂ and separated via centrifugation. Only the Mo_xS_y supernatant was collected for further processing. **a**, XRD patterns of the commercial MoS₂, MoS₂ sediment and Mo_xS_y supernatant, respectively. **b**, SEM images of the commercial MoS₂ and MoS₂ sediment, respectively. From XRD and SEM image analysis, we can conclude that the commercial MoS₂ was well crystalline with particle sizes around 1-2 μm; the sediment after centrifugation had a slightly decreased crystallinity (increased full width at half maximum, FWHM) and particle size. The Mo_xS_y particles in the supernatant were completely amorphous.

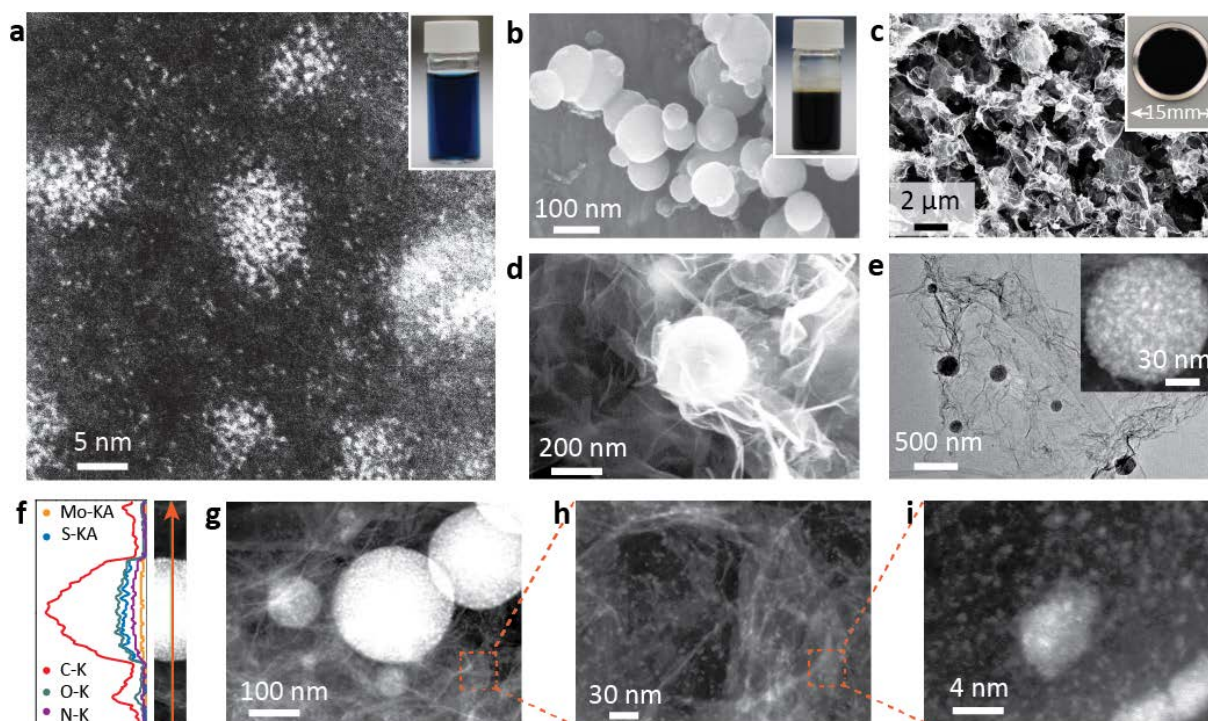


Figure 4.3 Morphology of the graphene-based composite aerogel at different stages of the fabrication process. **a**, STEM image of sub-nanometer sized Mo_xS_y clusters, which are individually dispersed, but sometimes also form nano assemblies of 5-6 nm. Inset, colloidally stable aqueous Mo_xS_y dispersion. **b**, SEM image of Mo_xS_y/polydopamine (PDA) spheres. Inset, stable aqueous Mo_xS_y/PDA dispersion. **c-e**, SEM and TEM images of the annealed Mo_xS_y/PDA/GO composite aerogel at different magnifications. Inset-c, photograph of an annealed aerogel sample on a current collector. The STEM image (inset-e) and EDX line scan (Fig. **f**) confirms that the annealed Mo_xS_y/PDA spheres consist of Mo_xS_y and N-doped amorphous carbon. **g-i**, STEM images of the annealed Mo_xS_y/PDA/GO composite revealing the three categories of spacers, which are **g**) Mo_xS_y/amorphous carbon composite spheres of 50-200 nm in diameter; **h**) Mo_xS_y nanoparticles around 5-6 nm and **i**) sub-nanometer Mo_xS_y molecular clusters, respectively.

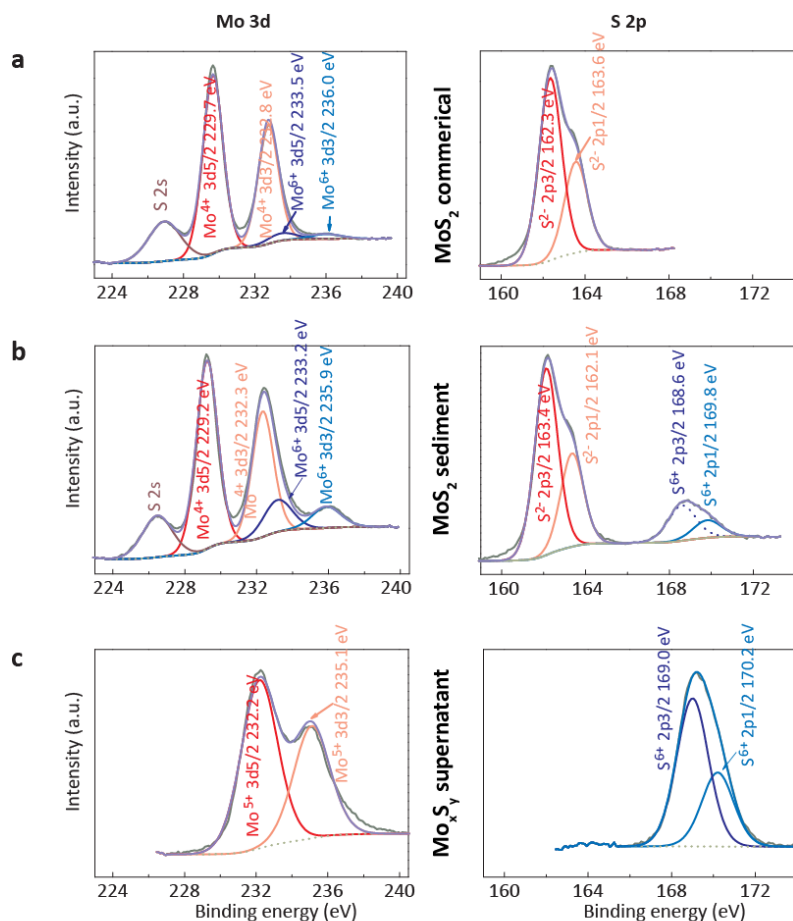


Figure 4.4 High-resolution XPS spectra of Mo 3d and S 2p recorded for commercial MoS₂, MoS₂ sediment and Mo_xS_y supernatant, respectively. After deconvolution of the Mo 3d and S 2p peaks, we can conclude that commercial MoS₂ is predominantly composed of Mo(IV+) and S(II-) with a tiny amount of Mo(VI+). The MoS₂ sediment was rather similar, however with an additional small quantity of S(VI+). The Mo_xS_y in the supernatant was oxidized to Mo(V+) and S(VI+). The higher oxidation states are ascribed to the high energy ball milling process.

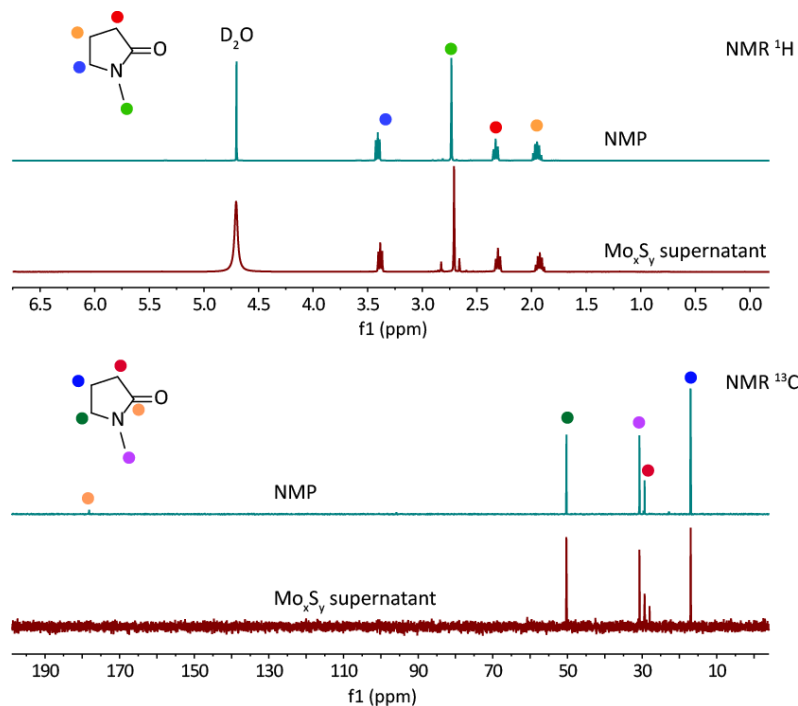


Figure 4.5 Comparison of ¹H/¹³C NMR spectra of N-methyl-2-pyrrolidone (NMP) and the Mo_xS_y supernatant in D₂O. The similarity of the NMR spectra of NMP and the Mo_xS_y supernatant demonstrates that NMP molecules were attached to the Mo_xS_y particle surface.

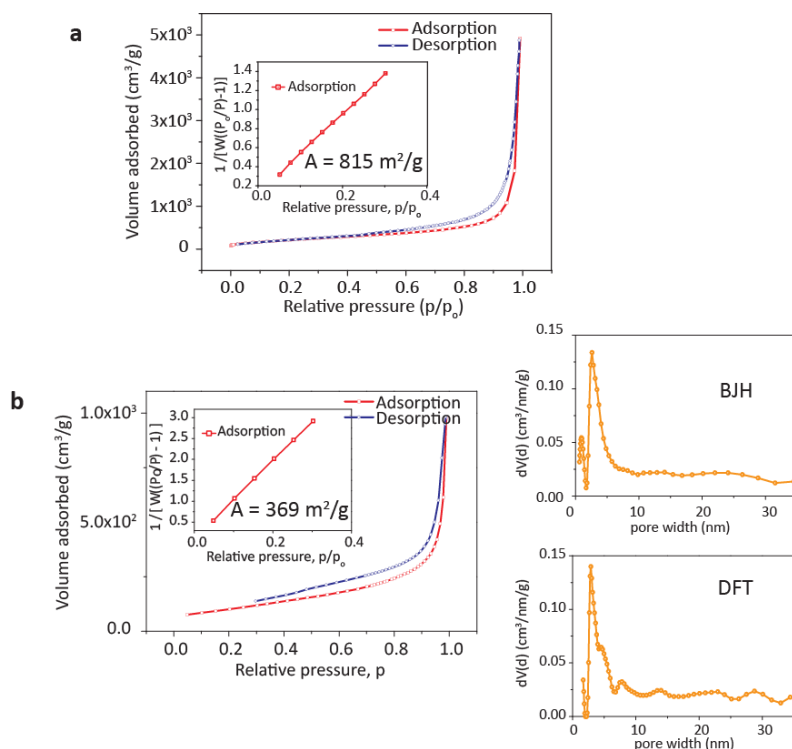


Figure 4.6 Specific surface area and pore size distribution. **a**, N_2 adsorption/desorption isotherm for a rGO aerogel with a high specific surface area of $815 \text{ m}^2/\text{g}$. **b**, Isotherm curves for the $\text{Mo}_x\text{S}_y/\text{C}/\text{rGO}$ composite aerogel with surface area of $369 \text{ m}^2/\text{g}$. The pore size distribution of the composite aerogel was calculated by BJH and DFT method, both of which gave a sharp peak at around 4 nm and a continuous tail up to 40 nm. The large number of mesopores between 3-40 nm, together with the macropores ($> 50 \text{ nm}$) visible in the SEM image indicate a hierarchical porosity for the $\text{Mo}_x\text{S}_y/\text{C}/\text{rGO}$ aerogels. The macropores act as a buffering reservoir for the Li-electrolyte, facilitating Li-ion diffusion to the interior surfaces, while the mesopores offer a large surface area accessible for Li-ion transport/storage, able to accommodate any local volume changes upon Li^+ insertion/extraction for the $\text{Mo}_x\text{S}_y/\text{C}$ spheres.

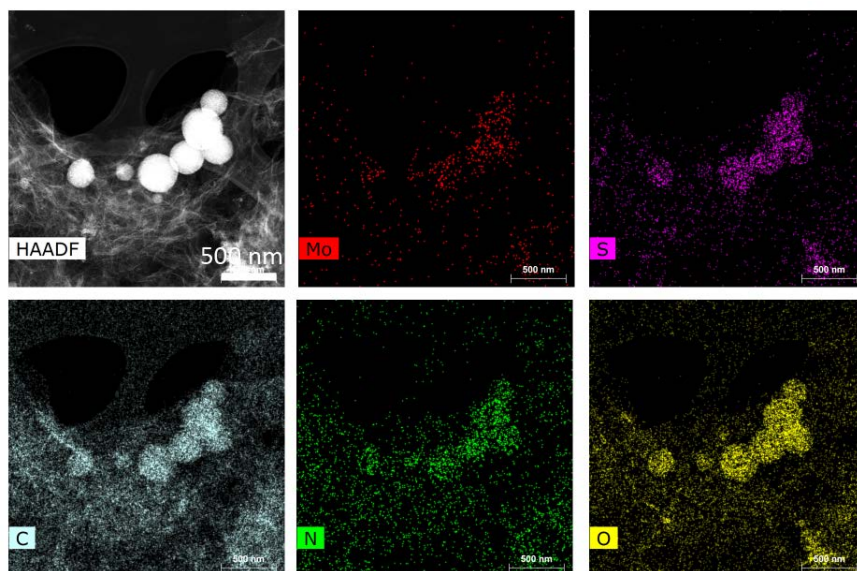


Figure 4.7 EDX mapping of the $\text{Mo}_x\text{S}_y/\text{C}/\text{rGO}$ composite aerogel. The Mo_xS_y particles with different size scales are homogeneously distributed on the graphene layers. Nitrogen from the pyrolysis of PDA and NMP is uniformly incorporated in the graphene sheets.

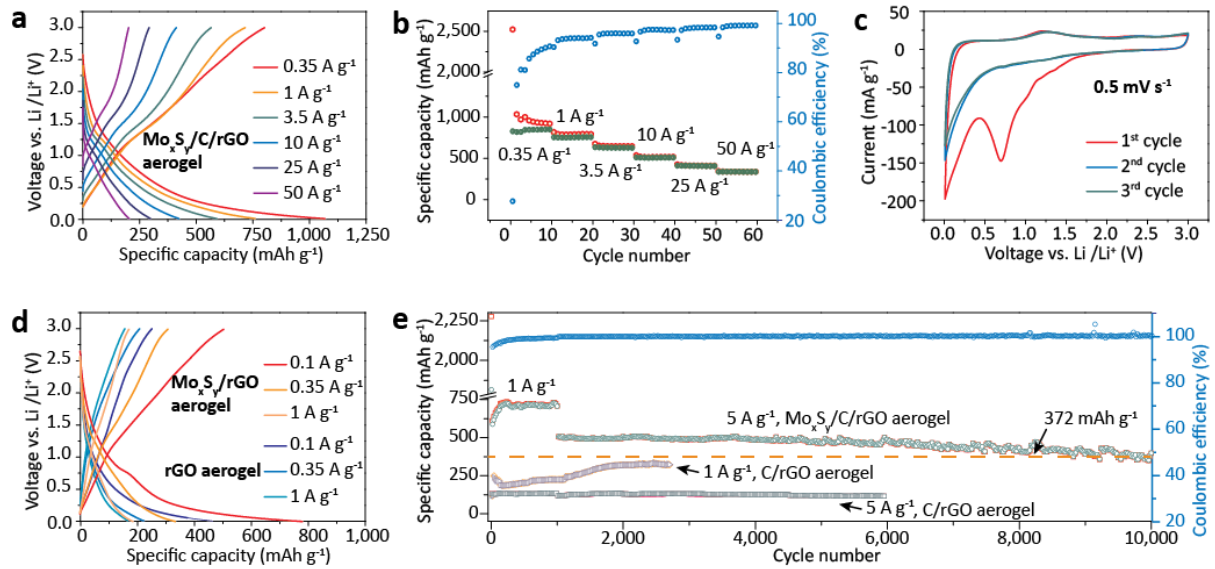


Figure 4.8 EC test of the $\text{Mo}_x\text{S}_y/\text{C}/\text{rGO}$ aerogel anodes. **a,b**, Cycling profiles for the composite aerogel at different current rates up to 50 A g^{-1} . **c**, The initial three cyclic voltammograms for the $\text{Mo}_x\text{S}_y/\text{C}/\text{rGO}$ aerogel anode. **d**, EC performance of the annealed $\text{Mo}_x\text{S}_y/\text{GO}$ and pure rGO aerogels at different current rates up to 1 A g^{-1} . **e**, Reversible capacity of the $\text{Mo}_x\text{S}_y/\text{C}/\text{rGO}$ aerogel over 10,000 cycles at 5 A g^{-1} in comparison with the performance of annealed PDA/GO (C/rGO) aerogels. Typical mass loading was between 0.6-1.0 mg cm^{-2} based on the whole composite. All the test were performed on at least 3 anodes.

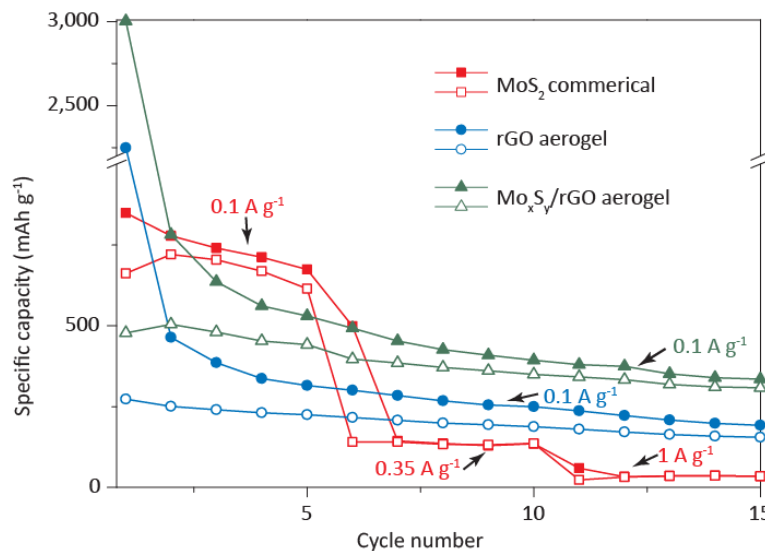


Figure 4.9 Cycling profiles for commercial MoS_2 , rGO aerogel and $\text{Mo}_x\text{S}_y/\text{rGO}$ aerogel at low current rates. Compared to the $\text{Mo}_x\text{S}_y/\text{C}/\text{rGO}$ composite aerogel, the rate-performance and cyclability of commercial MoS_2 , rGO aerogel and $\text{Mo}_x\text{S}_y/\text{rGO}$ aerogel are much inferior, which proves the success of the synergistic strategy of multiscale spacers between the graphene layers and N-doping for disordered graphene.

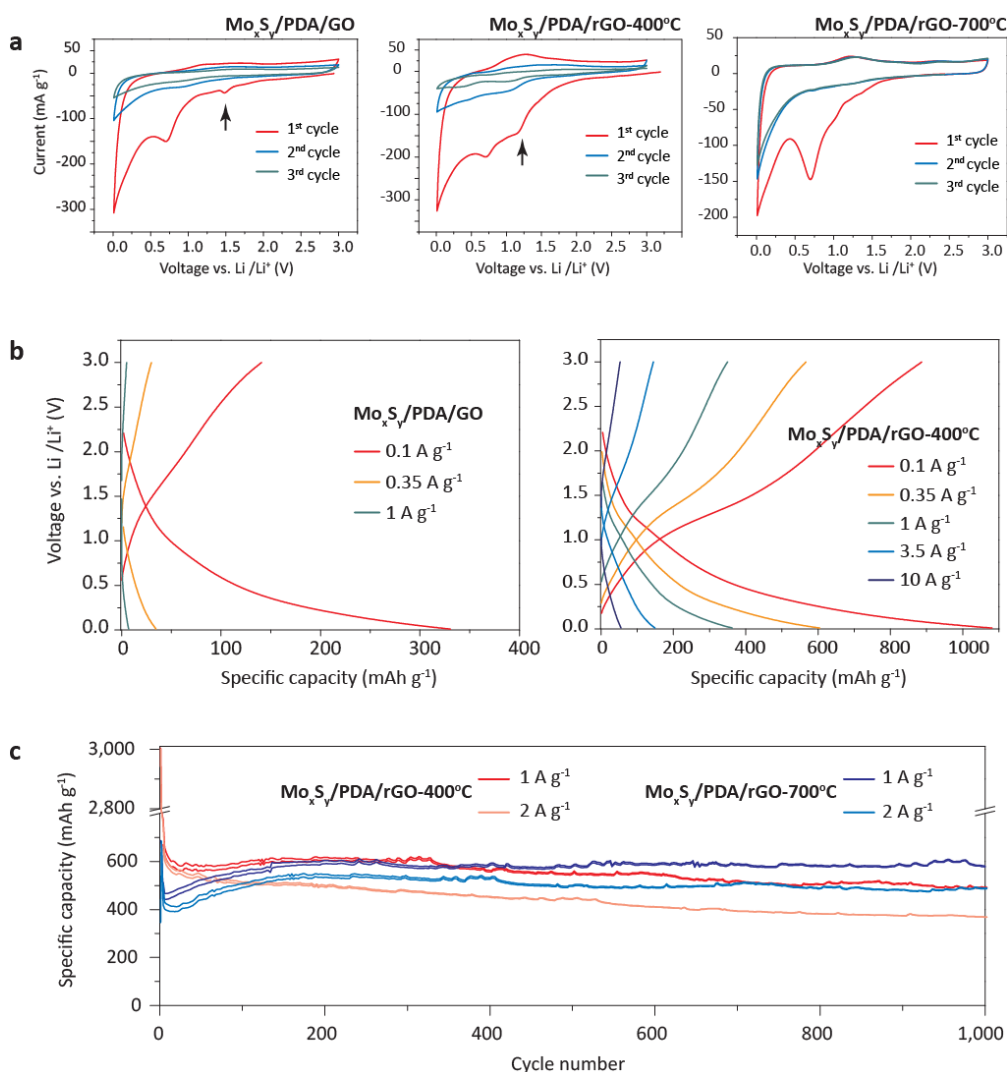


Figure 4.10 Thermal annealing effect on EC performance of different composite aerogels. **a**, CV scans (0.5 mV/s) for the Mo_xS_y/PDA/GO composite aerogel and its derivatives annealed at 400 °C and 700 °C, respectively. The peak around 0 V is attributed to Li⁺ adsorption onto graphene layers. The peak around 0.7 V can be attributed to SEI formation and initial reduction of Mo_xS_y. The peak around 1.5 V for the non-annealed sample slightly shifts to 1.4 V for the sample annealed at 400 °C, and completely disappears for the sample annealed at 700 °C. We ascribe this peak to the presence of functional groups in the graphene layers, which disappear with increasing annealing temperature. After the first CV scan, the aerogel annealed at 700 °C gives much more overlapping CV scans (2nd and 3rd cycles) in comparison to the other aerogels, indicating higher reversibility and Coulombic efficiency in later cycles. **b**, Cycling profiles for the pristine Mo_xS_y/PDA/GO and the sample annealed at 400 °C. Compared to the aerogel annealed at 700 °C (Fig. 3a in main text), the temperature apparently has a significant effect on the battery performance. A higher temperature (700 °C) leads to a higher degree of reduction of the graphene oxide, which gives rise to better conductivity, higher rate-performance and improved long-term stability. **c**, Long-term stability test of the Mo_xS_y/PDA/GO aerogel annealed at 400 °C and 700 °C at 1 A g⁻¹ and 2 A g⁻¹, respectively. The aerogel annealed at 700 °C shows both higher specific capacity and more stable cyclability over 1,000 cycles compared to the one annealed at 400 °C.

The graphene-based composite aerogel demonstrated outstanding electrochemical (EC) performance in terms of specific capacity, rate-performance and long-run cyclability. The rate-performance of the $\text{Mo}_x\text{S}_y/\text{C}/\text{rGO}$ aerogel is displayed in **Figure 4.8a,b**. At a low current rate of 0.35 A g^{-1} , it could discharge 1068 mAh g^{-1} . Increasing the current rate to impressive 50 A g^{-1} , the aerogel still delivered a reversible discharge of 204 mAh g^{-1} . With a balance between power and energy density, the composite aerogel supplied highly satisfactory capacity of 425 mAh g^{-1} at 10 A g^{-1} . The cyclic voltammogram (CV) at 0.5 mV s^{-1} for the initial three cycles is shown in **Figure 4.8c**. The first cathodic scan shows an irreversible peak at 0.75 V . This peak is ascribed to the formation of the solid electrolyte interphase (SEI) and the first reduction of the molybdenum species, and it disappears in the subsequent cycles. This observations suggest a stable SEI film, which prevented further contact between the electrolyte and the anode, leading to higher Coulombic efficiency. The cathodic peak centered at 0.01 V is attributed to the adsorption of Li-ions on graphene.^{150, 151}

In comparison to the $\text{Mo}_x\text{S}_y/\text{C}/\text{rGO}$ aerogels, other electrodes exhibited much inferior EC performance. Commercial MoS_2 delivered little capacity (**Figure 4.9**), annealed $\text{Mo}_x\text{S}_y/\text{GO}$ and rGO aerogels could merely discharge 186 and 166 mAh g^{-1} at 1 A g^{-1} , respectively (**Figure 4.8d & 4.9**). The long-term cyclability is a paramount parameter for practical use. The hierarchical $\text{Mo}_x\text{S}_y/\text{C}/\text{rGO}$ aerogel offered superior rate-performance and ultra-high stability after optimal annealing (**Figure 4.8e, 4.10 & 4.11**), delivering about 740 mAh g^{-1} at 1 A g^{-1} without any fading after 1,000 cycles. Even at 5 A g^{-1} it presented extraordinary stability. The capacity was maintained at 336 mAh g^{-1} (71.3% of the initial value of 471 mAh g^{-1} at 5 A g^{-1}) for additional 9,000 cycles, with average Coulombic efficiency close to 100% (**Figure 4.8e**). In contrast, the annealed PDA/GO (C/rGO) aerogel, with the same design concept but without Mo_xS_y spacers, could discharge 324 mAh g^{-1} at 1 A g^{-1} for 2700 cycles, however, its capacity at higher rate was significantly lower. At 5 A g^{-1} the initial capacity was only $\sim 131 \text{ mAh g}^{-1}$, and it further dropped to 115 mAh g^{-1} after 6,000 cycles, which again underlines the success of our strategy with three types of spacers.

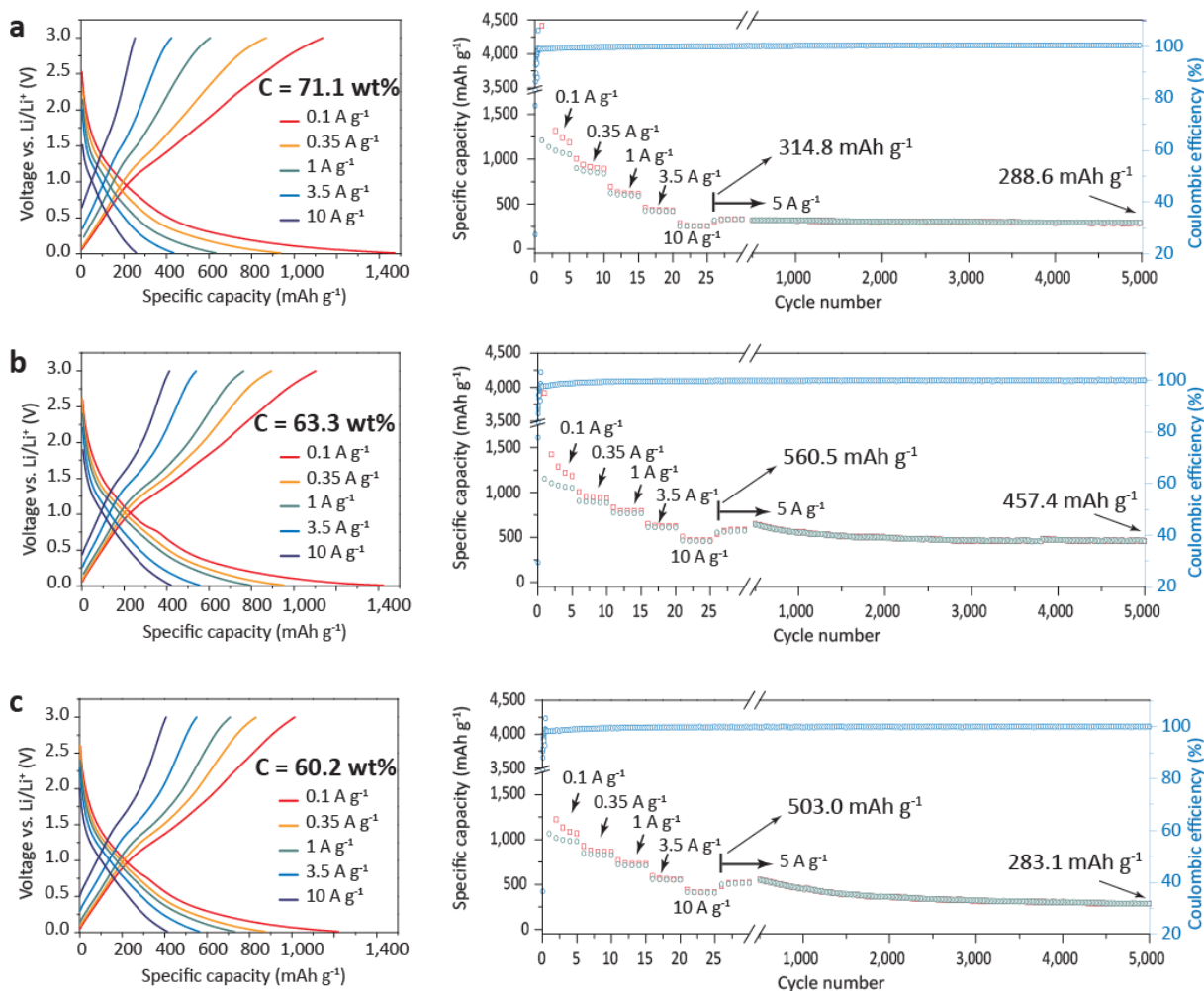


Figure 4.11 Different mass ratios of the spacers in the $\text{Mo}_x\text{S}_y/\text{C}/\text{rGO}$ composite aerogels and comparison of their EC performance having a, carbon content of 71.1 wt% (lowest loading of the spacers), b, 63.3 wt% of carbon (medium loading of the spacers) and c, 60.2 wt% of carbon (highest loading of the spacers). The amount of spacers can be varied. However, a lower loading of spacers reduced the effective area mass loading due to the lower density of GO, while a higher loading of spacers weakened the mechanical strength of the composite aerogel. In general, all the EC performance was outstanding in terms of specific charge, rate-performance and long-term cyclability. With less spacers, the composite a demonstrates the best capacity retention after 5000 cycles at 5 A g^{-1} (314.8 to 288.6 mAh g^{-1} , 91.7%), however at lowest capacity. With more spacers, the composite c offered much higher capacities under the same conditions, but with the lowest stability (503.0 to 283.1 mAh g^{-1} , 56.3%). After optimizing the loading of the spacers, composite b not only gives the most specific charges, but also excellent capacity retention (457.4 to 560.5 mAh g^{-1} , 81.6%). All the tests were performed on at least 3 anodes. The carbon content was determined by microelemental analysis on a LECO TrueSpec.

It is known that highly disordered graphene containing many defects, *e.g.* dopants, vacancies and edges, can provide additional reversible storage sites.¹³³ To elaborate the high capacity of the graphene-based composite aerogel, Raman spectroscopy was used to study the degree of disorder. In the Raman spectra of graphene, the characteristic G band arises from the zone center E_{2g} mode, corresponding to ordered sp^2 carbon, while the D peak is due to the breathing modes of six-atom rings and requires a defect for its activation.¹⁵² Therefore, the I_D/I_G intensity ratio is a measure for the degree of disorder in graphitic materials.¹⁵³ In **Figure 4.12a**, an evidently increasing I_D/I_G ratio was observed from the original GO sample to the final product, the $Mo_xS_y/C/rGO$ aerogel obtained after annealing at 700 °C. The decreasing intensity of the G band arises from the destruction of the E_{2g} symmetry and from the structural distortion of the sp^2 domains induced by the modification of the graphene lattice by N atoms as a result of PDA and NMP pyrolysis.

To further elucidate the excellent EC behavior of the graphene-based composite aerogels, different characterization techniques were applied to investigate the electrodes before and after cycling. Electrochemical impedance spectroscopy (EIS) measurements (**Figure 4.12b**) showed a relatively high interface and charge-transfer resistance at high frequencies (semicircle regime) for the pristine electrodes, while after the activation during the 1st cycle the semicircle regime was significantly reduced, and with every additional cycle it became smaller. This behavior suggests a lowering of the contact resistance.⁹⁸ Besides, the Warburg coefficient (which can be calculated from the inclined line regime) consecutively decreased with increasing number of cycles, indicative of higher Li-ion diffusion rates.¹⁵⁴ In **Figure 4.12c**, ex-situ X-ray photoelectron spectra (XPS) performed for cells cut off at different voltages clearly confirmed that the Mo_xS_y spacers contributed reversible capacity to the composite aerogel via redox reactions involving Mo, while sulfur mainly provided the 1st irreversible capacity via the S^{6+}/S^{2-} reaction. According to Fig. 4d, the microstructure of the composite did not significantly change, when the electrodes were fully lithiated at 0.01 V, de-lithiated at 3 V after 1 cycle and 100 cycles, respectively.

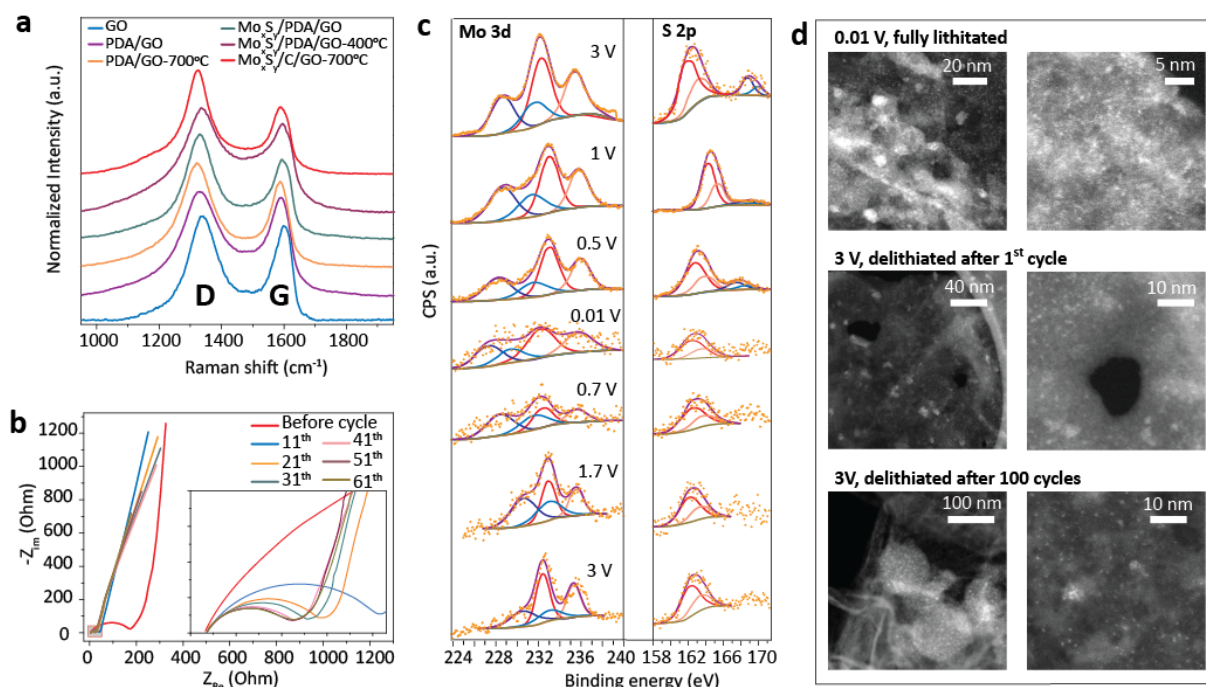


Figure 4.12 Characterization of the Mo_xS_y/C/rGO aerogel anodes at different synthesis stages and after lithiation. **a**, Raman spectra recorded for GO, PDA/GO and Mo_xS_y/PDA/GO aerogels annealed at different temperatures. The spectra intensity was normalized with respect to the D band. **b**, Impedance spectra plotted after different cycles. The inset magnifies the hemi-circle part in the high frequency regime. **c**, High-resolution XPS spectra of Mo 3d and S 2p recorded for cells cut off at different voltages. **d**, STEM images of the composite aerogels, which were fully lithiated and delithiated after 1 cycle and 100 cycles, respectively.

4.3 Conclusion

We developed novel graphene-based composite aerogels in which polydispersed particles as spacers on different size scales were homogeneously incorporated in between the graphene sheets, giving access to a 3-dimensional, porous and hierarchical architecture. In addition, the spacers acted as N-dopant sources, introducing a large degree of disorder into graphene. All of these factors synergistically contribute to a substantially improved cyclability at high current rates (up to 10,000 cycles at 5 A g⁻¹). With great potential for low-cost manufacturing of GO, our electrode design and fabrication method represents a significant advancement toward the practical use of graphene-based lithium ion batteries. In addition, the architectural design concept can be easily extended to other applications, *e.g.* supercapacitors or catalysts.

4.4 Experimental section

Preparation of Mo_xS_y aqueous suspension. 0.5 ml of N-methyl-2-pyrrolidone (NMP, Acros, 99%) was added to 1 g of commercial MoS_2 (Aldrich, $<2 \mu\text{m}$, 99%) in a ball milling jar (15 ml capacity), and then the black slurry was ball milled for 1.5 h at a frequency of 20 Hz. After ball milling, the highly viscous slurry was dried in a vacuum oven (10 mbar) at 60°C until it was dry. The dry product was scratched off the jar, gently ground into a fine powder with a mortar and pestle. The powder was dispersed into 45 vol% ethanol-water solution (25ml), followed by ultra-sonication for 2 h ($f = 37 \text{ Hz}$, pulse mode). The dispersion was centrifuged for 30 min at 4000 rpm. The sediment was dark grey in color and the supernatant was light blue. Only the supernatant (Fig. 2a inset), which was stable for months without sedimentation, was further processed. However, the concentration of the as-prepared supernatant was not high enough ($< 1\text{mg/ml}$). Therefore, 25 ml of Tris-HCl buffer (100 mM, $\text{pH} = 8.5$) were added to the Mo_xS_y dispersion, and then the whole mixture was concentrated by rotary evaporation until the concentration was above 10 mg/ml. The dispersion was now dark green and gradually precipitated in 2-3 hours. However, upon shaking it could be re-dispersed well. It is worth mentioning that the MoS_2 sediment after the centrifugation step could be re-recycled for ball milling again and thus be reused for new Mo_xS_y dispersion.

Preparation of aqueous Mo_xS_y /PDA and PDA dispersions. Dopamine hydrochloride (100 mg, Sigma-Aldrich) was added to the concentrated Mo_xS_y dispersion (10 ml, 10 mg/ml). Upon the addition of dopamine hydrochloride, the color immediately turned to brown. The mixture was put into an oil bath set at 60°C and stirred for 3h. The color gradually changed to dark wine-red. The product was centrifuged off and washed three times with ethanol. The yielded product was black in color and re-dispersed into milli-Q H_2O (concentration: 10 mg/ml). The PDA blended Mo_xS_y dispersion was stable for several hours, after which it could be re-dispersed again upon shaking. The pure PDA spheres without Mo_xS_y were obtained by adding dopamine hydrochloride (100 mg) into 10 ml of Tris-HCl buffer (100 mM, $\text{pH} = 8.5$), heated at 60°C and stirred for 2-20 h.

Fabrication of Mo_xS_y /PDA/GO and Mo_xS_y /GO composite aerogel. The Mo_xS_y /PDA dispersion (10 mg/ml) was mixed with an aqueous GO dispersion (5 mg/ml, Royal Elite, Shanghai). The mixture was shortly vortex shaken and sonicated for 2 min, and then transferred onto a petri-dish like current collector (made of Ti, Cu or Al), sealed in a closed bottle, and cured under a saturated H_2O vapor environment at 95°C . After 6 h, a monolithic hydrogel film formed without obvious volume shrinkage. The gel was carefully put into an excess of acetone for solvent exchange twice (24 h), followed by supercritical drying in CO_2 . A monolithic, crack-free aerogel film with minimum thickness of $\sim 100 \mu\text{m}$ was obtained. The shape of the final aerogels are dependent on the shape of the containers. If a Teflon substrate was used, also a free-standing film with some extent of volume shrinkage could be produced. The typical mass loadings of the composite aerogels are around $1\text{-}2 \text{ mg/cm}^2$. Higher mass loading could be obtained when more concentrated Mo_xS_y /PDA and GO suspension were used; however, when the concentration of the GO dispersions was higher than 10 mg/ml, it became highly viscous, which led to inhomogeneous mixture of the different components in the aerogels. For the fabrication of the Mo_xS_y /GO aerogels, a similar approach was employed, but

the Mo_xS_y was not combined with the PDA beads. Similarly, the pure GO aerogels were produced, just without Mo_xS_y and PDA.

Annealing of Mo_xS_y /PDA/GO composite aerogel. To optimize the battery performance, the supercritically dried Mo_xS_y /PDA/GO composite aerogels on Ti current collectors were thermally annealed under slightly reducing atmosphere (5 vol% H_2 in N_2). Even after annealing, the volume of the composite Mo_xS_y /C/rGO aerogels did not shrink, but the change in mass was dependent on the annealing temperature. After annealing at 400 °C, the mass of the composite aerogels did not change much. When the temperature was raised to 700 °C, the mass significantly dropped by 40-60 wt%, however without obvious volume change, indicating that PDA/ Mo_xS_y transformed to Mo_xS_y /amorphous carbon composite, and that GO was further reduced to rGO. After annealing at 700 °C, the typical mass loading was 0.6-1.0 mg/cm².

Electrode preparation. All monolithic aerogel samples with/without annealing were directly used as binder-free anodes. For comparison, commercial MoS_2 electrodes were prepared in a conventional way, *i.e.*, 60 wt% of MoS_2 was uniformly mixed with 30 wt% of carbon black (Super P, TIMCAL), 10 wt% of PVDF (polyvinylidene fluoride, Aldrich) in NMP (N-methyl-2-pyrrolidinone, Fluka) under mechanical stirring. The resulting paste was transferred onto a Ti current collector and vacuum dried at 100 °C overnight. The average electrode loading was 1-1.5 mg/cm². To systematically prove the beneficial role of the multiscale spacers, rGO, Mo_xS_y /rGO and PDA/rGO aerogels annealed at 700 °C were used as anodes in battery tests for comparison.

Electrochemical Measurements. Electrodes were assembled into Swagelok-type cells in an Ar filled glove box (H_2O , O_2 < 0.1 ppm). Li metal (99.9%, Alfa-Aesar) served as both reference and counter electrode. A piece of glass fiber or Celgard 2500 separator was soaked with electrolyte (1 M LiPF_6 in 1:1 wt% ethylene carbonate (EC)/dimethyl carbonate (DMC), Novolyte). All electrochemical measurements were performed using a Biologic instrument (VMP3) at room temperature. The electrodes were cycled between 0.01 and 3 V vs. Li/Li^+ at varying specific current rates. Electrochemical impedance spectroscopy (EIS) measurements were carried out at an amplitude of 10 mV over the frequency from 100 kHz to 0.01 Hz on the pristine electrodes as well as on the ones that went through different cycles. Between each EIS test, the rest time was 12 hours.

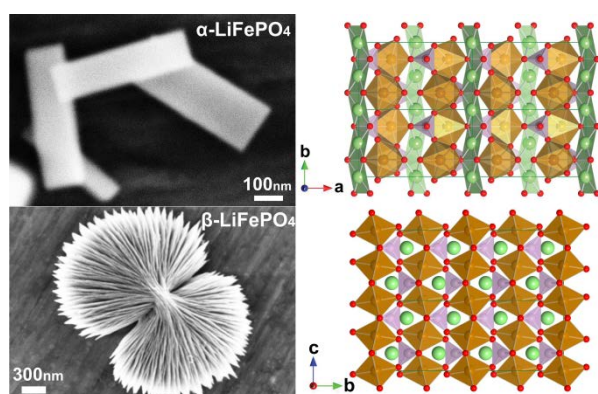
Characterizations. X-ray powder diffraction (XRD) patterns were recorded using a diffractometer from PANalytical (Empyrean with monochromator, $\text{Cu K}\alpha$ radiation). The morphological and elemental analyses were performed on a LEO 1530 Gemini scanning electron microscope (SEM) operating at 5 kV and on a FEI Talos F00X transmission electron microscope (TEM) operating at 200 kV in both scanning transmission electron (STEM) and transmission electron (TEM) modes. The TEM tomography study was also performed on the Talos in both TEM and STEM modes with a 2 degree step of the 140 degree tilting range. The SuperX EDX-system of Talos was employed for the high resolution elemental distribution studies in hypermap and line-scan modes. X-ray photoelectron spectra (XPS) were recorded on a Sigma 2 spectrometer (Thermo scientific) using a non-monochromatic $\text{Al K}\alpha$ X-ray source, where binding energy was calibrated taking $\text{C 1s} = 284.5$ eV. Nitrogen adsorption/desorption isotherms were measured on a Quantachrome Autosorb-iQ to

acquire specific surface area by multi-point BET method and pore size distribution by BJH and DFT method, respectively. Nuclear magnetic resonance (NMR) spectra were acquired on a Bruker AV400 spectrometer (Bruker BioSpin) operating at 400 MHz for protons. Chemical shifts (δ) are reported in ppm relative to residual solvent signals. Microelemental analysis was performed on a LECO TrueSpec. Raman spectroscopy was performed on an InVia Raman Microscope from Renishaw (UK), using the 532 nm line of an Ar Laser and spectra were recorded at room temperature in backscattering configuration.

Chapter 5 Conclusion

The general task through this PhD dissertation was to develop advanced electrode materials on nanoscale and to optimize nanostructured electrode architectures, aiming at better Li-/Na- ion batteries. We mainly focused on three scenarios: microwave-assisted synthesis of LiFePO_4 as cathodes, spinel-type metal oxide/rGO composite aerogels and hierarchical graphene-based aerogels as anodes in LIBs.

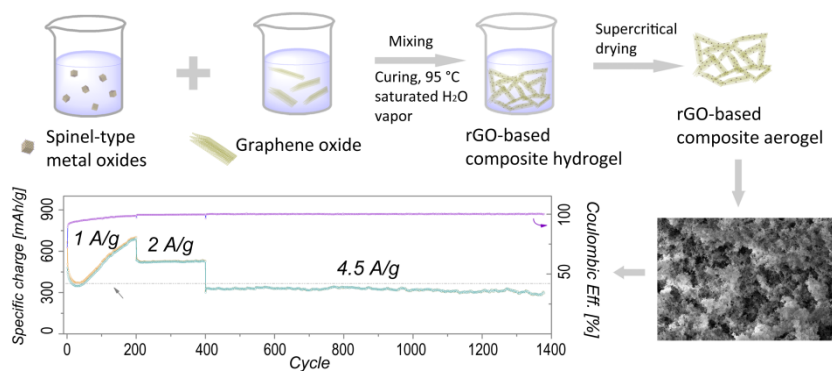
5.1 Tailoring the polymorphs & morphologies of LiFePO_4 as cathodes



Olivine- LiFePO_4 (α -phase) has been one of the most successful cathode candidates for LIBs so far, and has been extensively studied. Upon high pressure (65 kbar) and elevated temperature (900 °C), α - LiFePO_4 transforms into the high-pressure phase (β - LiFePO_4) that is much less known.

We presented an easy way to access both phases of LiFePO_4 by a time-efficient microwave-assisted nonaqueous process. Depending on the solvent used, not only the crystal structure varies, but also the particle morphology. Although the β - LiFePO_4 presents a sophisticated, hierarchically self-assembled bow tie-like morphology, which is expected to be ideal for Li-ion battery applications, it is electrochemically almost inactive. DFT-based molecular dynamics calculations at different sampling temperatures indicated that in β - LiFePO_4 Li ions were only able to rattle in the voids without the possibility of hopping. On the other hand, α - LiFePO_4 offered excellent electrochemical performance after carbon coating in spite of the relatively simple platelet-like morphology. According to the calculations, in α - LiFePO_4 the motion of Li ions are concerted and cooperative along the $[0\ 1\ 0]$ direction. After thermal annealing, β - LiFePO_4 transforms into the α -phase, and then the electrochemical performance is greatly improved.

5.2 Spinel-type metal oxide/rGO composite aerogels as anodes



Spinel-type metal oxides (AB_2O_4) are able to deliver high capacities *via* conversion reaction mechanism. However, they generally suffer from poor Li^+ and e^-

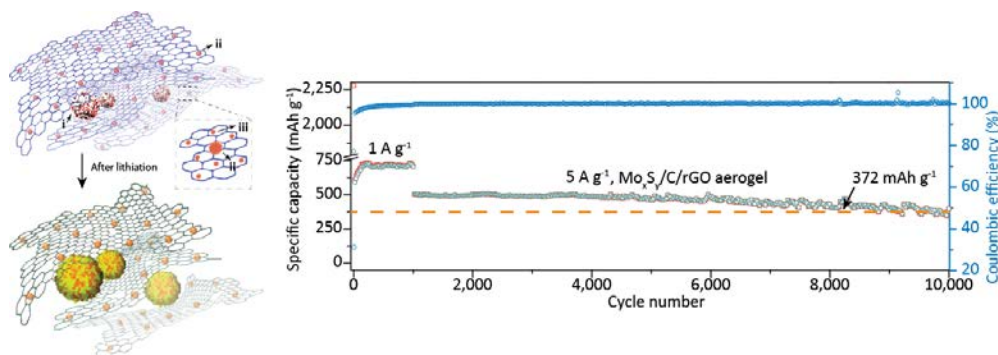
conductivities and the drastic volume changes upon Li -ion uptake severely impede their high-rate and cyclability performance towards the practical application.

Directly using spinel-type metal oxide nanoparticles (NPs) and graphene oxide (GO) as building blocks with their tailored surface charges, we developed a facile method to fabricate composite metal oxide/reduced graphene oxide (rGO) aerogels with any desired shape that can directly be used as binder-free anodes in Li -ion batteries. Benefitting from several structural features provided by the carefully designed electrode architecture, including hierarchical porosity, conductive network and mechanical stability offered by the inter-penetrated rGO layers, and the pillar effect of NPs in between the rGO sheets, the hybrid system synergistically enhances the intrinsic properties of each component. Consequently, the spinel/rGO composite aerogel demonstrates much enhanced rate capability and long-term stability without obvious capacity fading after 1000 cycles at high rates. We believe that the strategy presented here can be extended to other metal oxides, sulphides, and alloys (*e.g.* Ge or Sn) for the preparation of advanced anodes in Li -ion batteries.

5.3 Hierarchical graphene-based aerogels as anodes

Inspired by the spacer concept above, we further generalized the strategy of composite aerogels used in LIBs. We reported novel graphene-based composite aerogels in which polydispersed particles as spacers on different size scales were homogeneously incorporated in between the graphene sheets, giving access to a 3-dimensional, porous and hierarchical architecture. In addition, the spacers acted as N-dopant sources,

introducing a large degree of disorder into graphene. All of these factors synergistically contribute to a substantially improved cyclability at high current rates (up to 10,000 cycles at 5 A g^{-1}). With great potential for low-cost manufacturing of GO, our electrode design and fabrication method represents a significant step forward toward the practical use of graphene-based Li-ion batteries.



In addition, the concept can be easily extended to other applications, *e.g.* supercapacitors or catalysts.

5.4 Additional remarks

So far, we discussed a lot how we decreased the particle size to nanoscale, how we designed nanostructured electrode architectures and how these strategies successfully led to outstanding electrochemical performance of Li-ion batteries. However, “nanoscale” is not always a “penicillin” that could solve all problems in batteries. The effective increase in the electrodes’ surface area is at the expense of other disadvantages. If one recalls the section 1.5 where we discuss that 1) high electrolyte/electrode surface area may lead to more significant side reactions with the electrolyte, thus much lower initial Coulombic efficiency, and 2) the density of a nanostructured electrode is less than that of micrometer-sized particles, therefore, reducing the volumetric energy density. These two issues are as equally important as other properties for battery electrodes of choice, *e.g.* energy/power density or cyclability, when considered to be practically useful for massive industry production.

In addition, 3) electrode materials at smaller scale are beneficial for lower polarization, *i.e.* “nanoscale and nanoengineering” can alleviate the issue of polarization, but the working voltage is determined by their intrinsic redox potential after all.

There is a close link between industry and academia for battery research, very often, the gap exists though. And the gap, in my personal opinion, is necessary. Only because of that, we can focus on something more fundamental, or sometimes, simply for fun. This will finally make a difference.

Chapter 6 Other Projects

In this Chapter, I am going to very briefly describe some other projects which are:

- collaborated with other excellent researchers inside or outside of ETH Zurich;
- on-going project; and
- not-published yet.

6.1 Ni:MoO₂, XANES & EXAFS study

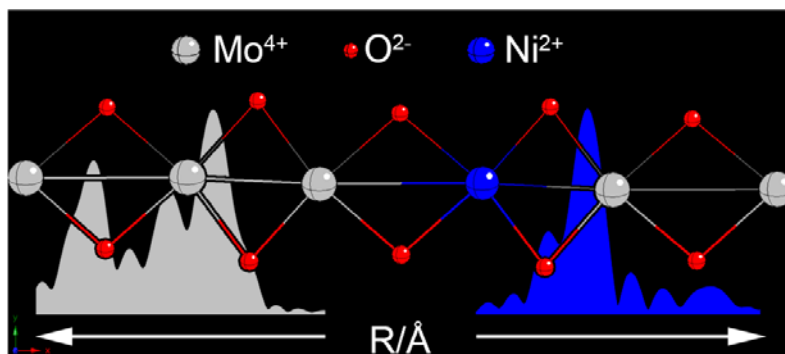


Figure 6.1 In this project, we present a synthesis of MoO₂ nanoparticles doped with 2 at% of Ni in a mixture of acetophenone and benzyl alcohol at 200 °C. Based on in situ X-ray absorption near-edge structure (XANES) and ex situ extended X-ray absorption fine structure (EXAFS) measurements at Ni K-edge and Mo K-edge, we discuss scenarios on how the “doping” reaction, that is, the incorporation of Ni in the MoO₂, proceeds. We can clearly exclude the formation of NiO or Ni nanoparticles. Moreover, within the resolution of our in situ XANES experiments, we observe that the ternary compound Ni:MoO₂ nucleates directly in the final composition. Although the local structure around the Ni ion adopts the MoO₂ crystal structure pointing at the substitution of tetravalent Mo by Ni, we find that Ni remains divalent. This aliovalent substitution results in the relaxation of the local structure, which is additionally reflected in the slight shrinking of the total volume of the unit cell of Ni:MoO₂. Interestingly, such a small amount of divalent Ni has a tremendous effect on the performance of the material as anode in LIBs. The initial discharge capacity of Ni:MoO₂ based anodes almost doubles from 370 mAh/g for MoO₂ to 754 mAh/g for Ni:MoO₂ at 0.1 C (1 C = 300 mA/g).

The detail of this work was published in *Chem. Mater.* **2014**, 26, 4505-4513 entitled “[Aliovalent Ni in MoO₂ Lattice - Probing the Structure and Valence of Ni and Its Implication on the Electrochemical Performance](#)” with authorship O. Hirsch[†], G. Zeng[†], L. Luo, M. Staniuk, P. M. Abdala, W. van Beek, F. Rechberger, M. J. Süess, M. Niederberger, D. Koziej* ([†]equal contribution).

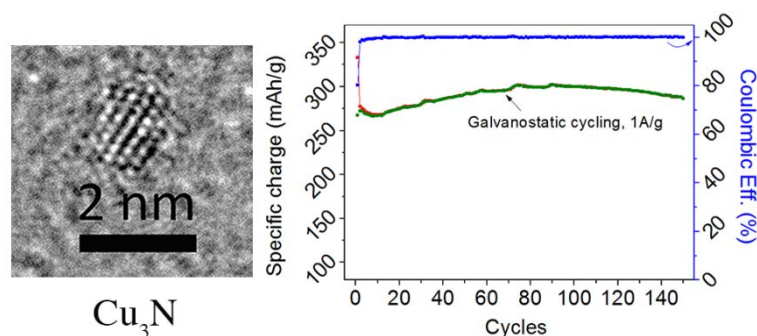
6.2 Cu₃N

Figure 6.2 In this project, we report a novel surfactant-free, solution-phase, low temperature route to crystalline, ultrasmall (~ 2 nm) Cu₃N nanoparticles via a one-step reaction between copper(II) methoxide and benzylamine. We propose a reaction mechanism for Cu₃N formation based on the gas chromatography-mass spectrometry (GC-MS) analysis of the organic reaction byproducts. The reaction pathway involves reduction of the Cu(II) to Cu(I) by benzylamine, in situ generation of ammonia and finally, the reaction between Cu(I) and ammonia to form Cu₃N. We tested the Cu₃N nanoparticles as an anode material for Li-ion batteries. According to cyclic voltammetry, the Cu₃N nanoparticles quickly undergo a phase transformation to Cu₂O, but then stably deliver a capacity of ~ 290 mAh g⁻¹ at 1 A g⁻¹ in the following 150 cycles.

The detail of this work was published in *Chem. Mater.* **2015**, 27, 8282-8288 entitled "Ultrasmall Cu₃N Nanoparticles: Surfactant-Free Solution-Phase Synthesis, Nitridation Mechanism, and Application for Lithium" with authorship R. Deshmukh*, G. Zeng, E. Tervoort, M. Staniuk, D. Wood, M. Niederberger*.

6.3 Vanadium oxides

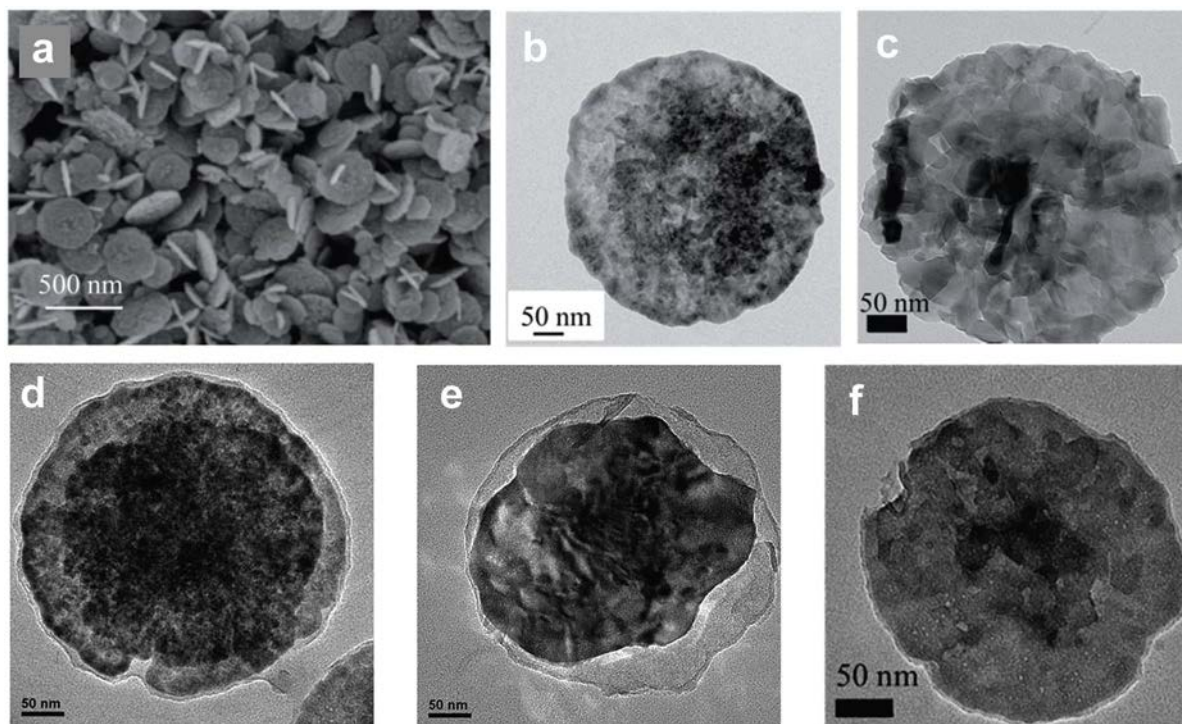


Figure 6.3 Vanadium oxides are promising electrode materials for Li-ion batteries, V_2O_5 as cathode and V_2O_3 as anode. However, both of them suffer from poor cycling stability and low rate performance. Reducing their particle size to the nanometer range and fabricating core-shell structures represent two versatile strategies to improve their electrochemical performance. In this work, we developed a solution route to round V_2O_3 nanoplatforms with diameters of about 400 nm and thicknesses of about 20 nm. They can be successfully transformed into hierarchical V_2O_5 , into V_2O_3 @amorphous carbon core-shell structures with tunable carbon layer thickness and into hierarchical V_2O_5 @ TiO_2 core-shell structures under full preservation of the 2-dimensional morphology. As an anode material, the carbon composite exhibits higher specific capacity and better cycling stability and rate performance in comparison to the pure V_2O_3 nanoplatforms. They can deliver a highly reversible capacity of 261 $mAh\ g^{-1}$, 200 $mAh\ g^{-1}$ and 122 $mA\ h\ g^{-1}$ at of 100 $mA\ g^{-1}$, 400 $mA\ g^{-1}$, and 1600 $mA\ g^{-1}$, respectively. As a cathode material, the V_2O_5 nanoplatforms@ TiO_2 cycled at 150 $mA\ g^{-1}$ for 100 times deliver a high initial discharge capacity of 211 $mA\ h\ g^{-1}$ with a high Coulombic efficiency of 99.1%.

The detail of this work was published in *J. Mater. Chem. A* **2015**, 3, 2861-2868 entitled "Design of Vanadium Oxide Core-shell Nanoplatforms for Lithium Ion Storage" with authorship W. Cheng, G. Zeng, M. Niederberger*.

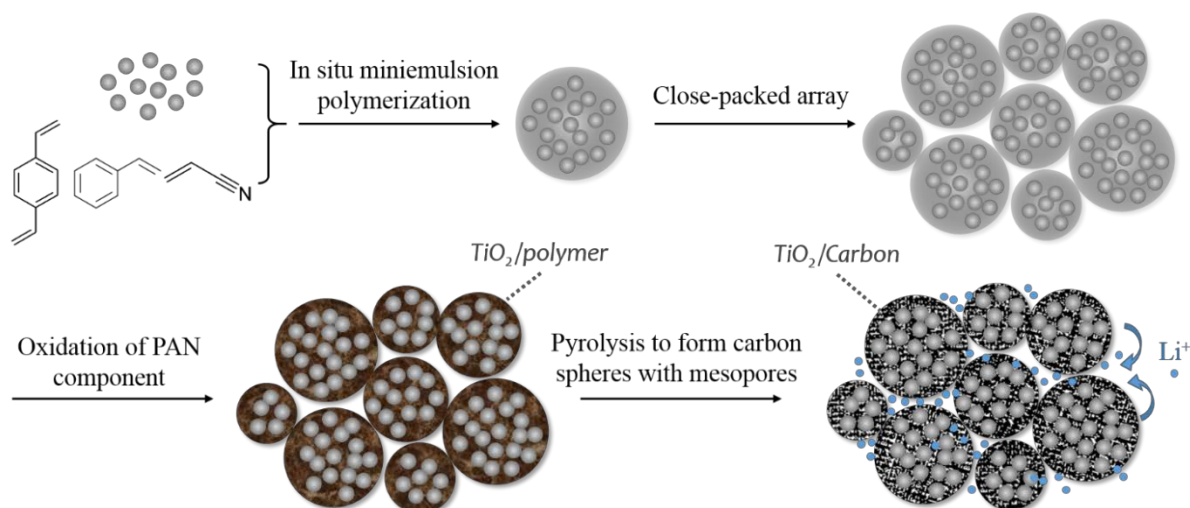
6.4 TiO₂

Figure 6.4 In this project, a general methodology is proposed to produce active cathode/anode materials for lithium ion batteries with a hierarchical structure. In particular, the active electrode materials in nano dimension (<10 nm) are carbon-coated and encapsulated inside submicron-scale graphite-like carbon spheres derived from suitable copolymer prepared through mini-emulsion polymerization. The graphite-like carbon matrix inside the spheres supplies high conductivity and mechanical rigidity and keeps well separated the nanoparticles of the active materials to avoid their aggregation. The carbon spheres possess mesopores for improving diffusion of Li ions in and out of the active materials, and for accommodating possible volume changes. The inter-space among the carbon spheres provides continuous channels which facilitate electrolyte infiltration. The proposed methodology has been applied to prepare anatase TiO₂/carbon anode materials. The Li-ion battery prepared using this anode material exhibits a reversible capacity of 173 mAh g⁻¹ at 500 mA g⁻¹, with a negligible capacity fading even after 600 cycles. Moreover, the applied preparation route can be easily scaled up for industrial productions.

This project was a collaboration with Morbidelli Group at ETH Zurich. The detail of this work used as Li-ion batteries was submitted with authorship L. Jin, G. Zeng, H. Wu*, M. Niederberger and M. Morbidelli*.

6.5 LiFePO₄ sticks formation mechanism

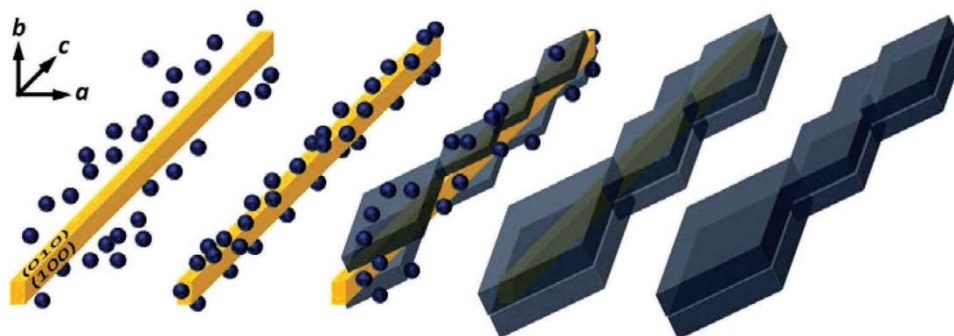


Figure 6.5 A time-dependent study on the formation of LiFePO₄ with olivine-type structure is presented. The material is synthesized through a non-aqueous route in benzyl alcohol assisted by microwave radiation. The LiFePO₄ forms with an anisotropic morphology of microscale stick-like particles. The detailed structure of these particles and their evolution with reaction time is revealed by transmission electron microscopy; a 3D reconstruction of a particle by electron tomography provides insight into the formation mechanism of these sticks. Without applying a thermal post-annealing treatment or a carbon coating, the electrochemical behavior of the LiFePO₄ microsticks is assessed for the preparation of cathodes in Li-ion batteries.

The detail of this work was published in *Small* **2012**, 8, 2231-2238 entitled “[Formation Mechanism of LiFePO₄ Sticks Grown by a Microwave-Assisted Liquid-Phase Process](#)” with authorship D. Carriazo*, M. D. Rossell, G. Zeng, I. Bilecka, R. Erni, M. Niederberger.

6.6 LiFePO_4 with varied morphologies and phases

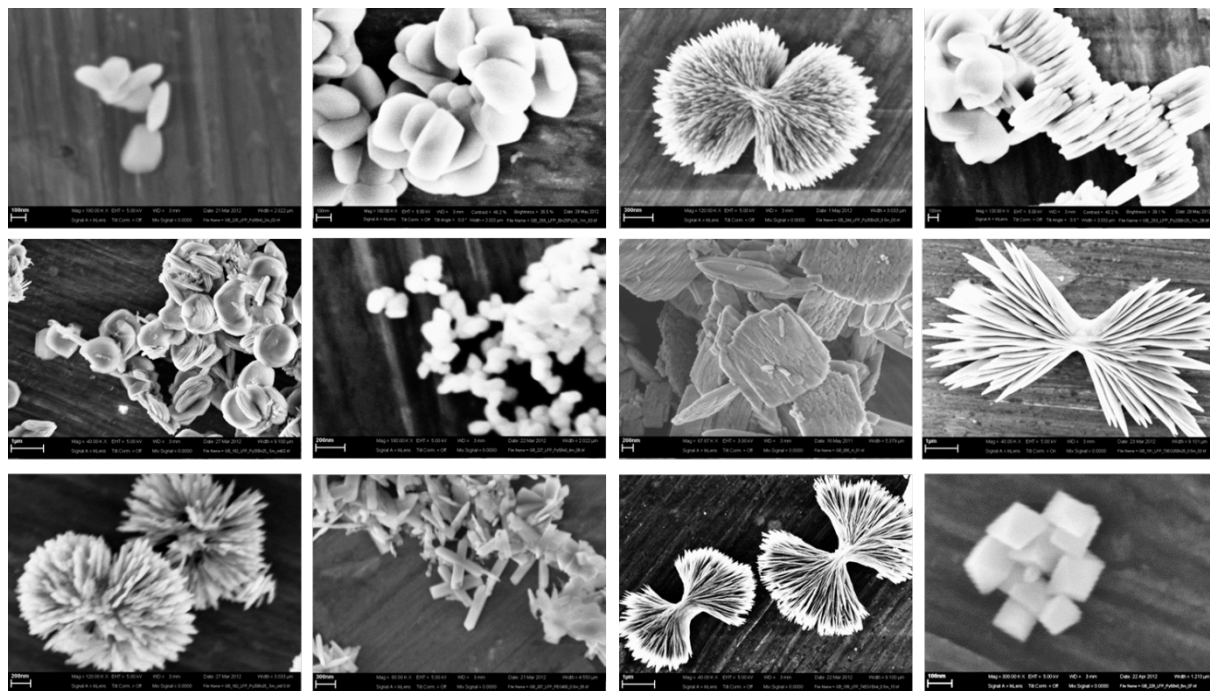


Figure 6.6 In addition to Chapter 2 where we successfully tailor the polymorphs and morphologies of LiFePO_4 by tuning the solvent ratio, actually we can do much more than that. The synthesis of LiFePO_4 via microwave-assisted non-aqueous sol-gel route is very sensitive to other parameters, *e.g.* concentration, temperature, solvent etc. Above we list a few graphs of LiFePO_4 that either belong to α -, β -phase or the mixture of both. Through controlling the parameters during the synthesis, we can obtain LiFePO_4 with varied morphologies and particle sizes. To correlate between the LiFePO_4 phase formation and synthesis parameters, we are carrying out more experiments in the hope that we can rationalize the synthesis conditions and finally predict the phase formation.

The project is still on-going, and the manuscript is under preparation.

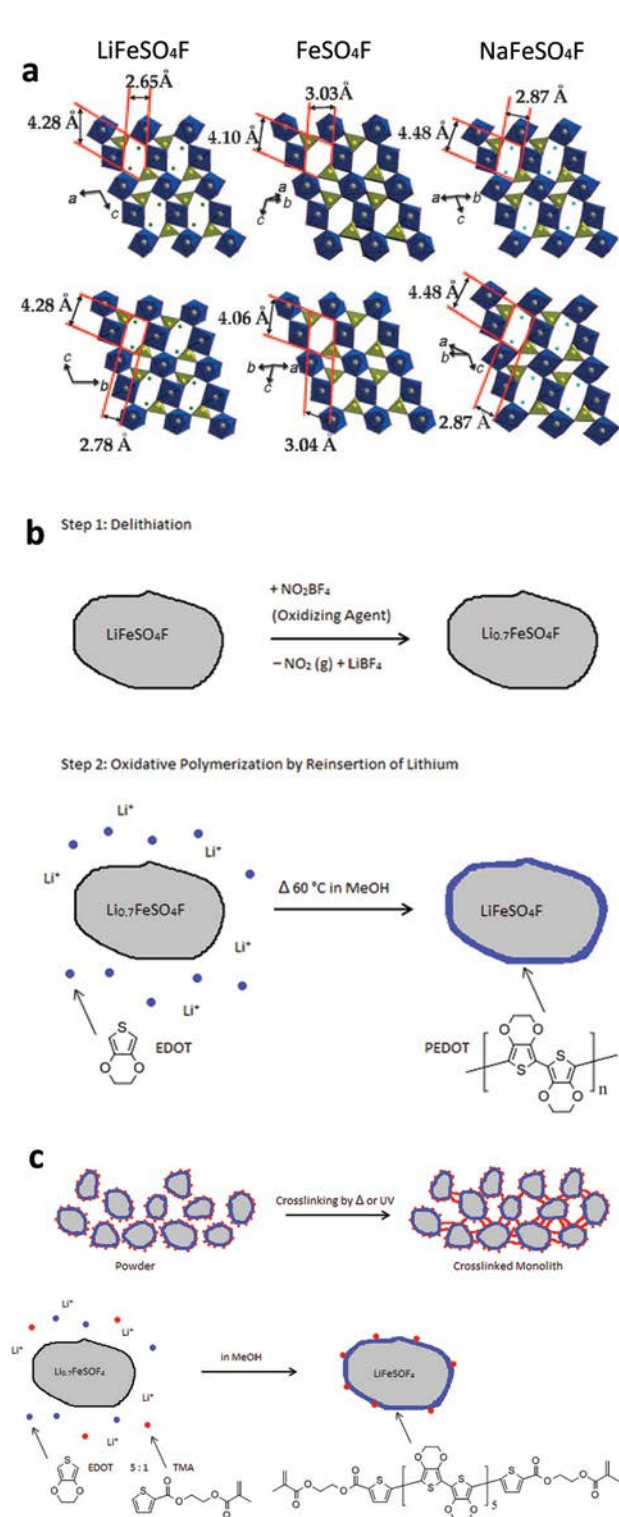
6.7 LiFeSO₄F & NaFeSO₄F

Figure 6.7 Encouraged by the discovery of LiMgSO₄F in 2002 which shows a much enhanced Li-ion conduction, the synthesis of LiFeSO₄F was first reported in 2009 by Tarascon *et al.* who synthesized the material in hydrophobic ionic liquid, EMI-TFSI.¹⁵⁵ We thought it might be feasible to replace the expensive ionic liquid with much cheaper hydrophilic tri- or tetra-ethylene glycol via microwave-assisted synthesis route. Indeed, it worked out both for LiFeSO₄F that can be obtained within several hours and NaFeSO₄F that even could be done in seconds as shown in **Graph a**. When we were struggling with stabilizing/optimizing the synthesis conditions and the inactive electrochemical property of NaFeSO₄F, we sadly found other groups were quicker than us. Similar work was published by Nazar *et al.*¹⁵⁶ and Tang *et al.*¹⁵⁷

Later, we thought it might be interesting to do some in situ conducting polymer coating since LiFeSO₄F is moisture sensitive. We tried to surface oxidize LiFeSO₄F to Li_{1-x}FeSO₄F which was used as oxidative reagent, and formed a thin layer of conducting polymer, PEDOT, on LiFeSO₄F particle surface (**Graph b**). The idea worked quite well. When we tried to maximize the battery performance, we were late again. Similar work was published.¹⁵⁸ Gian Cadisch was doing his Master thesis with me on this topic. Both of us were discouraged.

But Gian continued, he thought that the thiophenemethacrylate (TMA) end capped PEDOT could be cross-linked via heating or UV-irradiation to achieve a porous cathode monolith which was beneficial for battery performance (**Graph c**). And he actually succeeded to obtain a monolith of the composite cathode. For novelty and some other reasons, we finally did not move further. The project was suspended.

6.8 Mo_xS_y/C/rGO for NIBs

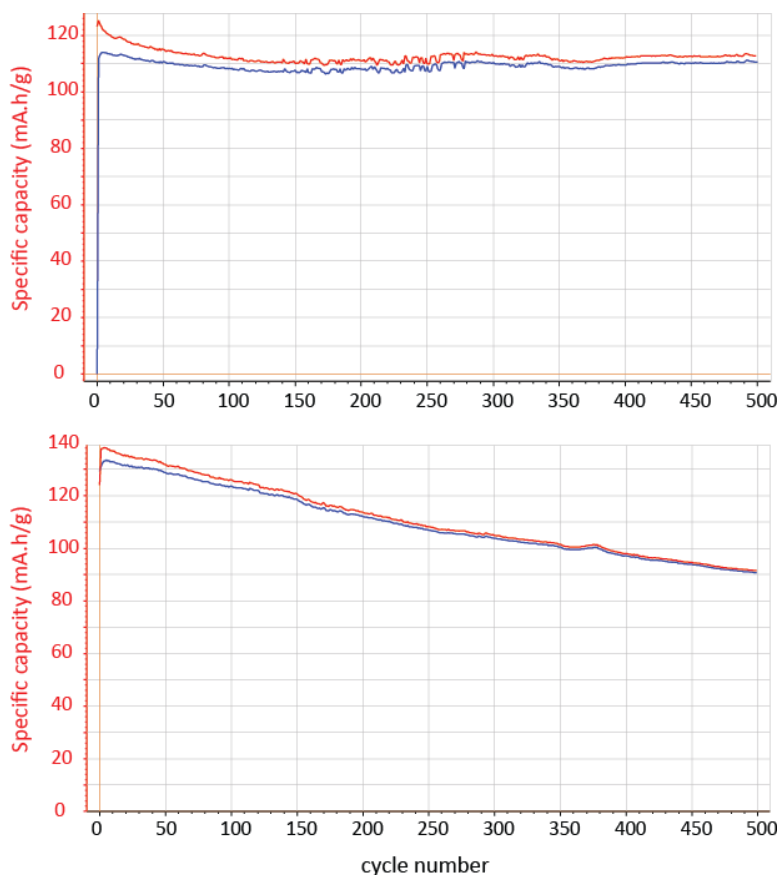


Figure 6.8 Inspired by the design of hierarchical graphene-based composite aerogels, we think it should be feasible to further extend the Mo_xS_y/C/rGO system to Na-ion batteries (or even beyond, *e.g.* Mg- or Al-ion batteries). We obtained some preliminary results as shown above which are reasonably good for Na-ion batteries. Due to the much larger size of Na-ion vs. Li-ion, the capacity and long-term stability for NIBs is not the best yet. We think there is still some room for improvement.

The project is still on-going.

6.9 Alloying-type materials for LIBs & NIBs

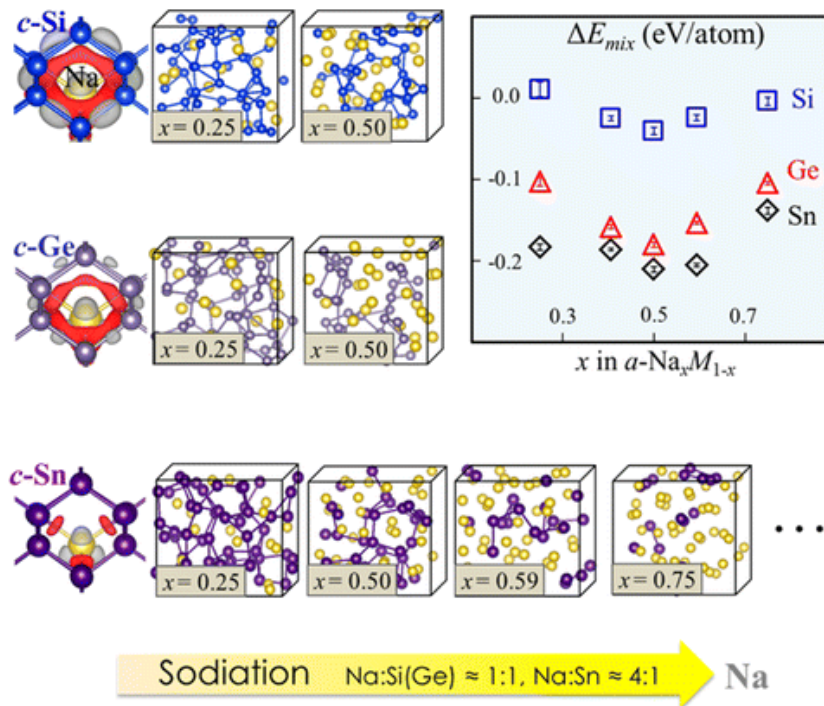


Figure 6.9 Alloying-type materials have received increasing attention owing to their large sodiation capacities, such as NaSi (954 mAh g^{-1}), NaGe (369 mAh g^{-1}), $\text{Na}_{15}\text{Sn}_4$ (847 mAh g^{-1}), $\text{Na}_{15}\text{Pb}_4$ (485 mAh g^{-1}), and Na_3Sb (660 mAh g^{-1}). However, their utilization is still challenging due to the significant volume expansion, which leads to anode degradation and poor capacity retention upon extended cycles. Using similar concept that we developed for the Li-ion batteries, we are now extending to alloying-type electrode materials, e.g. Ge, Sn or Si, as advanced anodes both for Li- and Na-ion batteries. Graph taken from Ref [159].

The project is on-going.

List of the Symbols and Abbreviations

Name	Symbol	Unit
Activity coefficient	a_i	[-]
Avogadro's number	N	[mol ⁻¹]
Boltzmann constant	k	[J/K]
Charge capacity	Q	[Ah]
Current density	j	[A/cm ²]
Electric current	I	[A]
Electrode area	A	[cm ²]
Faraday constant	F	[C/mol]
Gas constant	R	[J/(mol K)]
Gibbs free energy	ΔG	[J/mol]
Mass	m, m_i	[kg]
Number of electrons exchanged	z	[-]
Potential	U	[V]
Power density	P_V	[W/l]
Practical charge density of the active material	Q_V	[Ah/l]
Practical energy density of the active material	W_V	[Wh/l]
Practical specific charge of the active material	q	[Ah/kg]
Practical specific energy of the active material	w	[Wh/kg]
Specific current	i_w	[A/kg]
Specific electrical conductivity	κ_0	[S/cm]
Specific power	p	[W/kg]
Standard Gibbs free energy	ΔG^0	[J/mol]
Standard potential	E^0	[V]
Stoichiometric coefficient	n_i	[-]
Temperature	T	[K]/[°C]
Theoretical cell voltage	$\Delta E^0, U^0$	[V]
Theoretical charge density	$Q_{V, th}$	[Ah/l]
Theoretical energy density	$W_{V, th}$	[Wh/l]
Theoretical specific charge	q_{th}	[Ah/kg]
Theoretical specific energy	w_{th}	[Wh/kg]
Volume	V, V_i	[l]

Abbreviation	Name
2-Py	2-pyrrolidinone
BnOH	Benzyl alcohol
DEC	Diethyl carbonate
DMC	Dimethyl carbonate
DTA	Differential thermal analysis
EC	Ethylene carbonate
EMC	Ethyl methyl carbonate
GIC	Graphite intercalation compound
GO/(rGO)	Graphene oxide/(reduced graphene oxide)
LFP	Lithium iron phosphate, LiFePO_4
NMP	N-Methyl-2-pyrrolidone
PC	Propylene carbonate
PTFE	Polytetrafluoroethylene
PVDF	Polyvinylidene fluoride
SEI	Solid electrolyte interphase/interface
SEM	Scanning electron microscope
SHE	Standard hydrogen electrode
TEM	Transmission electron microscope
XRD	X-ray diffraction
XPS	X-ray photoelectron spectroscopy

Appendix

A. Cell preparation

A.1 The cell instrument

For the electrochemical investigations a cell has to be assembled. The scheme of the cell is given in the Figure A.1, which is mainly made of titanium. The counter electrode was brought onto a titanium-made cylinder (8) and pressed with a spring (5) against the working electrode coated onto a titanium current collector (10). A separator soaked with the electrolyte was put between the two electrodes. The cell assembling was set up in a glove box under argon atmosphere ($\text{H}_2\text{O} < 1 \text{ ppm}$, $\text{O}_2 = 0.1 \text{ ppm}$).

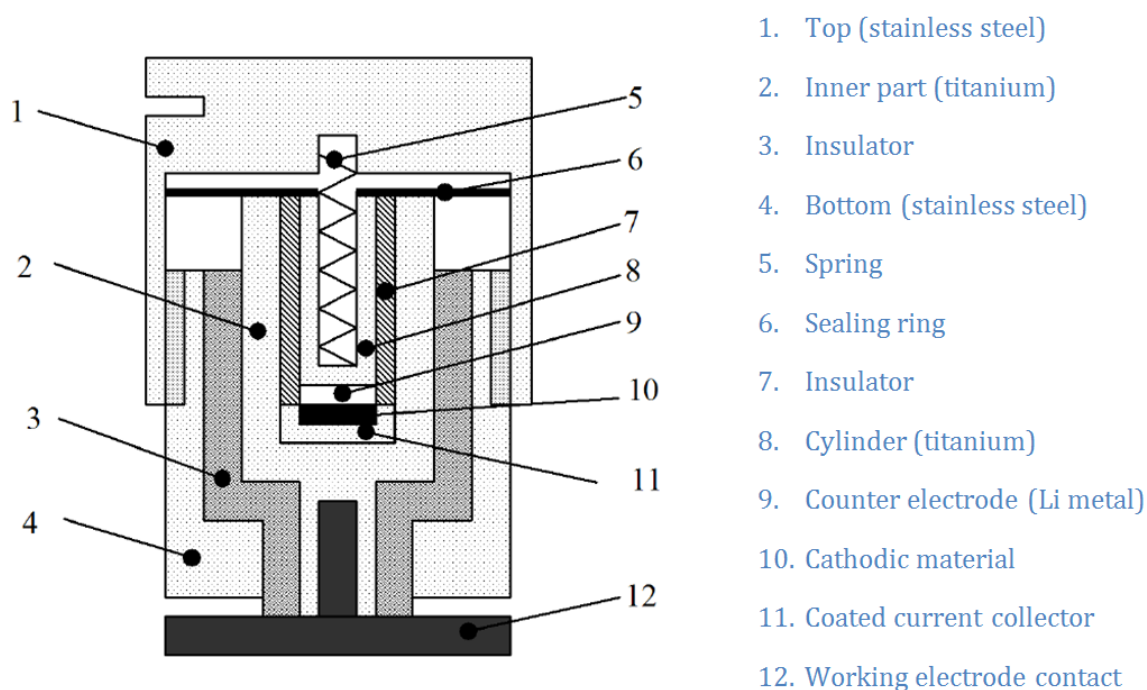


Figure A.1 Scheme of the electrochemical cell used in the experiments.

A.2 Electrode preparation

Working electrode. Since we were working on the oxides whose electronic conductivity is not high enough, a component that promotes the conductivity of the electrode had to be added. Super P[®] (provided by TIMCAL) is conductive carbon black used as conductive additive in Li-ion batteries. In addition, to hold the active material and the carbon together, a binder, Polyvinylidene Fluoride (PVDF, ALDRICH, average $M_w \sim 180,000 \text{ GPC}$) was used. To obtain a good mixing, the three

components (active material, carbon and binder) were suspended in an organic solvent, N-Methyl-2-pyrrolidone (NMP, Alfa-Aesar, 99.5 %).

Generally, 80 wt% of active materials, 10 wt% of carbon black and 10 wt% of PVDF were mixed and ground well using a mortar and pestle, and then the mix was transferred into a glass vial (10 ml capacity). The amount of NMP, depending on the quantities of mix, was added into the bottle to obtain the form of slurry or concentrated suspension. To better dissolve PVDF in NMP and mix the components, the materials were mechanically stirred and ultrasonicated for ca. 10 min at 40 °C. Generally, 3-10 mg of electrode materials were dropped onto the current collector (Figure A.2), followed by heat treatment in order to vaporize NMP and any H₂O absorbed on/in the materials. Usually, the heat treatment was conducted at 100 °C overnight or even longer. The weight of electrode materials were measured and multiplied by 80% to only refer to the active materials. After that, the current collector was sent into the glove box, and assembled into the cell.

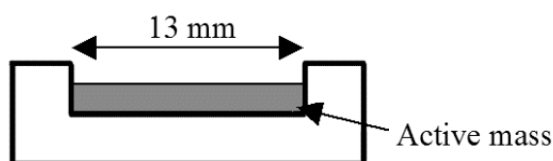


Figure A.2 Scheme of the current collector filled with active mass, with surface area = 1.3 cm².

Counter electrode All measurements through this work were performed using metallic lithium (ribbon, 0.75 mm thick, Aldrich) as the counter electrode. Because the potential of metallic lithium is nearly constant at moderate or low current densities, the counter electrode was also used as the reference electrode.

The electrolyte The electrolyte was used as received and always stored in the glove box. In this study, all measurements were performed with a mixture of ethylene carbonate and dimethyl carbonate 1:1 wt%, with 1 M LiPF₆.

The cells were discharged and charged at various current rates and different voltage windows.

B. Characterization of electrochemical cells

There are several criteria to evaluate the performance of electrochemical cells. A distinction must be made between the theoretical values and the practical values. Theoretical values are calculated from the thermodynamics of the electrochemical cell reaction. Practical values are related to the total mass of the complete battery, including the mass of the electrolyte, the separators, the current collectors, the terminals and the cell housing. In this work the specific charge always refers to the weight of the active component only.

B.1 Cell voltage

The cell voltage can be calculated from the Gibbs free energy of the corresponding chemical reaction:

$$U^0 = \Delta E^0 = \frac{-\Delta G^0}{zF} \quad [V]$$

B.2 Current density

The current density j is calculated by dividing the total current I flowing through an electrode by the electrode area A . The normal case is that the geometrical area is used:

$$j = \frac{I}{A} \quad [A/cm^2]$$

B.3 Charge capacity

The charge capacity Q is the total amount of charge obtainable from a cell:

$$Q = \int_{t_1}^{t_2} I(t) dt \quad [Ah]$$

B.4 Theoretical specific charge and theoretical charge density

The theoretical specific charge q_{th} is the amount of charge per kg of reactants m_i , and it can be calculated from the stoichiometry of the overall cell reaction:

$$q_{th} = \frac{zF}{\sum_i m_i} \quad [Ah/kg]$$

The charge divided by the volume of reactants V_i leads to the theoretical charge density $Q_{v,th}$:

$$Q_{v,th} = \frac{zF}{\sum_i V_i} \quad [Ah/l]$$

B.5 Practical specific charge and practical charge density

The practical specific charge q , or the practical charge density Q_v , is the total charge obtainable from a practical cell, divided by the total mass or the volume of the cell, respectively:

$$q = \int_{t_1}^{t_2} \frac{I(t)}{m} dt \quad [Ah/kg]$$

$$Q_v = \int_{t_1}^{t_2} \frac{I(t)}{V} dt \quad [Ah/l]$$

Another quantity often used is the so-called irreversible specific charge. It is defined as the difference between the specific charge spent on charging and the one obtained on discharging a cell. To obtain a normalized value this difference is then divided by the specific charge spent on charging.

B.6 Theoretical specific energy and theoretical energy density

The theoretical specific energy w_{th} , or the theoretical energy density $W_{V,th}$, can be calculated from the Gibbs energy change of the electrochemical cell reaction,

$$w_{th} = \frac{zF\Delta E^0}{\sum_i m_i} \quad [Wh/kg]$$

$$W_{V,th} = \frac{zF\Delta E^0}{\sum_i V_i} \quad [Wh/l]$$

divided by the sum of the stoichiometric masses of the reactants or by their volumes, respectively.

B.7 Practical specific energy and practical energy density

The practical specific energy w , or the practical energy density W_V , is the total electrical energy obtainable from a practical cell divided by the mass or the volume of the cell, respectively:

$$w = \int_{t_1}^{t_2} \frac{I\Delta E}{m} dt \quad [Wh/kg]$$

$$W_V = \int_{t_1}^{t_2} \frac{I\Delta E}{V} dt \quad [Wh/l]$$

B.8 Specific power and power density

The specific power p is the capability to deliver power per mass. The specific power of a cell depends on the discharge current and decreases during discharge. The power density P_V is the power divided by the volume of the cell. Again, one distinguishes between theoretical and practical values:

$$p = \frac{I\Delta E}{\sum_i m_i} \quad [W/kg]$$

$$P_V = \frac{I\Delta E}{\sum_i V_i} \quad [W/l]$$

In battery technology the term c-rate ($C/\Delta t$) is often used. C means a nominal or, sometimes, a theoretical charge capacity of a cell or battery in [Ah]. Therefore, C/2, for example, means a current theoretically allowing a full discharge in two hours.

C. Supporting information for Chapter 2

Table C.1 The Rietveld refinement report of α -LiFePO₄ which was performed using the program GSAS. The profile type used for fitting is Pseudo-Voigt function. Spherical Harmonics was performed for the preferred orientation correction. Surface roughness correction was performed based on Suortti model.

Sample ID	Density (g/cm ³)	Space group	Lattice parameters (Å)	Atomic parameters					Refinement parameters
				Atom	<i>x/a</i>	<i>y/b</i>	<i>z/c</i>	<i>Uiso</i>	
α -LiFePO ₄	3.602	<i>Pnma</i>	<i>a</i> = 10.3221(1)	Li	0.0	0.0	0.0	0.0142	<i>R</i> _{wp} = 9.54 χ^2 = 1.378
			<i>b</i> = 6.0030(1)	Fe	0.282091	0.25	0.975002	0.0023	
			<i>c</i> = 4.6941(1)	P	0.095276	0.25	0.418310	0.0009	
			$\alpha = \beta = \gamma = 90^\circ$	O1	0.097963	0.25	0.739999	0.0022	
			<i>V</i> = 290.876(4) (Å ³)	O2	0.456515	0.25	0.207699	0.0019	
				O3	0.166463	0.048019	0.285371	0.0015	

Table C.2 The Rietveld refinement report of β -LiFePO₄ using the program as above.

Sample ID	Density (g/cm ³)	Space group	Lattice parameters (Å)	Atomic parameters					Refinement parameters
				Atom	<i>x/a</i>	<i>y/b</i>	<i>z/c</i>	<i>Uiso</i>	
β -LiFePO ₄	3.731	<i>Cmcm</i>	<i>a</i> = 5.4948(2)	Li	0.0	0.663491	0.25	0.0038	<i>R</i> _{wp} = 10.62 χ^2 = 1.809
			<i>b</i> = 8.2335(2)	Fe	0.0	0.0	0.0	0.0067	
			<i>c</i> = 6.2074 (2)	P	0.0	0.348972	0.25	0.0027	
			$\alpha = \beta = \gamma = 90^\circ$	O1	0.0	0.243875	0.051271	0.0098	
			<i>V</i> = 280.83(1) (Å ³)	O2	0.203978	0.467170	0.25	0.0003	

Table C.3 Lattice parameters (Å), the shortest Li-Li distances (Å), the mean values of the bond lengths Fe-O and P-O, energy differences (kJ/mol) and cell volume differences (Å³) of the two orthorhombic structures, α (*Pnma*) and β (*Cmcm*). Both structures contain 4 formula units.

		GGA	GGA-D	LSDA+U
α	<i>a, b, c</i>	9.954, 5.873, 4.688	9.806, 5.822, 4.680	10.396, 6.167, 4.739
	<i>d</i> (Li-Li)	2.936	2.911	3.084
	< <i>d</i> (Fe-O)>	2.057	2.036	2.193
	< <i>d</i> (P-O)>	1.544	1.541	1.5364
β	<i>a, b, c</i>	5.300, 8.189, 6.170	5.226, 8.037, 6.200	5.611, 8.363, 6.269
	<i>d</i> (Li-Li)	4.201, 4.253	4.164, 4.366	4.413, 4.236
	< <i>d</i> (Fe-O)>	2.070	2.044	2.181
	< <i>d</i> (P-O)>	1.542	1.535	1.534
	$\Delta E_{\beta\alpha}$	18.397	10.703	10.662
	$\Delta V_{\beta\alpha}$	-6.198	-6.743	-9.644

Table C.4 The Wyckoff positions of the orthorhombic structure, symmetry group *Pnma*. Z = 4. The lattice parameters 10.396 Å, 6.167 Å, 4.739 Å, calculated at LSDA+U level.

Species	x	y	z	Site	Symmetry
Li	0	0	0	4a	-1
Fe	0.2162	0.25	0.5323	4c	.m.
P	0.4041	0.25	0.0788	4c	.m.
O	0.4010	0.25	0.7590	4c	.m.
O	0.0414	0.25	0.3041	4c	.m.
O	0.3346	0.0515	0.2088	8d	1

Table C.5 The Wyckoff positions of the orthorhombic structure, symmetry group *Cmcm*. Z = 4. The lattice parameters are 5.611 Å, 8.363 Å, 6.269 Å, calculated at LSDA+U level.

Species	x	y	z	Site	Symmetry
Li	0	0.6704	0.25	4c	<i>m2m</i>
Fe	0	0	0	4a	<i>2/m..</i>
P	0	0.3466	0.25	4c	<i>m2m</i>
O	0	0.2422	0.0512	8f	<i>m..</i>
O	0.2205	0.4575	0.25	8g	<i>..m</i>

Table C.6 The Wyckoff positions of FePO₄ in the two orthorhombic structures, calculated at LSDA+U level. Z = 4 in both symmetries.

Species	x	y	z	Site	Symmetry
<i>Pnma</i>, a = 9.912 Å, b = 6.189 Å, c = 4.961 Å, V_c = 304.322 Å³					
Fe	0.276	0.25	0.519	4c	.m.
P	0.105	0.25	0.068	4c	.m.
O	0.131	0.25	0.768	4c	.m.
O	0.455	0.25	0.381	4c	.m.
O	0.175	0.0584	0.212	8d	1
<i>Cmcm</i>, a = 5.302 Å, b = 7.914 Å, c = 6.645 Å, V_c = 278.832 Å³					
Fe	0	0	0	4c	<i>2/m..</i>
P	0	0.3411	0.25	4c	<i>m2m</i>
O	0	0.2324	0.0623	8f	<i>m..</i>
O	0.2386	0.4537	0.25	8g	<i>..m</i>

Table C.7 The Wyckoff positions of the orthorhombic structure, symmetry group $Cmcm$, modelled starting with the absorption of one mole of Li in the orthorhombic structure of $FePO_4$, same symmetry group. The structure data calculated at DFT-D level and LSDA+U level ($Z = 4$), respectively.

Species	x	y	z	Site	Symmetry
Calculated DFT-D level: a = 5.096 Å, b = 8.363 Å, c = 6.771 Å, $V_c = 288.568 \text{ Å}^3$					
Li	0	0	0	4a	2/m..
Fe	0	0.5	0	4b	2/m..
P	0	0.1863	0.25	4c	m2m
O	0	0.2764	0.0612	8f	m..
O	0.2401	0.0635	0.25	8g	..m
Calculated LSDA+U level (Z = 4): a = 5.527 Å, b = 8.471 Å, c = 7.193 Å, $V_c = 336.733 \text{ Å}^3$					
Li	0	0	0	4a	2/m..
Fe	0	0.5	0	4b	2/m..
P	0	0.1864	0.25	4c	m2m
O	0	0.2825	0.0729	8f	m..
O	0.2188	0.0722	0.25	8g	..m

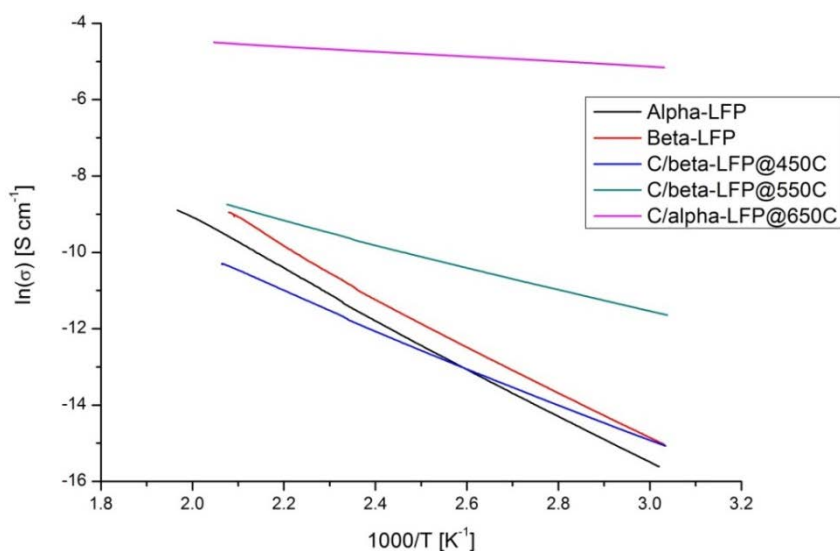


Figure C.1 Electronic conductivity results for as-prepared α - $LiFePO_4$ and carbon coated α - $LiFePO_4$ annealed at 650 °C, pristine β - $LiFePO_4$ and carbon coated β - $LiFePO_4$ treated at 450 °C, and phase-transformed carbon coated β - $LiFePO_4$ fired at 550 °C, respectively, all of which were measured by two-point *d.c.* method.

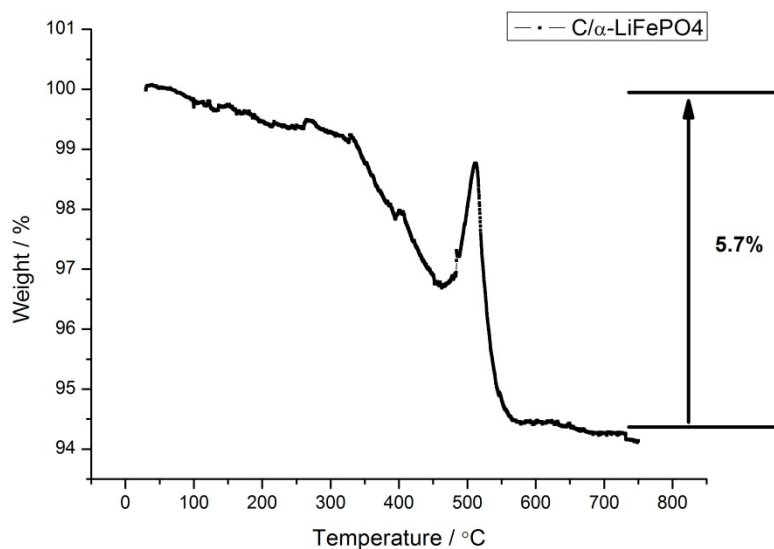


Figure C.2 A typical thermal gravimetric analysis (TGA) curve of LiFePO₄ heated in air. TGA is commonly used for evaluating the carbon content according to equation $\text{LiFePO}_4 + (1/4)\text{O}_2 \rightarrow (1/3)\text{Li}_3\text{Fe}_2(\text{PO}_4)_3 + (1/6)\text{Fe}_2\text{O}_3$. As a result of this oxidation, weight loss of 5.7% was calculated as carbon content of 10.2%.

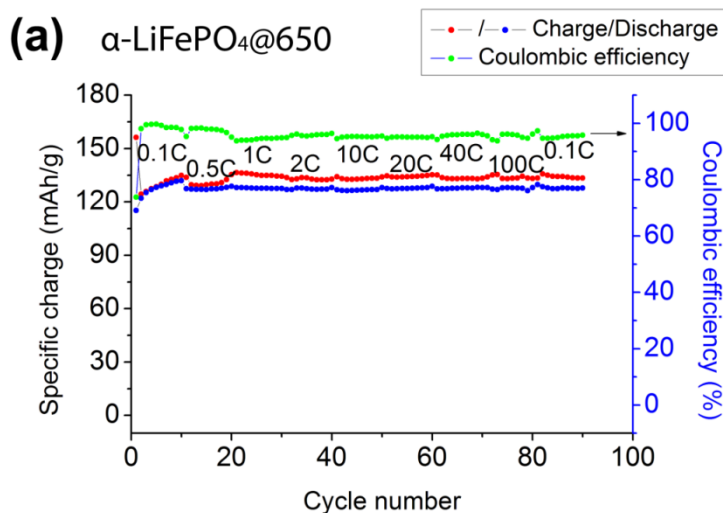
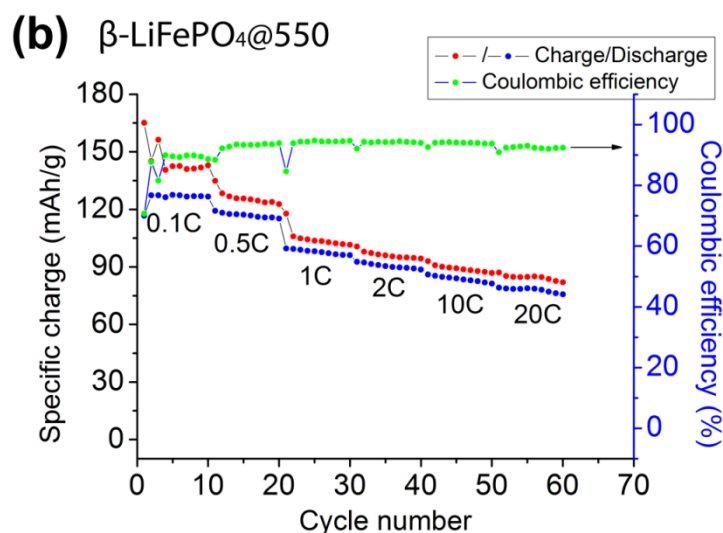


Figure C.3 To promote complete charge/discharge at the respective potential limits, a potentiostatic step was included until the specific current decreased to 0.1C. After including the potentiostatic step, the coulombic efficiency for α-LiFePO₄@650 is ~96% and it can always reversibly deliver ~135 mAh/g as it does at 0.1 C (a); The coulombic efficiency for β-LiFePO₄@550 is ~94%, but its specific charge cannot be fully recovered to the value obtained at 0.1C. Its capacity gradually decreased upon higher current rates (b).



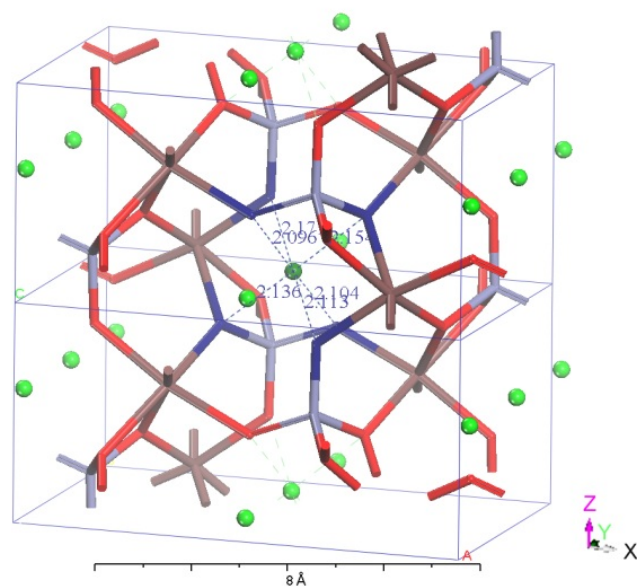


Figure C.4 A view of the local coordination of the Li atom in the *Pnma* structure at thermal equilibrium, $T = 10$ K. The nearest neighbour oxygen atoms to Li are coloured in blue.

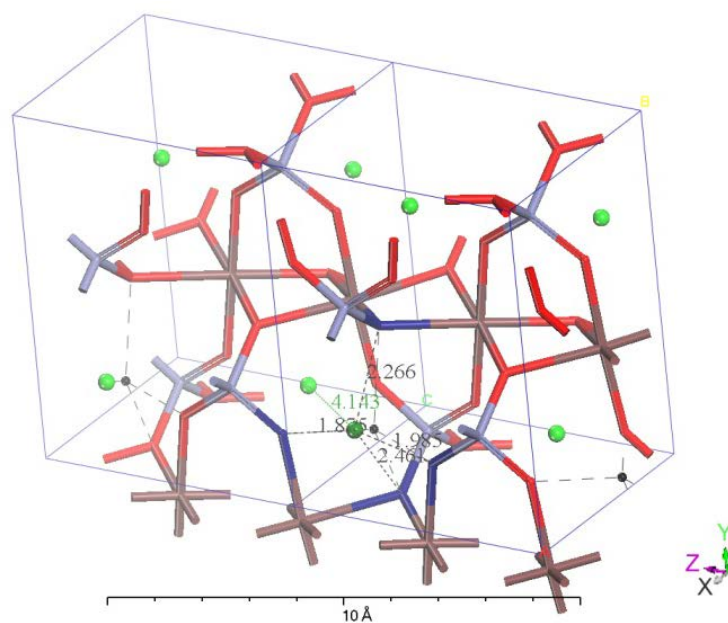


Figure C.5 A view of the local coordination of the Li atom in the *Cmc* structure at thermal equilibrium, $T = 10$ K. The nearest neighbour oxygen atoms to Li are coloured in blue.

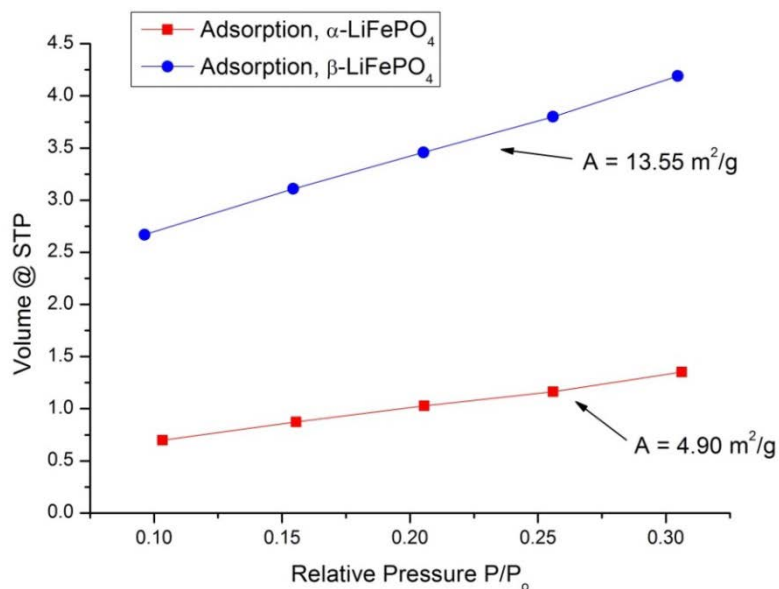


Figure C.6 Specific surface area determined by gas adsorption, $A = 4.90 \text{ m}^2/\text{g}$ for $\alpha\text{-LiFePO}_4$ and $A = 13.55 \text{ m}^2/\text{g}$ for $\beta\text{-LiFePO}_4$.

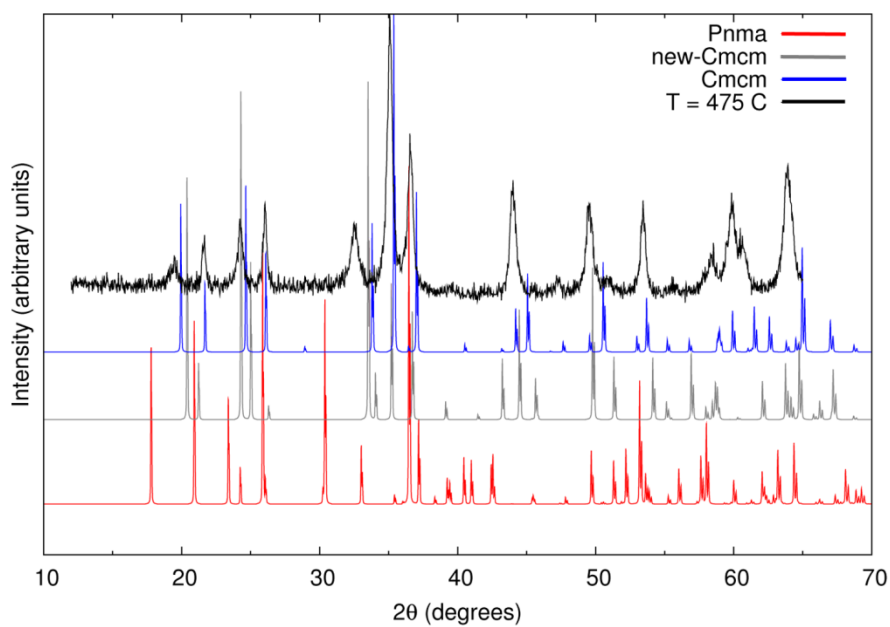


Figure C.7 The calculated XRD patterns of the α ($Pnma$), β ($Cmcm$) and the new $Cmcm$ structures. For comparison the experimental XRD pattern of the β structure at $T = 475 \text{ }^\circ\text{C}$.

D. Supporting information for Chapter 3

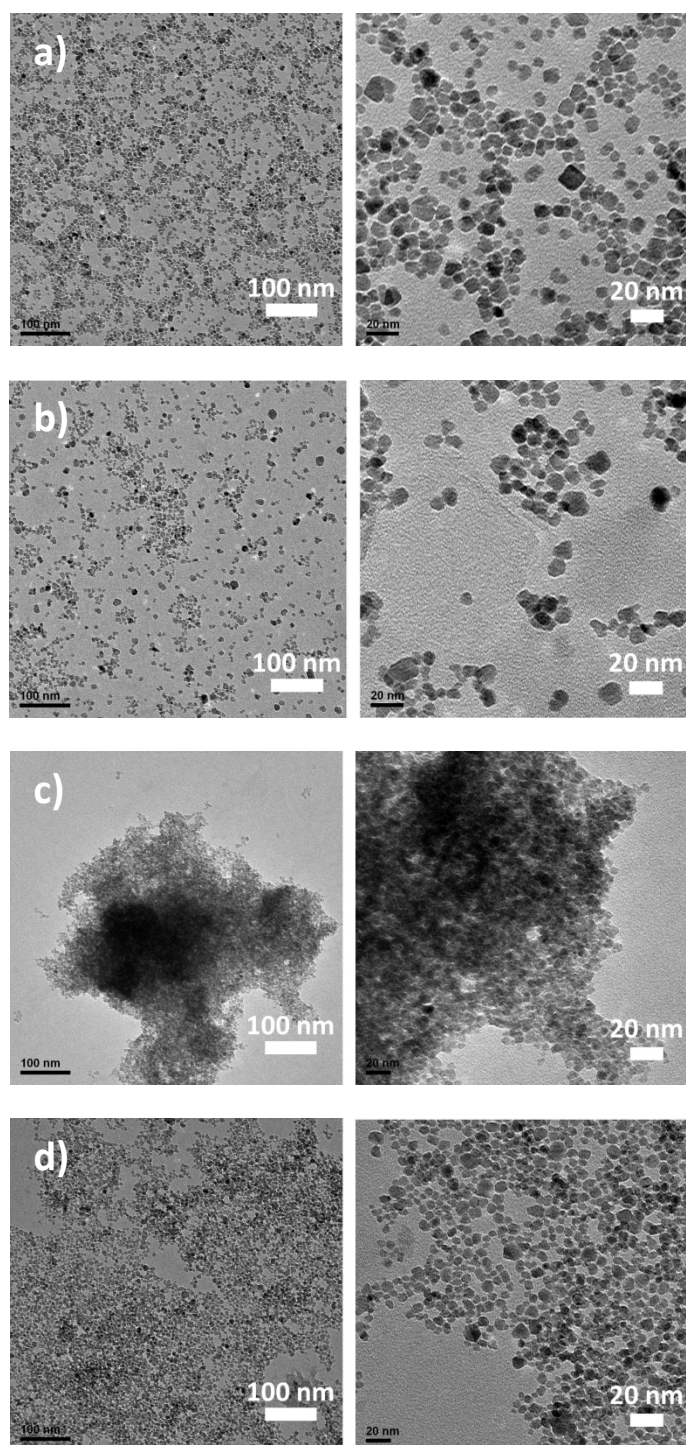


Figure D.1 TEM images of the ferrite nanoparticles (NPs) at low and higher magnifications: a) Fe_3O_4 , b) CoFe_2O_4 , c) MnFe_2O_4 and d) NiFe_2O_4 .

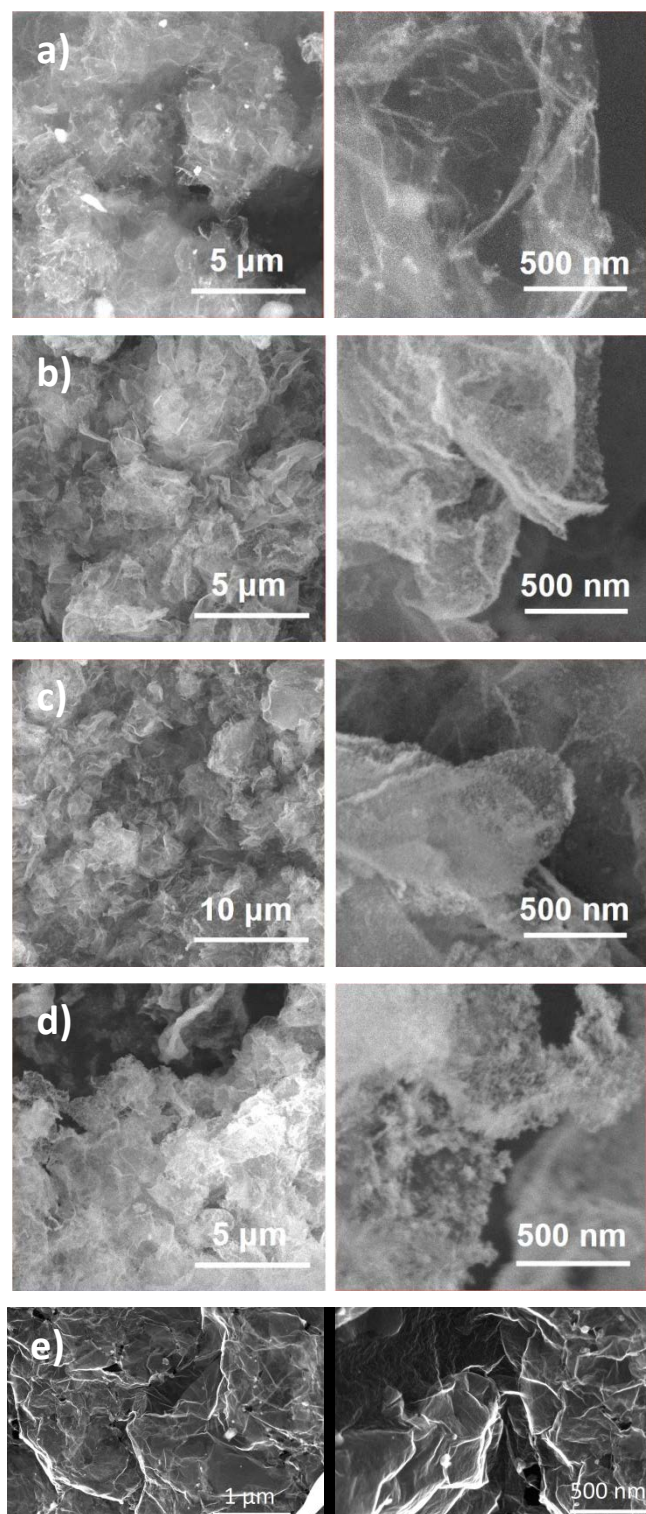


Figure D.2 SEM images of spinel-type ferrite/rGO composite aerogels at low and higher magnifications: a) Fe₃O₄/rGO, b) CoFe₂O₄/rGO, c) MnFe₂O₄/rGO, d) NiFe₂O₄/rGO and e) pure rGO aerogel without NPs.

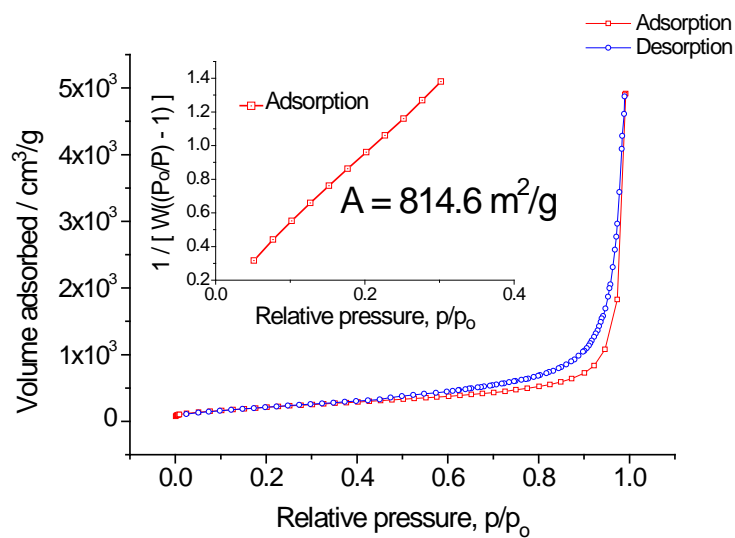


Figure D.3 N₂ adsorption/desorption isotherm of the rGO aerogel with specific surface area of 814.6 m²/g.

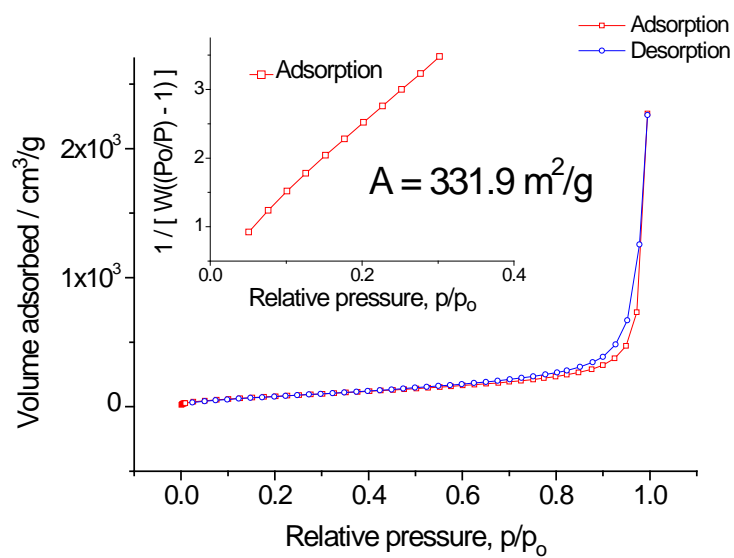


Figure D.4 N₂ adsorption/desorption isotherm of the Co₃O₄/rGO aerogel with specific surface area of 331.9 m²/g.

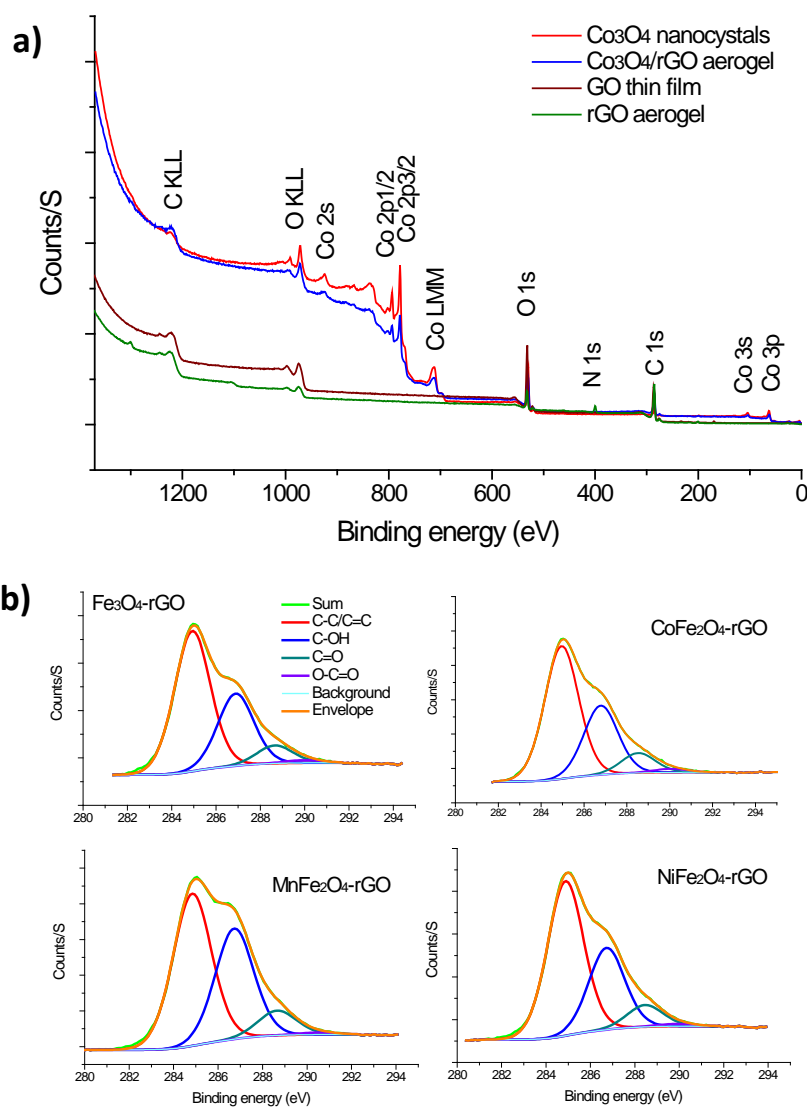


Figure D.5 a) XPS survey spectra of Co₃O₄ nanocrystals, Co₃O₄/rGO, GO thin film and rGO aerogel. b) High-resolution XPS C 1s spectra for Fe₃O₄/rGO, CoFe₂O₄/rGO, MnFe₂O₄/rGO and NiFe₂O₄/rGO composite aerogels.

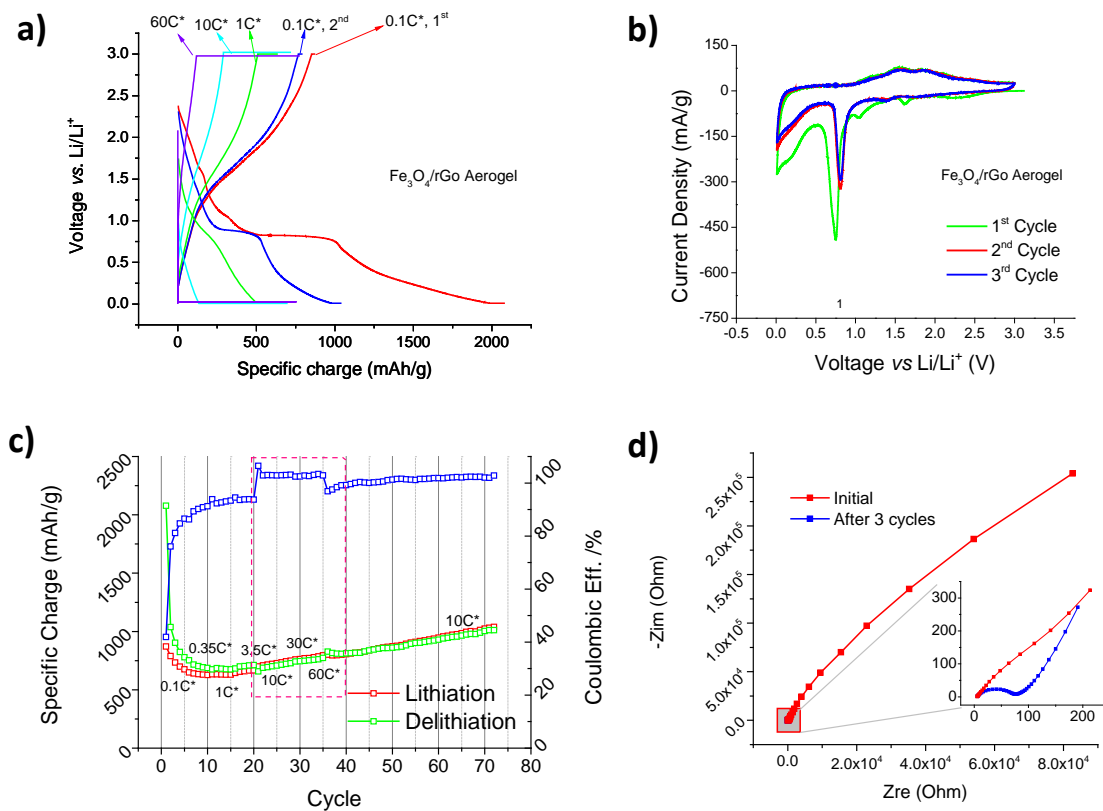


Figure D.6 Electrochemical tests for the $\text{Fe}_3\text{O}_4/\text{rGO}$ composite aerogel: a) constant current + constant voltage (CC+CV) cycling profiles at different current rates; b) the first three cyclic voltammetry scans at 0.05 mV/s ; c) cycling performance under CC+CV conditions; d) EIS spectra of the composite aerogel before and after 3 cycles at 3V vs. Li^+/Li .

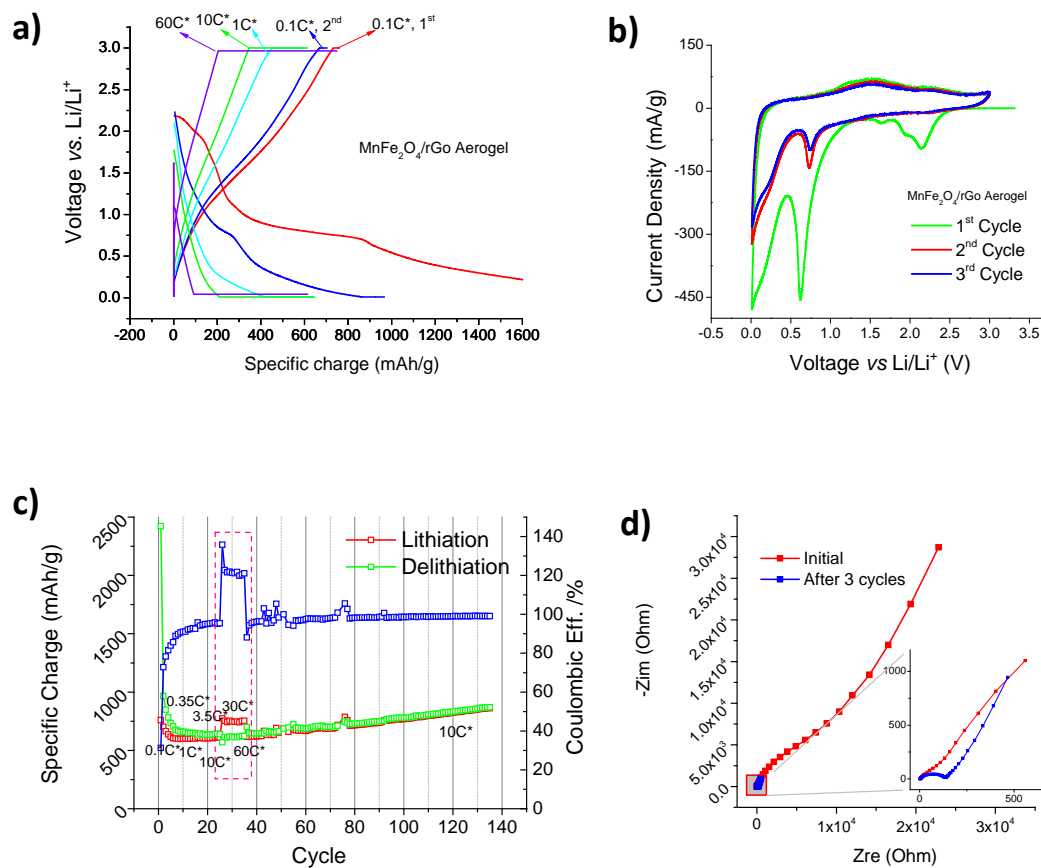


Figure D.7 Electrochemical tests for the MnFe₂O₄/rGO composite aerogel: a) constant current + constant voltage (CC+CV) cycling profiles at different current rates; b) the first three cyclic voltammetry scans at 0.05 mV/s; c) cycling performance under CC+CV conditions; d) EIS spectra of the composite aerogel before and after 3 cycles at 3V vs. Li⁺/Li.

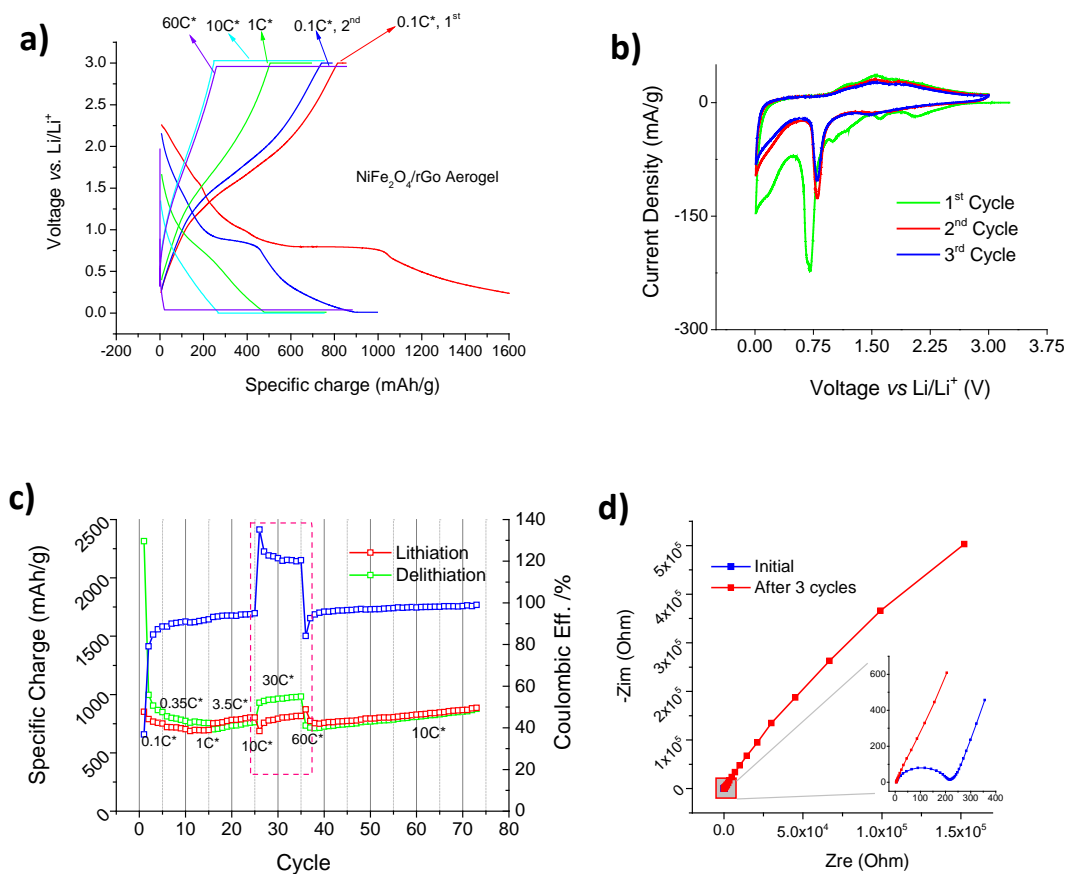


Figure D.8 Electrochemical tests for the NiFe₂O₄/rGO composite aerogel: a) constant current + constant voltage (CC+CV) cycling profiles at different current rates; b) the first three cyclic voltammetry scans at 0.05 mV/s; c) cycling performance under CC+CV conditions; d) EIS spectra of the composite aerogel before and after 3 cycles at 3 V vs. Li⁺/Li.

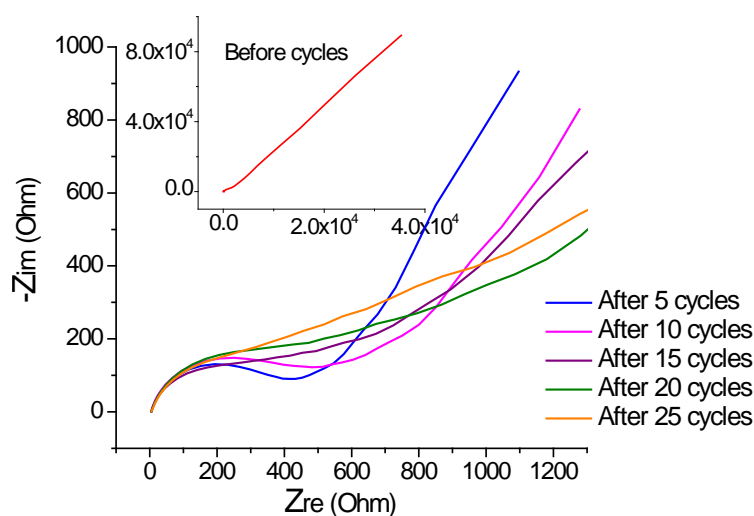


Figure D.9 EIS of the Co₃O₄/rGO composite aerogel for the pristine electrode (inset) and after different numbers of cycles measured at 3V vs. Li⁺/Li after 24h of relaxation. Inset: Small semicircle showing that the aerogel composite cannot store any lithium before activation in the first cycle. After 5 cycles, well defined semicircle and Warburg impedance indicate good activation of the composite aerogel. After higher cycle numbers, the resistance increases.

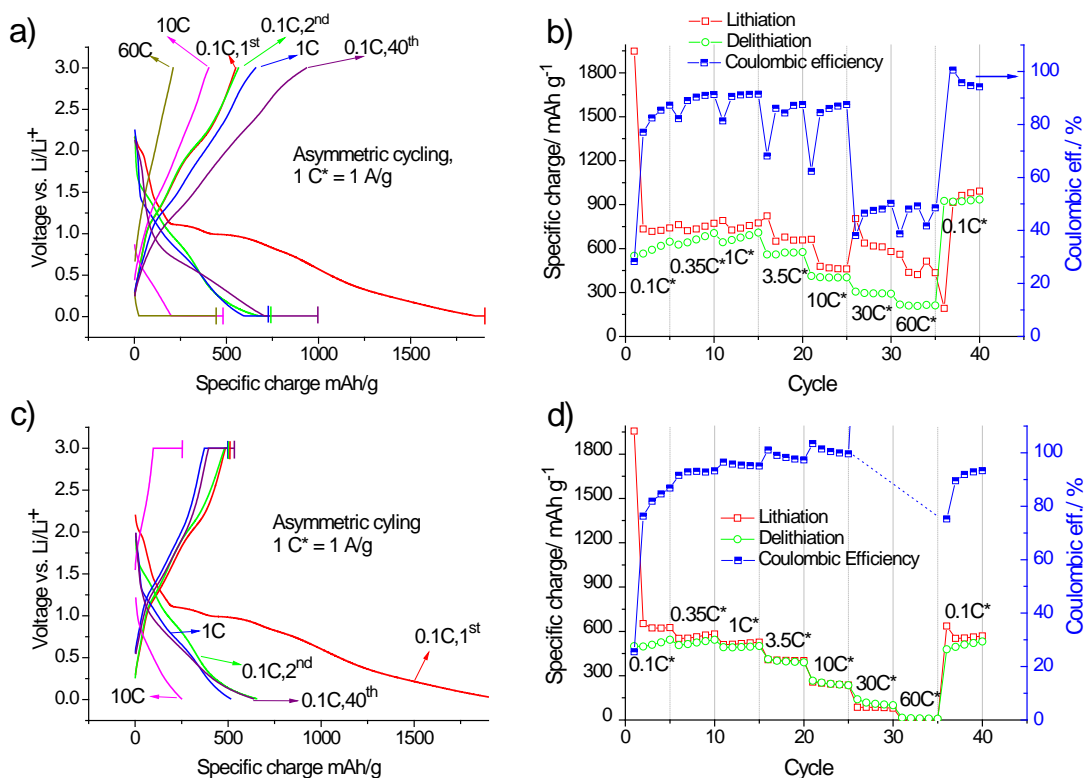


Figure D.10 Galvanostatic (constant current) cycling of the $\text{Co}_3\text{O}_4/\text{rGO}$ aerogel with potential limitation (constant voltage) a,b) on discharges or c,d) on charges until the specific current reaches the equivalent to 0.05 C rate. a, b) When the $\text{Co}_3\text{O}_4/\text{rGO}$ aerogel discharges (lithiation) at high current rates, e.g., at 60 C, it delivers 446 mAh g^{-1} (merely 24 mAh g^{-1} contributed from the galvanostatic part), while it can still be charged galvanostatically (delithiation) with 211 mAh g^{-1} . c, d) The $\text{Co}_3\text{O}_4/\text{rGO}$ aerogel discharges slower. At 60 C the overpotential of the $\text{Co}_3\text{O}_4/\text{rGO}$ aerogel quickly reaches the cutoff potential, but barely on the galvanostatic part during discharge. At current rates $\leq 10\text{ C}$ and under GCPL conditions, the electrode's Coulombic efficiency is approaching 100%. Obviously, the Li-ion de-/insertion kinetics are asymmetric: The kinetics of delithiation from the porous composite electrode is much quicker than that of lithiation.

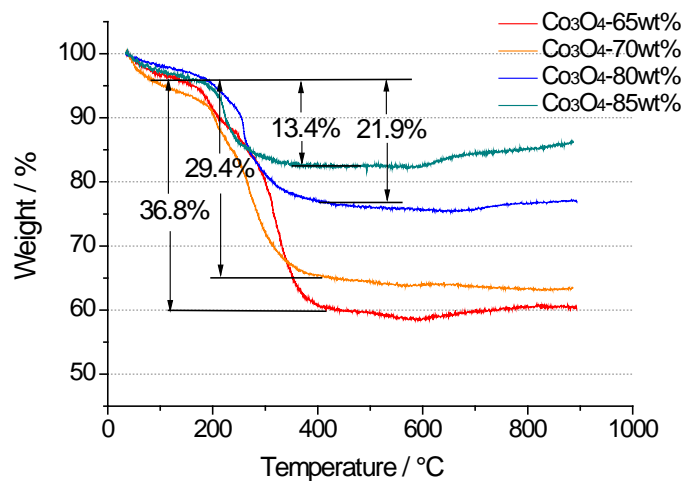


Figure D.11 Thermal gravimetric analysis (TGA) curves of the $\text{Co}_3\text{O}_4/\text{rGO}$ composite aerogels giving information about the mass loading of the Co_3O_4 nanocrystals.

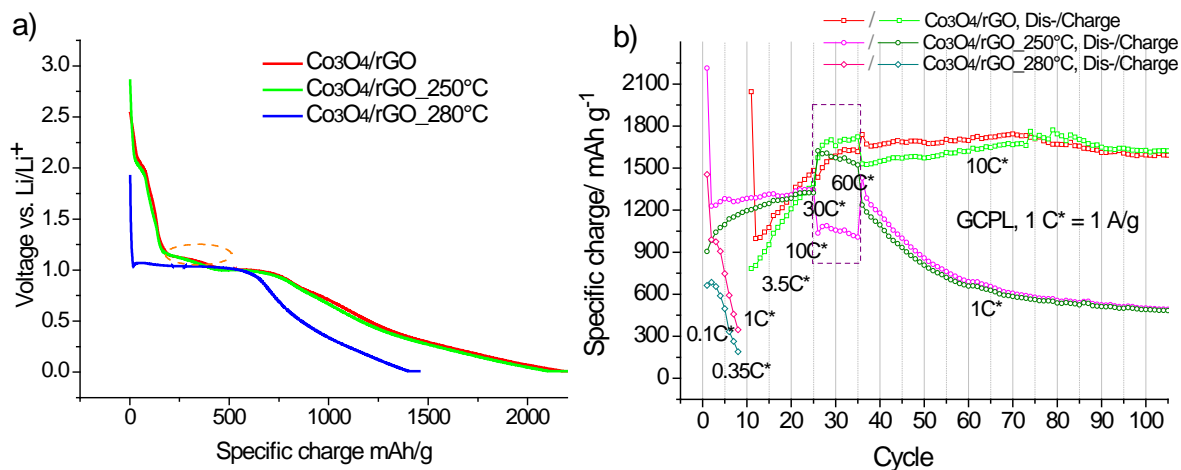


Figure D.12 Constant current + constant voltage (CC+CV) cycling profiles for the $\text{Co}_3\text{O}_4/\text{rGO}$ composite aerogels that were thermally treated at different temperatures under N_2 plus 5 vol% H_2 atmosphere for 6 hours. a) The plateau at ~ 1.1 V disappears after the heat treatment at 280°C , which indicates reduction of graphene oxide. b) However, the cyclability of the $\text{Co}_3\text{O}_4/\text{rGO}$ aerogel is lowered after the heat treatment.

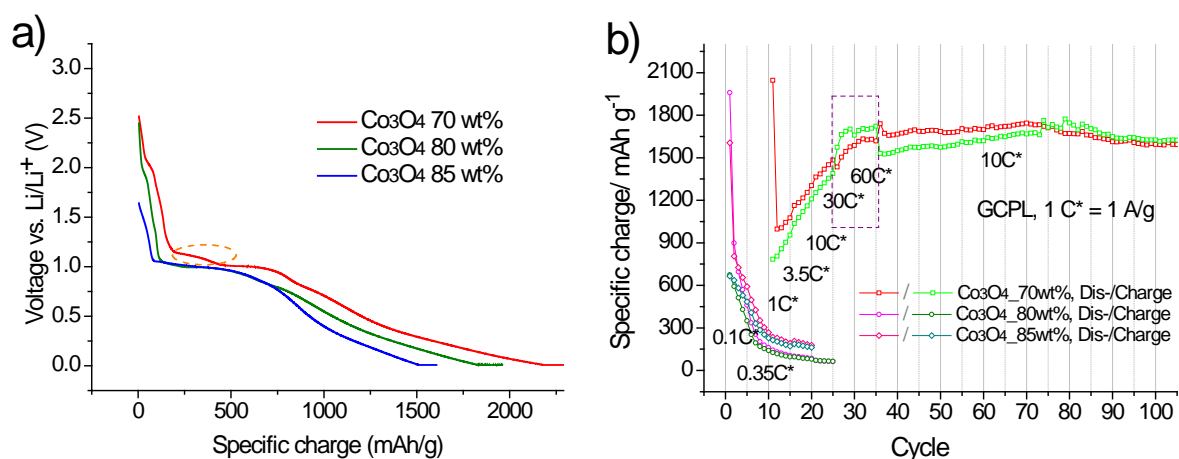


Figure D.13 Constant current + constant voltage (CC+CV) cycling profiles for the $\text{Co}_3\text{O}_4/\text{rGO}$ composite aerogels with different loadings of Co_3O_4 NCs. a) The plateau at ~ 1.1 V is less pronounced with less loading of the GO. b) However, with less amount of GO, the cyclability of the $\text{Co}_3\text{O}_4/\text{rGO}$ composite aerogel drops significantly. Obviously, it requires an optimum amount of graphene oxide to create hierarchical porosity and to provide the mechanical stability of the composite aerogel.

References

1. Paris Climate Change Conference, United Nations, (2015).
2. Murray, J. & King, D. Climate policy: Oil's tipping point has passed. *Nature* **481**, 433-435 (2012).
3. Whittingham, M.S. Materials Challenges Facing Electrical Energy Storage. *MRS Bull.* **33**, 411-419 (2008).
4. Goodenough, J.B. & Kim, Y. Challenges for Rechargeable Li Batteries. *Chem. Mater.* **22**, 587-603 (2010).
5. Tarascon, J.M. & Armand, M. Issues and Challenges Facing Rechargeable Lithium Batteries. *Nature* **414**, 359-367 (2001).
6. Arico, A.S., Bruce, P., Scrosati, B., Tarascon, J.-M. & van Schalkwijk, W. Nanostructured materials for advanced energy conversion and storage devices. *Nat. Mater.* **4**, 366-377 (2005).
7. Bruce, P.G., Scrosati, B. & Tarascon, J.-M. Nanomaterials for Rechargeable Lithium Batteries. *Angew. Chem. Int. Ed.* **47**, 2930-2946 (2008).
8. Palacin, M.R. Recent advances in rechargeable battery materials: a chemist's perspective. *Chem. Soc. Rev.* **38**, 2565-2575 (2009).
9. WHITTINGHAM, M.S. Electrical Energy Storage and Intercalation Chemistry. *Science* **192**, 1126-1127 (1976).
10. Whittingham, M.S.C.b.U.P.
11. Murphy, D.W., Di Salvo, F.J., Carides, J.N. & Waszczak, J.V. Topochemical reactions of rutile related structures with lithium. *Mater. Res. Bull.* **13**, 1395-1402 (1978).
12. Lazzari, M. & Scrosati, B. A Cyclable Lithium Organic Electrolyte Cell Based on Two Intercalation Electrodes. *J. Electrochem. Soc.* **127**, 773-774 (1980).
13. Mizushima, K., Jones, P.C., Wiseman, P.J. & Goodenough, J.B. Li_xCoO_2 ($0 < x < 1$): A new cathode material for batteries of high energy density. *Mater. Res. Bull.* **15**, 783-789 (1980).
14. Nagaura, T.T., K. Lithium ion rechargeable battery. *Prog. Batteries Solar Cells* **9**, 209 (1990).
15. Armand, M. & Tarascon, J.M. Building better batteries. *Nature* **451**, 652-657 (2008).
16. Coluccia, M., PhD Dissertation, ETH Zurich No. 13751 (2000).
17. Pioletto Pioletto, A., PhD Dissertation, ETH Zurich No. 15659 (2004).
18. Garcia, B., Lavallée, S., Perron, G., Michot, C. & Armand, M. Room temperature molten salts as lithium battery electrolyte. *Electrochim. Acta* **49**, 4583-4588 (2004).
19. Fong, R., von Sacken, U. & Dahn, J.R. Studies of Lithium Intercalation into Carbons Using Nonaqueous Electrochemical Cells. *J. Electrochem. Soc.* **137**, 2009-2013 (1990).
20. Yazami, R. Surface chemistry and lithium storage capability of the graphite-lithium electrode. *Electrochim. Acta* **45**, 87-97 (1999).
21. Sloop, S.E., Pugh, J.K., Wang, S., Kerr, J.B. & Kinoshita, K. Chemical Reactivity of PF_5 and LiPF_6 in Ethylene Carbonate/Dimethyl Carbonate Solutions. *Electrochem. Solid-State Lett.* **4**, A42-A44 (2001).
22. Lewandowski, A. & Świdarska-Mocek, A. Ionic liquids as electrolytes for Li-ion batteries - An overview of electrochemical studies. *J. Power Sources* **194**, 601-609 (2009).
23. Stassen, I. & Hambitzer, G. Metallic lithium batteries for high power applications. *J. Power Sources* **105**, 145-150 (2002).
24. Nishimoto, A., Watanabe, M., Ikeda, Y. & Kohjiya, S. High ionic conductivity of new polymer electrolytes based on high molecular weight polyether comb polymers. *Electrochim. Acta* **43**, 1177-1184 (1998).
25. Pradel, A. & Ribes, M. Lithium chalcogenide conductive glasses. *Mater. Chem. Phys.* **23**, 121-142 (1989).
26. Adachi, G.-y., Imanaka, N. & Aono, H. Fast Li^+ Conducting Ceramic Electrolytes. *Adv. Mater.* **8**, 127-135 (1996).

27. Goodenough, J.B. Cathode materials: A personal perspective. *J. Power Sources* **174**, 996-1000 (2007).
28. Whittingham, M.S. Lithium Batteries and Cathode Materials. *Chem. Rev.* **104**, 4271-4302 (2004).
29. Schougaard, S.B., Bréger, J., Jiang, M., Grey, C.P. & Goodenough, J.B. $\text{LiNi}_{0.5+\delta}\text{Mn}_{0.5-\delta}\text{O}_2$ - A High-Rate, High-Capacity Cathode for Lithium Rechargeable Batteries. *Adv. Mater.* **18**, 905-909 (2006).
30. Kang, K., Meng, Y.S., Bréger, J., Grey, C.P. & Ceder, G. Electrodes with High Power and High Capacity for Rechargeable Lithium Batteries. *Science* **311**, 977-980 (2006).
31. Spahr, M.E., Novák, P., Schnyder, B., Haas, O. & Nesper, R. Characterization of Layered Lithium Nickel Manganese Oxides Synthesized by a Novel Oxidative Coprecipitation Method and Their Electrochemical Performance as Lithium Insertion Electrode Materials. *J. Electrochem. Soc.* **145**, 1113-1121 (1998).
32. Yamamoto, O. et al. Proceedings of the Eighth International Meeting on Lithium Batteries Cycling performance of novel lithium insertion electrode materials based on the Li-Ni-Mn-O system. *J. Power Sources* **68**, 629-633 (1997).
33. Thackeray, M.M., David, W.I.F., Bruce, P.G. & Goodenough, J.B. Lithium insertion into manganese spinels. *Mater. Res. Bull.* **18**, 461-472 (1983).
34. Thackeray, M.M., Johnson, P.J., de Picciotto, L.A., Bruce, P.G. & Goodenough, J.B. Electrochemical extraction of lithium from LiMn_2O_4 . *Mater. Res. Bull.* **19**, 179-187 (1984).
35. Hirayama, M. et al. Characterization of Electrode/Electrolyte Interface with X-Ray Reflectometry and Epitaxial-Film LiMn_2O_4 Electrode. *J. Electrochem. Soc.* **154**, A1065-A1072 (2007).
36. Hunter, J.C. Preparation of a new crystal form of manganese dioxide: λ - MnO_2 . *J. Solid State Chem.* **39**, 142-147 (1981).
37. Park, O.K. et al. Who will drive electric vehicles, olivine or spinel? *Energ. Environ. Sci.* **4**, 1621-1633 (2011).
38. Padhi, A.K., Nanjundaswamy, K.S. & Goodenough, J.B. Phospho-olivines as Positive-Electrode Materials for Rechargeable Lithium Batteries. *J. Electrochem. Soc.* **144**, 1188-1194 (1997).
39. Ellis, B.L., Lee, K.T. & Nazar, L.F. Positive Electrode Materials for Li-Ion and Li-Batteries. *Chem. Mater.* **22**, 691-714 (2010).
40. Chen, Z.H. & Dahn, J.R. Reducing carbon in LiFePO_4/C composite electrodes to maximize specific energy, volumetric energy, and tap density. *J. Electrochem. Soc.* **149**, A1184-A1189 (2002).
41. Dominko, R. et al. Impact of the carbon coating thickness on the electrochemical performance of LiFePO_4/C composites. *J. Electrochem. Soc.* **152**, A607-A610 (2005).
42. Zhou, F., Cococcioni, M., Kang, K. & Ceder, G. The Li intercalation potential of LiMPO_4 and LiMSiO_4 olivines with M = Fe, Mn, Co, Ni. *Electrochem. Commun.* **6**, 1144-1148 (2004).
43. Zhou, F., Kang, K., Maxisch, T., Ceder, G. & Morgan, D. The electronic structure and band gap of LiFePO_4 and LiMnPO_4 . *Solid State Commun.* **132**, 181-186 (2004).
44. Gong, Z. & Yang, Y. Recent advances in the research of polyanion-type cathode materials for Li-ion batteries. *Energ. Environ. Sci.* **4**, 3223-3242 (2011).
45. Sawai, K., Iwakoshi, Y. & Ohzuku, T. Carbon materials for lithium-ion (shuttlecock) cells. *Solid State Ion.* **69**, 273-283 (1994).
46. Liu, Y., Xue, J.S., Zheng, T. & Dahn, J.R. Mechanism of lithium insertion in hard carbons prepared by pyrolysis of epoxy resins. *Carbon* **34**, 193-200 (1996).
47. Magasinski, A. et al. High-performance lithium-ion anodes using a hierarchical bottom-up approach. *Nat. Mater.* **9**, 353-358 (2010).
48. Aravindan, V., Lee, Y.-S. & Madhavi, S. Research Progress on Negative Electrodes for Practical Li-Ion Batteries: Beyond Carbonaceous Anodes. *Adv. Energy Mater.* **5**, in press (2015).
49. Cabana, J., Monconduit, L., Larcher, D. & Palacín, M.R. Beyond Intercalation-Based Li-Ion Batteries: The State of the Art and Challenges of Electrode Materials Reacting Through Conversion Reactions. *Adv. Mater.* **22**, E170-E192 (2010).
50. Zhang, W.-J. A review of the electrochemical performance of alloy anodes for lithium-ion batteries. *J. Power Sources* **196**, 13-24 (2011).
51. Jiang, J. et al. Recent advances in metal oxide-based electrode architecture design for electrochemical energy storage. *Adv. Mater.* **24**, 5166-5180 (2012).

52. Tarascon, J.-M. Is lithium the new gold? *Nat Chem* **2**, 510-510 (2010).
53. Kim, S.-W., Seo, D.-H., Ma, X., Ceder, G. & Kang, K. Electrode Materials for Rechargeable Sodium-Ion Batteries: Potential Alternatives to Current Lithium-Ion Batteries. *Adv. Energy Mater.* **2**, 710-721 (2012).
54. Slater, M.D., Kim, D., Lee, E. & Johnson, C.S. Sodium-Ion Batteries. *Adv. Funct. Mater.* **23**, 947-958 (2013).
55. Hong, S.Y. et al. Charge carriers in rechargeable batteries: Na ions vs. Li ions. *Energ. Environ. Sci.* **6**, 2067-2081 (2013).
56. Wang, Y., He, P. & Zhou, H. Olivine LiFePO₄: development and future. *Energ. Environ. Sci.* **4**, 805-817 (2011).
57. Wang, J.J. & Sun, X.L. Understanding and recent development of carbon coating on LiFePO₄ cathode materials for lithium-ion batteries. *Energ. Environ. Sci.* **5**, 5163-5185 (2012).
58. Chen, Z. & Dahn, J.R. Reducing Carbon in LiFePO₄/C Composite Electrodes to Maximize Specific Energy, Volumetric Energy, and Tap Density. *J. Electrochem. Soc.* **149**, A1184-A1189 (2002).
59. Wang, Y., Wang, Y., Hosono, E., Wang, K. & Zhou, H. The Design of a LiFePO₄/Carbon Nanocomposite With a Core-Shell Structure and Its Synthesis by an In Situ Polymerization Restriction Method. *Angew. Chem. Int. Ed.* **47**, 7461-7465 (2008).
60. Fan, Q., Tang, Y. & Chen, Y. A novel method to fabricate nonstoichiometric LiFePO₄/C core-shell composites. *J. Power Sources* **205**, 463-466 (2012).
61. Huang, Y.-H., Park, K.-S. & Goodenough, J.B. Improving Lithium Batteries by Tethering Carbon-Coated LiFePO₄ to Polypyrrole. *J. Electrochem. Soc.* **153**, A2282-A2286 (2006).
62. Lepage, D., Michot, C., Liang, G., Gauthier, M. & Schougaard, S.B. A Soft Chemistry Approach to Coating of LiFePO₄ with a Conducting Polymer. *Angew. Chem. Int. Ed.* **50**, 6884-6887 (2011).
63. Chung, S.Y., Bloking, J.T. & Chiang, Y.M. Electronically conductive phospho-olivines as lithium storage electrodes. *Nat. Mater.* **1**, 123-128 (2002).
64. Bilecka, I. et al. Microwave-assisted solution synthesis of doped LiFePO₄ with high specific charge and outstanding cycling performance. *J. Mater. Chem.* **21**, 5881-5890 (2011).
65. Sun, C., Rajasekhara, S., Goodenough, J.B. & Zhou, F. Monodisperse Porous LiFePO₄ Microspheres for a High Power Li-Ion Battery Cathode. *J. Am. Chem. Soc.* **133**, 2132-2135 (2011).
66. Doherty, C.M., Caruso, R.A., Smarsly, B.M., Adelhelm, P. & Drummond, C.J. Hierarchically Porous Monolithic LiFePO₄/Carbon Composite Electrode Materials for High Power Lithium Ion Batteries. *Chem. Mater.* **21**, 5300-5306 (2009).
67. Popovic, J. et al. LiFePO₄ Mesocrystals for Lithium-Ion Batteries. *Small* **7**, 1127-1135 (2011).
68. Yim, C.-H., Baranova, E.A., Abu-Lebdeh, Y. & Davidson, I. Highly ordered LiFePO₄ cathode material for Li-ion batteries templated by surfactant-modified polystyrene colloidal crystals. *J. Power Sources* **205**, 414-419 (2012).
69. García-Moreno, O. et al. Influence of the Structure on the Electrochemical Performance of Lithium Transition Metal Phosphates as Cathodic Materials in Rechargeable Lithium Batteries: A New High-Pressure Form of LiMPO₄ (M = Fe and Ni). *Chem. Mater.* **13**, 1570-1576 (2001).
70. Voß, B. et al. Facile Synthesis of the High-Pressure Polymorph of Nanocrystalline LiFePO₄ at Ambient Pressure and Low Temperature. *Chem. Mater.* **24**, 633-635 (2012).
71. Bilecka, I. & Niederberger, M. Microwave chemistry for inorganic nanomaterials synthesis. *Nanoscale* **2**, 1358-1374 (2010).
72. Baghbanzadeh, M., Carbone, L., Cozzoli, P.D. & Kappe, C.O. Microwave-Assisted Synthesis of Colloidal Inorganic Nanocrystals. *Angew. Chem. Int. Ed.* **50**, 11312-11359 (2011).
73. Bilecka, I., Hintennach, A., Djerdj, I., Novak, P. & Niederberger, M. Efficient microwave-assisted synthesis of LiFePO₄ mesocrystals with high cycling stability. *J. Mater. Chem.* **19**, 5125-5128 (2009).
74. Carriazo, D. et al. Formation Mechanism of LiFePO₄ Sticks Grown by a Microwave-Assisted Liquid-Phase Process. *Small* **8**, 2231-2238 (2012).
75. Shi, S. et al. First-principles study of lattice dynamics of LiFePO₄. *Phys. Lett. A* **373**, 4096-4100 (2009).
76. Yang, J. & Tse, J.S. Li Ion Diffusion Mechanisms in LiFePO₄: An ab Initio Molecular Dynamics Study. *J. Phys. Chem. A* **115** (2011).

77. Inorganic 3D Structures, Springer (2011).
78. Islam, M.S., Driscoll, D.J., Fisher, C.A.J. & Slater, P.R. Atomic-scale investigation of defects, dopants, and lithium transport in the LiFePO₄ olivine-type battery material. *Chem. Mater.* **17**, 5085-5092 (2005).
79. Chung, S.-Y., Choi, S.-Y., Yamamoto, T. & Ikuhara, Y. Atomic-Scale Visualization of Antisite Defects in LiFePO₄. *Phys. Rev. Lett.* **100**, 125502 (2008).
80. Fisher, C.A.J., Hart Prieto, V.M. & Islam, M.S. Lithium Battery Materials LiMPO₄ (M = Mn, Fe, Co, and Ni): Insights into Defect Association, Transport Mechanisms, and Doping Behavior. *Chem. Mater.* **20**, 5907-5915 (2008).
81. Gardiner, G.R. & Islam, M.S. Anti-Site Defects and Ion Migration in the LiFe_{0.5}Mn_{0.5}PO₄ Mixed-Metal Cathode Material. *Chem. Mater.* **22**, 1242-1248 (2009).
82. Dodd, J.L., Yazami, R. & Fultz, B. Phase Diagram of Li_xFePO₄. *Electrochem. Solid-State Lett.* **9**, A151-A155 (2006).
83. Tang, P., Holzwarth, N.A.W. & Holzwarth Comparison of the electronic structures of four crystalline phases of FePO₄. *Phys. Rev. B* **76** (2007).
84. Rouse, G., Rodriguez-Carvajal, J., Patoux, S. & Masquelier, C. Magnetic structures of the triphylite LiFePO₄ and of its delithiated form FePO₄. *Chem. Mater.* **15**, 4082-4090 (2003).
85. Palomares, V. et al. Structural, magnetic and electrochemical study of a new active phase obtained by oxidation of a LiFePO₄/C composite. *J. Mater. Chem.* **22**, 4735-4743 (2012).
86. Arroyo-de Dompablo, M.E., Gallardo-Amores, J.M. & Amador, U. Lithium Insertion in the High-Pressure Polymorph of FePO₄: Computational Predictions and Experimental Findings. *Electrochem. Solid-State Lett.* **8**, A564-A569 (2005).
87. de Dompablo, M. et al. Gaining Insights into the Energetics of FePO₄ Polymorphs. *Chem. Mater.* **22**, 994-1001 (2010).
88. Prohini, P.P. Iron Phosphate Materials as Cathodes for Lithium Batteries. Springer (2011).
89. Gómez-Avilés, A., Darder, M., Aranda, P. & Ruiz-Hitzky, E. Functionalized Carbon-Silicates from Caramel-Sepiolite Nanocomposites. *Angew. Chem. Int. Ed.* **46**, 923-925 (2007).
90. Dathar, G.K.P., Sheppard, D., Stevenson, K.J. & Henkelman, G. Calculations of Li-Ion Diffusion in Olivine Phosphates. *Chem. Mater.* **23**, 4032-4037 (2011).
91. Hu, G.R., Xiao, Z.W., Peng, Z.D., Du, K. & Deng, X.R. Preparation of LiFePO₄ for lithium ion battery using Fe₂P₂O₇ as precursor. *J. Cent. South Univ. T* **15**, 531-534 (2008).
92. Lee, G.H., Seo, S.D., Shim, H.W., Park, K.S. & Kim, D.W. Synthesis and Li electroactivity of Fe₂P₂O₇ microspheres composed of self-assembled nanorods. *Ceram. Int.* **38**, 6927-6930 (2012).
93. Lee, M.-H., Kim, J.-Y. & Song, H.-K. A hollow sphere secondary structure of LiFePO₄ nanoparticles. *Chem. Commun.* **46**, 6795-6797 (2010).
94. Oh, S.W. et al. Double Carbon Coating of LiFePO₄ as High Rate Electrode for Rechargeable Lithium Batteries. *Adv. Mater.* **22**, 4842-4845 (2010).
95. Yu, F., Zhang, J.-J., Yang, Y.-F. & Song, G.-Z. Up-scalable synthesis, structure and charge storage properties of porous microspheres of LiFePO₄@C nanocomposites. *J. Mater. Chem.* **19**, 9121-9125 (2009).
96. Morgan, D., Van der Ven, A. & Ceder, G. Li Conductivity in Li_xMPO₄ (M = Mn, Fe, Co, Ni) Olivine Materials. *Electrochem. Solid-State Lett.* **7**, A30-A32 (2004).
97. Nishimura, S.-i. et al. Experimental visualization of lithium diffusion in Li_xFePO₄. *Nat. Mater.* **7**, 707-711 (2008).
98. Gaberscek, M., Moskon, J., Erjavec, B., Dominko, R. & Jamnik, J. The importance of interphase contacts in Li ion electrodes: the meaning of the high-frequency impedance arc. *Electrochem. Solid-State Lett.* **11**, A170-A174 (2008).
99. Atebamba, J.-M., Moskon, J., Pejovnik, S. & Gaberscek, M. On the Interpretation of Measured Impedance Spectra of Insertion Cathodes for Lithium-Ion Batteries. *J. Electrochem. Soc.* **157**, A1218-A1228 (2010).
100. Clark, S.J. et al. First principles methods using CASTEP. *Z. Kristall.* **220**, 567-570 (2005).
101. Grimme, S. Semiempirical GGA-type density functional constructed with a long-range dispersion correction. *J. Comput. Chem.* **27**, 1787-1799 (2006).

102. Goodenough, J.B. Evolution of strategies for modern rechargeable batteries. *Acc. Chem. Res.* **46**, 1053-1061 (2013).
103. Li, N., Chen, Z., Ren, W., Li, F. & Cheng, H.-M. Flexible graphene-based lithium ion batteries with ultrafast charge and discharge rates. *Proc. Natl. Acad. Sci.* **109**, 17360-17365 (2012).
104. Zhou, F., Xin, S., Liang, H.-W., Song, L.-T. & Yu, S.-H. Carbon Nanofibers Decorated with Molybdenum Disulfide Nanosheets: Synergistic Lithium Storage and Enhanced Electrochemical Performance. *Angew. Chem. Int. Ed.* **53**, 11552-11556 (2014).
105. Chang, K. & Chen, W. L-Cysteine-Assisted Synthesis of Layered MoS₂/Graphene Composites with Excellent Electrochemical Performances for Lithium Ion Batteries. *ACS Nano* **5**, 4720-4728 (2011).
106. Kim, Y. et al. Additive-Free Hollow-Structured Co₃O₄ Nanoparticle Li-Ion Battery: The Origins of Irreversible Capacity Loss. *ACS Nano* **8**, 6701-6712 (2014).
107. Wu, Z.-S. et al. Graphene Anchored with Co₃O₄ Nanoparticles as Anode of Lithium Ion Batteries with Enhanced Reversible Capacity and Cyclic Performance. *ACS Nano* **4**, 3187-3194 (2010).
108. Wu, F., Ma, X., Feng, J., Qian, Y. & Xiong, S. 3D Co₃O₄ and CoO@C Wall Arrays: Morphology Control, Formation Mechanism, and Lithium-Storage Properties. *J. Mater. Chem. A* **2**, 11597-11605 (2014).
109. Li, B. et al. Co₃O₄@graphene Composites as Anode Materials for High-Performance Lithium Ion Batteries. *Inorg. Chem.* **50**, 1628-1632 (2011).
110. Wang, Y., Xia, H., Lu, L. & Lin, J. Excellent Performance in Lithium-Ion Battery Anodes: Rational Synthesis of Co(CO₃)_{0.5}(OH)_{0.1}H₂O Nanobelt Array and Its Conversion into Mesoporous and Single-Crystal Co₃O₄. *ACS Nano* **4**, 1425-1432 (2010).
111. Huang, G., Xu, S., Lu, S., Li, L. & Sun, H. Micro-/Nanostructured Co₃O₄ Anode with Enhanced Rate Capability for Lithium-Ion Batteries. *ACS Appl. Mater. Interfaces* **6**, 7236-7243 (2014).
112. Liu, N. et al. A Pomegranate-Inspired Nanoscale Design for Large-Volume-Change Lithium Battery Anodes. *Nat. Nanotechnol.* **9**, 187-192 (2014).
113. Kwon, Y.H. et al. Cable-Type Flexible Lithium Ion Battery Based on Hollow Multi-Helix Electrodes. *Adv. Mater.* **24**, 5192-5197 (2012).
114. Zhai, Y. et al. Carbon Materials for Chemical Capacitive Energy Storage. *Adv. Mater.* **23**, 4828-4850 (2011).
115. Xin, S., Guo, Y.-G. & Wan, L.-J. Nanocarbon Networks for Advanced Rechargeable Lithium Batteries. *Acc. Chem. Res.* **45**, 1759-1769 (2012).
116. Roberts, A.D., Li, X. & Zhang, H. Porous Carbon Spheres and Monoliths: Morphology Control, Pore Size Tuning and Their Applications As Li-Ion Battery Anode materials. *Chem. Soc. Rev.* **43**, 4341-4356 (2014).
117. Antonietti, M., Fechner, N. & Feller, T.-P. Carbon Aerogels and Monoliths: Control of Porosity and Nanoarchitecture via Sol-Gel routes. *Chem. Mater.* **26**, 196-210 (2013).
118. Heiligtag, F.J., Rossell, M.D., Suess, M.J. & Niederberger, M. Template-Free Co-Assembly of Preformed Au and TiO₂ Nanoparticles into Multicomponent 3D Aerogels. *J. Mater. Chem.* **21**, 16893-16899 (2011).
119. Rechberger, F., Heiligtag, F.J., Süess, M.J. & Niederberger, M. Assembly of BaTiO₃ Nanocrystals into Macroscopic Aerogel Monoliths with High Surface Area. *Angew. Chem. Int. Ed.* **53**, 6823-6826 (2014).
120. Heiligtag, F.J., Airaghi Leccardi, M.J.I., Erdem, D., Suess, M.J. & Niederberger, M. Anisotropically Structured Magnetic Aerogel Monoliths. *Nanoscale* **6**, 13213-13221 (2014).
121. Wang, L., Zhuo, L., Zhang, C. & Zhao, F. Embedding NiCo₂O₄ Nanoparticles into a 3DHPC Assisted by CO₂-Expanded Ethanol: A Potential Lithium-Ion Battery Anode with High Performance. *ACS Appl. Mater. Interfaces* **6**, 10813-10820 (2014).
122. Yin, L. et al. Spinel ZnMn₂O₄ Nanocrystal-Anchored 3D Hierarchical Carbon Aerogel Hybrids as Anode Materials for Lithium Ion Batteries. *Adv. Funct. Mater.* **24**, 4176-4185 (2014).
123. Yang, S., Feng, X., Ivanovici, S. & Müllen, K. Fabrication of Graphene-Encapsulated Oxide Nanoparticles: Towards High-Performance Anode Materials for Lithium Storage. *Angew. Chem. Int. Ed.* **49**, 8408-8411 (2010).
124. Zhu, J. et al. Facile Synthesis of Metal Oxide/Reduced Graphene Oxide Hybrids with High Lithium Storage Capacity and Stable Cyclability. *Nanoscale* **3**, 1084-1089 (2011).

125. Bilecka, I., Kubli, M., Amstad, E. & Niederberger, M. Simultaneous Formation of Ferrite Nanocrystals and Deposition of Thin Films via a Microwave-assisted Nonaqueous Sol-Gel Process. *J. Sol-Gel Sci. Technol.* **57**, 313-322 (2011).
126. Adhikari, B., Biswas, A. & Banerjee, A. Graphene Oxide-Based Hydrogels to Make Metal Nanoparticle-Containing Reduced Graphene Oxide-Based Functional Hybrid Hydrogels. *ACS Appl. Mater. Interfaces* **4**, 5472-5482 (2012).
127. Hu, H., Zhao, Z., Wan, W., Gogotsi, Y. & Qiu, J. Ultralight and Highly Compressible Graphene Aerogels. *Adv. Mater.* **25**, 2219-2223 (2013).
128. Cong, H.-P., Chen, J.-F. & Yu, S.-H. Graphene-Based Macroscopic Assemblies and Architectures: An Emerging Material System. *Chem. Soc. Rev.* **43**, 7295-7325 (2014).
129. Sun, Y., Wu, Q. & Shi, G. Graphene based new energy materials. *Energ. Environ. Sci.* **4**, 1113-1132 (2011).
130. Wu, Z.-S. et al. Three-Dimensional Graphene-Based Macro- and Mesoporous Frameworks for High-Performance Electrochemical Capacitive Energy Storage. *J. Am. Chem. Soc.* **134**, 19532-19535 (2012).
131. Pralong, V. et al. Electrochemical Study of Nanometer Co_3O_4 , Co, CoSb_3 and Sb Thin Films Toward Lithium. *Solid State Ion.* **166**, 295-305 (2004).
132. Kang, Y.M. et al. A Study on the Charge-Discharge Mechanism of Co_3O_4 As An Anode for the Li Ion Secondary Battery. *Electrochim. Acta* **50**, 3667-3673 (2005).
133. Pan, D. et al. Li storage properties of disordered graphene nanosheets. *Chem. Mater.* **21**, 3136-3142 (2009).
134. Memarzadeh Lotfabad, E., Kalisvaart, P., Kohandehghan, A., Karpuzov, D. & Mitlin, D. Origin of Non-SEI Related Coulombic Efficiency Loss in Carbons Tested against Na and Li. *J. Mater. Chem. A* **2**, 19685-19695 (2014).
135. Su, Q., Zhang, J., Wu, Y. & Du, G. Revealing the electrochemical conversion mechanism of porous Co_3O_4 nanoplates in lithium ion battery by in situ transmission electron microscopy. *Nano Energy* **9**, 264-272 (2014).
136. Yoo, E. et al. Large Reversible Li Storage of Graphene Nanosheet Families for Use in Rechargeable Lithium Ion Batteries. *Nano Lett.* **8**, 2277-2282 (2008).
137. Yoshino, A., Sanechika, K. & Nakajima, T., Japanese Patent, No. 1989293 (1985).
138. Wang, G., Shen, X., Yao, J. & Park, J. Graphene nanosheets for enhanced lithium storage in lithium ion batteries. *Carbon* **47**, 2049-2053 (2009).
139. Sato, K., Noguchi, M., Demachi, A., Oki, N. & Endo, M. A mechanism of lithium storage in disordered carbons. *Science* **264**, 556-558 (1994).
140. Han, X., Qing, G., Sun, J. & Sun, T. How many lithium ions can be inserted onto fused C6 aromatic ring systems? *Angew. Chem. Int. Ed.* **51**, 5147-5151 (2012).
141. Wu, Z.-S., Ren, W., Xu, L., Li, F. & Cheng, H.-M. Doped graphene sheets as anode materials with superhigh rate and large capacity for lithium ion batteries. *ACS Nano* **5**, 5463-5471 (2011).
142. Wang, H. et al. Nitrogen-doped graphene nanosheets with excellent lithium storage properties. *J. Mater. Chem.* **21**, 5430-5434 (2011).
143. Zeng, G. et al. A General Method of Fabricating Flexible Spinel-Type Oxide/Reduced Graphene Oxide Nanocomposite Aerogels as Advanced Anodes for Lithium-Ion Batteries. *ACS Nano* **9**, 4227-4235 (2015).
144. Liu, J., Wickramaratne, N.P., Qiao, S.Z. & Jaroniec, M. Molecular-based design and emerging applications of nanoporous carbon spheres. *Nat. Mater.* **14**, 763-774 (2015).
145. Zhao, Y. et al. Self-adaptive strain-relaxation optimization for high-energy lithium storage material through crumpling of graphene. *Nat. Commun.* **5** (2014).
146. Lin, M.-C. et al. An ultrafast rechargeable aluminium-ion battery. *Nature* **520**, 324-328 (2015).
147. Xu, L.Q., Yang, W.J., Neoh, K.-G., Kang, E.-T. & Fu, G.D. Dopamine-induced reduction and functionalization of graphene oxide nanosheets. *Macromolecules* **43**, 8336-8339 (2010).
148. Lei, C. et al. Dopamine as the coating agent and carbon precursor for the fabrication of N-doped carbon coated Fe_3O_4 composites as superior lithium ion anodes. *Nanoscale* **5**, 1168-1175 (2013).
149. Ma, C., Shao, X. & Cao, D. Nitrogen-doped graphene nanosheets as anode materials for lithium ion batteries: a first-principles study. *J. Mater. Chem.* **22**, 8911-8915 (2012).

150. Suzuki, T., Hasegawa, T., Mukai, S.R. & Tamon, H. A theoretical study on storage states of Li ions in carbon anodes of Li ion batteries using molecular orbital calculations. *Carbon* **41**, 1933-1939 (2003).
151. Wang, Z.-L., Xu, D., Wang, H.-G., Wu, Z. & Zhang, X.-B. In Situ Fabrication of Porous Graphene Electrodes for High-Performance Energy Storage. *ACS Nano* **7**, 2422-2430 (2013).
152. Ferrari, A.C. & Basko, D.M. Raman spectroscopy as a versatile tool for studying the properties of graphene. *Nat. Nanotechnol.* **8**, 235-246 (2013).
153. Cançado, L.G. et al. Quantifying defects in graphene via raman spectroscopy at different excitation energies. *Nano Lett.* **11**, 3190-3196 (2011).
154. Zeng, G., Caputo, R., Carriazo, D., Luo, L. & Niederberger, M. Tailoring Two Polymorphs of LiFePO₄ by Efficient Microwave-Assisted Synthesis: A Combined Experimental and Theoretical Study. *Chem. Mater.* **25**, 3399-3407 (2013).
155. Recham, N. et al. A 3.6 V lithium-based fluorosulphate insertion positive electrode for lithium-ion batteries. *Nat. Mater.* **9**, 68-74 (2010).
156. Tripathi, R., Ramesh, T.N., Ellis, B.L. & Nazar, L.F. Scalable Synthesis of Tavorite LiFeSO₄F and NaFeSO₄F Cathode Materials. *Angew. Chem. Int. Ed.* **49**, 8738-8742 (2010).
157. Yuan, Z. et al. A novel benzene-water azeotrope route to new Na-based metal fluorosulphates NaFeSO₄F and NaFeSO₄F·2H₂O in one minute. *CrystEngComm* **14**, 4251-4254 (2012).
158. Sobkowiak, A. et al. Understanding and Controlling the Surface Chemistry of LiFeSO₄F for an Enhanced Cathode Functionality. *Chem. Mater.* **25**, 3020-3029 (2013).
159. Chou, C.-Y., Lee, M. & Hwang, G.S. A Comparative First-Principles Study on Sodiation of Silicon, Germanium, and Tin for Sodium-Ion Batteries. *J. Phys. Chem. C* **119**, 14843-14850 (2015).

Curriculum Vitae

ETH Zurich
Laboratory for Multifunctional Materials
HCI F511, Vladimir-Prelog-Weg 5
8093 Zurich
+41 44 633 94 72
guobo.zeng@mat.ethz.ch

ZENG Guobo

EDUCATION

PhD study in Materials Science, ETH Zurich, Switzerland

2011/08 – 05/2016

with Prof. Markus Niederberger: Multifunctional materials for lithium-ion batteries

Master Degree in Materials Science, ETH Zurich, Switzerland

09/2008 – 05/2011

with Prof. Reinhard Nesper: Molybdenum compounds and their applications for lithium-ion batteries

Bachelor Degree in Materials Science & Engineering, Central South University, P. R. China

09/2004 – 06/2008

with Prof. Zhiming Yu: The effects of W/W-C interlayer on adhesion of HFCVD diamond film

MAIN AWARD

E-MRS Graduate Student Award, Lille, France, 05/2016

Swiss Chemical Society Travel Award, 05/2015

Chinese Government Award for Outstanding Student Abroad (国家优秀自费留学生), 03/2015

“Chunhui” Pioneer Cup Award (春晖杯), 12/2014

PUBLICATIONS

R. Deshmukh, **G. Zeng**, E. Tervoort, M. Staniuk, D. Wood, M. Niederberger, **Ultrasmall Cu₃N Nanoparticles: Surfactant-Free Solution-Phase Synthesis, Nitridation Mechanism, and Application for Lithium Storage.** *Chem. Mater.* **2015**, 27, 8282-8288

Zeng, G.; Shi, N.; Hess, M.; Chen, X.; Cheng, W.; Fan, T.; Niederberger, M. **A General Method of Fabricating Flexible Spinel-Type Oxide/Reduced Graphene Oxide Nanocomposite Aerogels as Advanced Anodes for Lithium-Ion Batteries.** *ACS Nano* **2015**, 4227–4235

Cheng, W.; **Zeng, G.**; Niederberger, M. **Design of Vanadium Oxide Core-Shell Nanoplatelets for Lithium Ion Storage.** *J. Mater. Chem. A* **2015**, 3, 2861-2868

Hirsch, O.[#]; **Zeng, G.**[#]; Luo, L.; Staniuk, M.; Abdala, P. M.; van Beek, W.; Rechberger, F.; Süess, M. J.; Niederberger, M.; Koziej, D. **Aliovalent Ni in MoO₂ Lattice— Probing the Structure and Valence of Ni and Its Implication on the Electrochemical Performance.** *Chem. Mater.* **2014**, 26, 4505-4513 (#Equal Contribution)

Zeng, G.; Caputo, R.; Carriazo, D.; Luo, L.; Niederberger, M. **Tailoring Two Polymorphs of LiFePO₄ by Efficient Microwave-Assisted Synthesis: A Combined Experimental and Theoretical Study.** *Chem. Mater.* **2013**, 25, 3399-3407

Carriazo, D.; Rossell, M. D.; Zeng, G.; Bilecka, I.; Erni, R.; Niederberger, M. **Formation Mechanism**

of LiFePO₄ Sticks Grown by a Microwave-Assisted Liquid-Phase Process. *Small* **2012**, 8, 2231

CONFERENCES

European Materials Research Society (E-MRS) Spring Meeting 2016, Lille, France 05/2016

Oral: Hierarchical graphene-composite aerogels for ultra long-life Li-ion batteries

8th International Conference on Materials for Advanced Technologies (ICMAT) of the Materials Research Society of Singapore, Singapore, 06/2015

Oral: A General Method of Fabricating Reduced Graphene Oxide Nanocomposite Aerogels with Conversion-Type Electrode Materials for Advanced Lithium-Ion Batteries

Materials Research Society (MRS) Spring Meeting, San Francisco, USA 04/2015

Oral: A General Method of Fabricating Flexible Spinel-Type Oxide/Reduced Graphene Oxide Nanocomposite Aerogels for Advanced Lithium-Ion Batteries

Swiss Chemical Society (SCS) Fall Meeting, Zurich 09/2014

Poster: Flexible Co₃O₄-rGO Composite Aerogel as High-Performance Anode in Li-Ion Batteries

8th MRC Graduate Symposium, 05/2013

Poster: Efficient Microwave-Assisted Synthesis of LiFePO₄ with Various Primary and Secondary Structures for High power Li-ion Batteries, Poster Award

SCS Fall Meeting, Lausanne 09/2013

Poster: Tailoring Two Polymorphs of LiFePO₄ by Efficient Microwave-Assisted Synthesis for High-power Li-ion Batteries

ONGOING PROJECTS

Zeng, G.; Niederberger, M. etc. Hierarchical graphene-based aerogels for long-life Li-ion batteries at high rates, *Adv. Mater.*, in press, 2016

Jin, L. Zeng, G.; Wu, H.; Niederberger, M. and Morbidelli M. A Generic Methodology for Generation of Hierarchical Architecture in Active Electrode Materials for Lithium Ion Batteries, submitted, 2016

Zeng, G. & Niederberger, M. etc. High-Performance Sodium-Ion Batteries, manuscript under preparation, 2016

Zeng, G. & Niederberger, M. etc. Rational Design of LiFePO₄ Polymorphs via Microwave-Assisted Synthesis, manuscript under preparation, 2016

EXPERIMENTAL SKILLS

From battery electrode materials synthesis to battery assembly and test (ex-situ and in-situ)

Characterizations: XRD, SEM, XPS and HRTEM

REFERENCE

Prof. Dr. Markus Niederberger

Department of Materials, ETH Zurich

phone +41 44 633 63 90

markus.niederberger@mat.ethz.ch